

Department of Physics and Astronomy

Heidelberg University

Master thesis

in Physics

submitted by

Álvaro Lozano Onrubia

born in Madrid (Spain)

2021

Strong First-Order Electroweak Phase

Transitions:

A Reassessment of the Sphaleron Decoupling Criterion

In two Models with
Extended Scalar Sectors

This Master thesis has been carried out by

Álvaro Lozano Onrubia

at the

Max Planck Institute for Nuclear Physics

under the supervision of

Dr. Florian Goertz

Acknowledgements

First and foremost, I wish to thank Dr. Florian Goertz for the opportunity and for his excellent mentoring throughout the past year. The success of this thesis rests in no small part on his academic advice as well as his moral support and encouragement. Furthermore, I wish to commend him for his group, NEWFO, a team of talented scientists which helped me better understand the finer details of modern physics through many fruitful discussions. I thank Sven Fabian, Dr. Andrei Anghel and Dr. Yun Jiang for the valuable insights into the physics of phase transitions. I further express my gratitude towards the rest of the group as well as the division of Prof. Dr. Dr. h.c. Manfred Lindner for the warm welcome. In a broader sense, I also wish to extend my gratitude to the Max Planck Institute for Nuclear Physics and, in particular, to its IT service. Without the technical support in issues related to the computing cluster, many calculations featured in my results could not have been carried out.

In addition to the staff at MPIK, I thank Laura Batini, Moritz Breitbach, Dr. Kaori Fuyuto, Dr. Huaike Guo and Prof. Amine Ahriche for inspiring discussions and clarifications as well as useful literature recommendations.

I thank María Isabel Dias Astros, Sven Fabian and Dr. Andrei Anghel for the proofreading and their valuable comments.

Thanks to the entirety of my Heidelberg family for the splendid time throughout the past years. As the song goes – *ich hab' mein Herz in Heidelberg verloren!* Of course, thanks to all of my friends abroad.

Finalmente, quiero agradecer a mis padres, a mis hermanos y a toda mi familia su apoyo durante estos años.

Strong First-Order Electroweak Phase Transitions:**A Reassessment of the Sphaleron Decoupling Criterion In two Models with Extended Scalar Sectors**

Electroweak baryogenesis builds on the premise of a strong first-order electroweak phase transition, which is realized when the temperature T at its onset and the corresponding temperature-dependent Higgs vacuum expectation value $v(T)$ satisfy $v(T)/T \gtrsim 1.0$ according to a standard working criterion. This thesis reassesses the reliability of the criterion in two models with extended scalar sectors: the Inert Doublet Model and a real scalar singlet extension of the Standard Model. The focus lies in a reevaluation of the dominant temperature- and model-dependent effects of the electroweak sphaleron, which underlie the criterion and determine the order of magnitude of the condition. Furthermore, the widely neglected subtlety of successful bubble nucleation is addressed. Its implications are comprehensively studied in the Inert Doublet Model and generally accounted for in both models – for which recent phenomenological constraints are taken into consideration – by evaluating the phase transition strength at the nucleation temperature. Ultimately, the effects of the new physics and the chosen temperature scheme on the criterion are found to be modest, with the respective analyses of the models both suggesting an updated criterion $v(T)/T \gtrsim (1.05 - 1.30)$ that agrees well with the most generous state-of-the-art estimates.

Starke Elektroschwache Phasenübergänge Erster Ordnung:**Eine Neubewertung des Sphaleron-Entkopplungskriteriums in zwei Modellen mit erweiterten Skalarsektoren**

Elektroschwache Baryogenese baut auf der Prämisse eines starken elektroschwachen Phasenübergangs erster Ordnung auf, der gemäß eines Standardkriteriums dann realisiert wird, wenn die Übergangstemperatur T und der entsprechende temperaturabhängige Higgs-Vakuumerwartungswert $v(T)$ die Bedingung $v(T)/T \gtrsim 1.0$ erfüllen. In dieser Arbeit wird die Zuverlässigkeit des Kriteriums in zwei Modellen mit erweiterten Skalarsektoren neu bewertet: dem Inert-Doublet-Modell und einer realen skalaren Singulett-Erweiterung des Standardmodells. Der Schwerpunkt liegt in einer Neubeurteilung der dominanten temperatur- und modellabhängigen Effekte des elektroschwachen Sphalerons, welche dem Kriterium letztendlich zugrunde liegen und die Größenordnung der Bedingung festlegen. Außerdem wird die weithin vernachlässigte Feinheit der erfolgreichen Blasen nucleation angerissen. Ihre Auswirkungen werden im Inert-Doublet-Modell umfassend untersucht und in beiden Modellen – hinsichtlich neuester phänomenologischer Einschränkungen aufgestellt – allgemein berücksichtigt, indem die Phasenübergangsstärke bei der Nukleationstemperatur ausgewertet wird. Letztendlich gelten die Auswirkungen der neuen Physik und des gewählten Temperaturschemas auf das Kriterium als bescheiden: die jeweiligen Analysen der Modelle schlagen ein angepasstes Kriterium $v(T)/T \gtrsim (1.05 - 1.30)$ vor, welches gut mit den großzügigsten aktuellen Abschätzungen übereinstimmt.

Contents

I	Introduction and theoretical background	1
1	Introduction	3
2	Electroweak theory in the SM	6
3	Quantum field theory essentials	10
4	Baryon number violation and Yang-Mills vacua	15
4.1	Violation of baryon number conservation in the SM	15
4.2	$SU(2)$ and its vacuum structure	18
5	The electroweak sphaleron	23
5.1	Sphaleron field configuration	25
5.2	The sphaleron rate	29
6	Thermal phase transitions	31
6.1	First-order phase transitions	31
6.2	Barrier penetration and quantum tunneling	33
6.2.1	The bounce	35
6.3	Nucleation in finite-temperature field theory	36
6.4	Electroweak nucleation in a thermal universe	37
6.5	The EWPhT in BSM physics	38
7	Electroweak baryogenesis	39
7.1	Outline of the mechanism	39
7.2	Sphaleron decoupling condition	43
7.3	Status of electroweak baryogenesis	46
II	Methods	47
8	Constructing the effective potential	49
8.1	Coleman-Weinberg potential	49
8.2	Thermal one-loop corrections	50
8.3	Thermal resummation	51
8.4	Thermal Debye masses	52
8.5	Full thermal effective potential	53
9	Numerical methods	54
9.1	CosmoTransitions	54
9.2	Relaxation algorithm	55

III Criterion for a strong first-order electroweak phase transition in BSM scenarios	59
10 Inert Doublet Model	61
10.1 The model	61
10.2 Construction of the effective potential	62
10.2.1 Parametrization	63
10.2.2 Zero-temperature, field-dependent masses	63
10.2.3 Counterterm potential	64
10.2.4 Thermal mass corrections	65
10.3 Constraints on the model parameters	66
10.3.1 Theoretical constraints	67
10.3.2 Experimental constraints	68
10.4 Construction of the electroweak sphaleron	69
10.5 Investigation of the decoupling criteria	71
10.5.1 Selection of benchmark points	71
10.5.2 Characterization of the sphaleron	72
10.5.3 SFOPhTs and sphaleron decoupling in the IDM	74
11 Real scalar singlet extension	82
11.1 The model	82
11.2 Construction of the effective potential	83
11.2.1 Zero-temperature, field-dependent masses	83
11.2.2 Counterterm potential	84
11.2.3 Thermal mass corrections	85
11.3 Constraints on the model parameters	86
11.3.1 Theoretical constraints	86
11.3.2 Experimental constraints	88
11.4 Construction of the electroweak sphaleron	90
11.5 Investigation of the decoupling criteria	91
11.5.1 Selection of benchmark points	91
11.5.2 Characterization of the sphaleron	93
11.5.3 SFOPhTs and sphaleron decoupling in the rSM	95
12 Conclusion and outlook	99
A Units and conventions	121
B Finite-temperature Feynman rules	124
C Saddle-point method	125
D Mathematical background	127
D.1 Maps and homotopy theory	127
D.2 Saddle points of functions on manifolds	128
E The Standard Model sphaleron	130
E.1 Existence	130
E.2 $U(1)$ corrections to the SM sphaleron energy	132

F Sphaleron rate	134
G Relaxation method	136
H Aspects of the IDM	138
H.1 Parameter constraints in the IDM	138
H.1.1 Perturbative unitarity	138
H.1.2 Oblique parameters	138
H.1.3 Plotting range in plots of σ and $\mathcal{E}(T)/T$	139
I Aspects of the rSM	140
I.1 Eigenvalues of the Higgs-singlet mass matrix	140
I.2 Perturbative unitarity constraints	140

Acronyms

1PI	1-Particle-Irreducible
2HDM	Two-Higgs-Doublet Model
ABJ	Adler-Bell-Jackiw
BAU	Baryon Asymmetry of the Universe
BMP	Benchmark Point
BSM	Beyond Standard Model
BVP	Boundary Value Problem
CKM	Cabibbo-Kobayashi-Maskawa
CS	Chern-Simons
CW	Coleman-Weinberg
DM	Dark Matter
EW	Electroweak
EWBG	Electroweak Baryogenesis
EWPhT	Electroweak Phase Transition
EWSB	Electroweak Symmetry Breaking
FOPhT	First-Order Phase Transition
FTFT	Finite-Temperature Field Theory
GWS	Glashow-Weinberg-Salam
IDM	Inert Doublet Model
IR	Infrared
QFT	Quantum Field Theory
QM	Quantum Mechanics
rSM	Real-singlet-extended Standard Model
SFOPhT	Strong First-Order Phase Transition
SM	Standard Model
SOPhT	Second-Order Phase Transition

SSB Spontaneous Symmetry Breaking

UV Ultraviolet

VEV Vacuum Expectation Value

List of Figures

4.1 Particle living on a circle.	19
4.2 Vacuum structure of $SU(2)$ as a function of N_{CS}	21
5.1 Multidimensional vacuum structure of $SU(2)$ theory.	23
5.2 Manifold with a non-contractible loop.	24
5.3 Field profiles of the SM $SU(2)$ sphaleron.	29
6.1 Evolution of the potential in first- and second-order phase transitions.	32
6.2 Potential $V(\phi)$ with two non-degenerate minima.	34
6.3 Characteristics of the bounce solution.	36
7.1 Onset of the phase transition: bubble nucleation.	40
7.2 Effects of C and CP violation on quark interactions with the bubble wall.	41
7.3 Expansion of the true vacuum bubbles.	42
8.1 Thermal loops and daisy diagrams.	52
9.1 Sphaleron energies in the SM for different values of λ/g_2^2	58
10.1 Exemplary sphaleron solutions in the IDM.	72
10.2 Thermal evolution of the normalized VEVs and sphaleron energies in the IDM.	73
10.3 Evolution of $T_{n,c}$ and $v_1(T_{n,c})$ as a function of the mass splitting Δm	75
10.4 Evolution of $\xi_{n,c}$ as a function of the mass splitting Δm	76
10.5 Evolution of $\sigma_{n,c}$ as a function of the mass splitting Δm	77
10.6 Evaluation of $\sigma_{n,c}$ and $\mathcal{E}(T_{n,c})/T_{n,c}$ for two benchmark scans of Δm	78
10.7 Scaling of $\mathcal{E}(T_n)/T_n$ in the IDM for the previous random sample of 800 points.	79
10.8 Comparison of the criteria on σ_n and ξ_n in the IDM for a large scan of parameter space.	80

11.1 Upper limits on the Higgs-singlet mixing parameter.	89
11.2 Exemplary sphaleron solutions in the rSM.	93
11.3 Thermal evolution of the VEVs and sphaleron energies in the rSM.	94
11.4 Scaling of $\mathcal{E}(T_n)/T_n$ with ξ_n in the rSM.	95
11.5 Comparison of the criteria on σ_n and ξ_n in the rSM for a large scan of parameter space.	96

List of Tables

8.1 Property specifications of the particle content.	50
10.1 Parameter space used in the analysis of the IDM.	67
10.2 Benchmark points in the IDM.	71
11.1 Parameter space used in the analysis of the rSM.	89
11.2 Benchmark points in the rSM.	92

Part I

Introduction and theoretical background

Chapter 1

Introduction

Over the past fifty years, the Standard Model (SM) of particle physics has succeeded in providing a comprehensive framework within which to explore the fundamental interactions that shape our universe. And yet, despite its many successes, the sheer variety of its shortcomings cannot be overstated [1–13]. One subtle and yet decisive flaw concerns baryonic matter, which the SM presumes to describe well. While the theory provides a sound account of baryonic matter largely backed up by experimental evidence, nothing in its structure suggests a prevalence of baryons over antibaryons or vice versa [14–16]. This notion becomes untenable in the light of present evidence, which suggests an excess of matter over antimatter [17–22]. The *baryon asymmetry of the universe* (BAU) thus fundamentally calls into question the prowess of the SM.

The BAU becomes all the more puzzling when confronted to our present understanding of cosmology, which quickly rules out the simplest explanations. Accounts of a universe subdivided into matter- and antimatter-dominated regions are short-lived: they are as entropically far-fetched as they are lacking in experimental evidence [17, 23–26]. Neither can the baryon asymmetry be rationalized as an initial condition, as standard inflation calls for a dilution of such relic asymmetries [27]. Fine-tuning issues are particularly acute in the most optimistic cases and thereby become no-go scenarios in the present scientific paradigm [28, 29]. Having virtually excluded the present BAU as a remnant of the pre-inflation era, its generation by means of dynamic processes – *i.e.* *baryogenesis* – faces the best odds.

While baryogenesis has seen very diverse implementations over the past decades (see *e.g.* Ref. [30] for a compilation), its success necessarily rests on common ground provided by the so-called *Sakharov conditions* [31–35]. A process that prompts baryogenesis needs (i) to violate baryon number, (ii) to occur off thermodynamical

equilibrium and (iii) to account for sufficient violation of the C and CP symmetries. Whereas each of these poses a significant strain, the call for baryon number violation faces a very particular challenge: any model of baryogenesis needs to accommodate the present-day stability of the proton¹, an observation at odds with the violation of baryon number [38–43]. Furthermore, the scale disparity inherent to tests of baryogenesis threatens a final *coup de grâce* to many theories, as their testability requires to correlate a process of cosmic scale to a set of accessible and measurable parameters [44, 45].

A candidate mechanism which thrives in these apparent contradictions is *electroweak baryogenesis* (EWBG) [45–53]. At its heart, EWBG takes advantage of an established instance of symmetry breaking – namely electroweak symmetry breaking (EWSB) – in order to source the baryonic asymmetry. In its conception, the mechanism is thus deeply rooted in SM electroweak (EW) phenomenology. The greatest merit of EWBG lies in how it reconciles baryon number violation in the early universe with the present-day stability of matter. Its cornerstone is the EW *sphaleron*: a non-perturbative anomalous process predicted by the SM which is believed to have been enhanced before EWSB, yet to be largely suppressed in this day and age [54–56].

Despite its virtues, EWBG faces a number of well-known implementational drawbacks. While the SM provides a solid framework for the mechanism, the numbers do not add up. In particular, it has been noted that CP violation in the SM is too scarce to account for the observed baryon asymmetry [30, 57–60]. Furthermore, it has been settled that the off-equilibrium property required for EWBG – a *strong first-order phase transition* (SFOPhT) in the EW sector at EWSB – cannot be satisfied within the standard picture [30, 61–65]. Such deficiencies are complemented by the practical impossibility of sphaleron processes at present or foreseeable colliders [66]. Altogether, the study of EWBG is thus set *ab initio* on a path beyond the present theoretical and experimental state of the art.

A large class of scenarios beyond the Standard Model (BSM) features extensions of the SM Higgs sector. Such extensions, often consisting in additional Higgs

¹The stability of matter suggests baryon number conservation. As Ref. [36] points out, the notion of baryon number conservation can be traced back to E. C. G. Stueckelberg [37].

doublets or new singlet scalars altogether, are known to possess non-trivial phase transition behaviours on account of the broadened field content. When these effects are considered, it is possible to alleviate the constraints on the standard Higgs sector which otherwise hinder the viability of a SFOPhT. As high energy theory persists in its supply of viable candidates for EWBG, phenomenological research continues to tie in with experimental advances. The advent of gravitational wave detection has rendered the study of cosmic-calibre phenomena more accessible than ever before, thus uncovering virgin ground for cosmic archaeology [67–72]. As a defining event in the history of the universe, the EWPhT is expected to have left imprints on the gravitational wave spectrum, its signature very much defined by the type and strength of the phase transition and the underlying field content of the theory. The prospects of tangible insights into one of the premises of EWBG, in addition to the present climate of theoretical high energy physics, greatly foster the study of the mechanism in extensions of the SM.

In the context of EWBG, a widely employed criterion classifies the EWPhT as *strong* when the approximate inequality $v_{\text{pt}}/T_{\text{pt}} \gtrsim 1$ holds, with both the vacuum expectation value of the Higgs field v_{pt} and the temperature T_{pt} evaluated at the moment of the phase transition [27, 47, 73–75]. This thesis sets out to revisit and dissect the reliability of this condition in two BSM extensions of the Higgs sector: the Inert Doublet Model (IDM) and a canonical real scalar singlet extension (rSM). To this aim, the following itinerary is proposed:

- Part I covers a largely self-contained theoretical build-up to EWBG. Chapters 2 – 6 present a general review of the context, the relevant tools and selected ingredients of EWBG. Chapter 7 unifies these processes into the mechanism of EWBG and justifies the requirement for a SFOPhT.
- Part II specifies the theoretical methods and numerical procedures on which the subsequent analyses rest.
- Part III builds the IDM and the rSM in view of up-to-date experimental limits and goes on to explore the viability of SFOPhTs therein. The emphasis is placed on the reassessment of the condition $v_{\text{pt}}/T_{\text{pt}} \gtrsim 1$.

Chapter 2

Electroweak theory in the SM

Electroweak (EW) theory is the unified description of processes pertaining to the weak and electromagnetic interactions. In the SM, the mathematical groundwork for this description is provided by the Glashow-Weinberg-Salam (GWS) model [76–78]. The centerpiece of the GWS theory is the gauge group $SU(2)_L \times U(1)_Y$. Gauge invariance of a theory with fermions ψ under this group induces the existence of four gauge fields: one field B_μ arising from the $U(1)$ gauge symmetry under which the particles carry a weak hypercharge Y and three fields W_μ^a ($a \in \{1, 2, 3\}$) emerging from a $SU(2)$ gauge symmetry under which only the left-handed particles are charged. The model is completed by a complex $SU(2)_L$ Higgs doublet Φ ,

$$\Phi \stackrel{\text{def}}{=} \frac{1}{\sqrt{2}} \begin{pmatrix} \phi_1 + i\phi_2 \\ \phi_3 + i\phi_4 \end{pmatrix}. \quad (2.1)$$

The Lagrangian of EW theory is given by

$$\mathcal{L}_{\text{EW}} \stackrel{\text{def}}{=} \mathcal{L}_{\text{kin}} + \mathcal{L}_{\text{Yuk}} - V(\Phi). \quad (2.2)$$

\mathcal{L}_{kin} represents the kinetic terms of the theory¹,

$$\mathcal{L}_{\text{kin}} \stackrel{\text{def}}{=} -\frac{1}{4}W_{\mu\nu}^a W^{a\mu\nu} - \frac{1}{4}B_{\mu\nu}B^{\mu\nu} + (\mathcal{D}_\mu\Phi)^\dagger(\mathcal{D}^\mu\Phi) + \sum_j i\bar{\psi}_j\gamma^\mu\mathcal{D}_\mu\psi_j. \quad (2.3)$$

The gauge field terms in Eq. (2.3) follow the conventional definitions of the fields and the field strength tensors (see *e.g.* Ref. [79]),

$$W_\mu \stackrel{\text{def}}{=} \frac{1}{2}\sigma^a W_\mu^a \quad (2.4)$$

$$B_{\mu\nu} \stackrel{\text{def}}{=} \partial_\mu B_\nu - \partial_\nu B_\mu \quad (2.5)$$

$$W_{\mu\nu}^a \stackrel{\text{def}}{=} \partial_\mu W_\nu^a - \partial_\nu W_\mu^a + g_2\epsilon^{abc}W_\mu^b W_\nu^c, \quad (2.6)$$

¹ $\bar{\psi}_j \stackrel{\text{def}}{=} \psi_j^\dagger\gamma^0$.

with the Pauli matrices σ^a (Appendix [A](#)). The sum over j covers all fermions in the theory. EW theory distinguishes between so-called *left*- and *right*-handed fermions. These have different transformation properties under the gauge group. Left-handed leptons and quarks may transform as $SU(2)$ doublets expressed as

$$l^i \stackrel{\text{def}}{=} \begin{pmatrix} \nu_L^i \\ e_L^i \end{pmatrix}, \quad q^i \stackrel{\text{def}}{=} \begin{pmatrix} u_L^i \\ d_L^i \end{pmatrix}, \quad (2.7)$$

with i denoting the fermion generation, $i \in \{1, 2, 3\}$. Their right-handed counterparts^{[2](#)}

$$e_R^i, u_R^i, d_R^i \quad (2.8)$$

instead transform as singlets under $SU(2)$ and decouple altogether from its gauge bosons. The EW *covariant derivative* acting on the Higgs doublet and the left-handed fermion fields is

$$\mathcal{D}_\mu \stackrel{\text{def}}{=} \partial_\mu - ig_1 Y B_\mu - ig_2 W_\mu^a \tau^a, \quad (2.9)$$

with the generators τ^a corresponding to normalized Pauli matrices, $\tau^a = \sigma^a/2$, the gauge couplings parameters g_1 and g_2 , and Y denoting the weak hypercharge of the object acted upon. The right-handed particles instead have

$$\mathcal{D}_\mu \stackrel{\text{def}}{=} \partial_\mu - ig_1 Y B_\mu. \quad (2.10)$$

In the fermionic term of Eq. [\(2.3\)](#), the derivatives are contracted with the Dirac matrices γ^μ .

\mathcal{L}_{Yuk} accounts for the *Yukawa* interactions between the Higgs doublet and the fermions. It contains on the one hand the leptonic contribution

$$\mathcal{L}_{\text{Yuk}}^l \stackrel{\text{def}}{=} - \left(y_i^l \bar{l}^i \Phi e_R^i + \text{h.c.} \right), \quad (2.11)$$

which features the leptonic Yukawa couplings y_i^l . On the other hand, similar Yukawa terms are introduced for the quark sector. In the so-called *flavor basis*, these are

$$\mathcal{L}_{\text{Yuk}}^q \stackrel{\text{def}}{=} - \left(Y_{ij}^d \bar{q}^i \Phi d_R^j + Y_{ij}^u \bar{q}^i \tilde{\Phi} u_R^j + \text{h.c.} \right), \quad (2.12)$$

where $\tilde{\Phi} \stackrel{\text{def}}{=} i\sigma_2 \Phi$. The coupling structure is encoded in two non-diagonal Yukawa matrices Y_{ij}^d and Y_{ij}^u [\[80\]](#). Finally, the Lagrangian also features the Higgs potential

$$V(\Phi) \stackrel{\text{def}}{=} -\mu^2 \Phi^\dagger \Phi + \lambda (\Phi^\dagger \Phi)^2. \quad (2.13)$$

²The SM does not include right-handed neutrinos ν_R^i by construction.

Gauge symmetry under the group $SU(2)_L \times U(1)_Y$ characterizes the EW Lagrangian as invariant under the concatenation of certain local $U(1)$ and $SU(2)$ transformations (see *e.g.* Refs. [79–81] and Appendix A). The structure of the covariant derivative (2.9) is tailored to enforce the general gauge invariance of \mathcal{L}_{EW} under these transformations. Nonetheless, the GWS model crucially accounts for an instance of *spontaneous symmetry breaking* (SSB), whereby the initial symmetry group is reduced to a subset thereof at the vacuum, *i.e.* $SU(2)_L \times U(1)_Y \rightarrow U(1)_{\text{em}}$. This so-called Higgs mechanism [82–84] is realized by the spontaneous acquisition of a non-zero vacuum expectation value (VEV) $\langle \Phi \rangle = v/\sqrt{2}$ by the Higgs doublet. In the phase of broken EW symmetry³, the doublet is conventionally represented in a basis such that

$$\Phi = \frac{1}{\sqrt{2}} \begin{pmatrix} 0 \\ v + h \end{pmatrix}, \quad (2.14)$$

featuring an excitation with respect to the VEV v – the Higgs boson h . The ground state of the Lagrangian in Eq. (2.2) only remains invariant under transformations generated by the linear combination $Q = \tau^3 + Y$, Q being the generator of the $U(1)_{\text{em}}$ symmetry responsible for electromagnetic interactions. Its gauge field is the photon.

After symmetry breaking, the kinetic terms of the Higgs doublet give rise to

$$\begin{aligned} \mathcal{L}_{\text{kin}} &\supset \frac{1}{2} \begin{pmatrix} 0 & v \end{pmatrix} \begin{pmatrix} \frac{1}{2}g_1 B_\mu + g_2 W_\mu^a \tau^a \\ \frac{1}{2}g_1 B^\mu + g_2 W^{b,\mu} \tau^b \end{pmatrix} \begin{pmatrix} 0 \\ v \end{pmatrix} \\ &= \frac{1}{2} \frac{v^2}{4} \left(g_2^2 (W_\mu^1)^2 + g_2^2 (W_\mu^2)^2 + (-g_2 W_\mu^3 + g_1 B_\mu)^2 \right). \end{aligned} \quad (2.15)$$

Recasting the gauge fields in a convenient diagonal basis such that

$$W_\mu^\pm \stackrel{\text{def}}{=} \frac{1}{\sqrt{2}} (W_\mu^1 \mp iW_\mu^2) \quad (2.16)$$

$$Z_\mu \stackrel{\text{def}}{=} \frac{1}{\sqrt{g_1^2 + g_2^2}} (g_2 W_\mu^3 - g_1 B_\mu) \quad (2.17)$$

$$A_\mu \stackrel{\text{def}}{=} \frac{1}{\sqrt{g_1^2 + g_2^2}} (g_1 W_\mu^3 + g_2 B_\mu) \quad (2.18)$$

permits to identify the expressions in Eq. (2.15) as gauge field mass terms⁴ (Appendix A)

$$m_{W^\pm} = g_2 \frac{v}{2}, \quad m_Z = \sqrt{g_1^2 + g_2^2} \frac{v}{2}, \quad m_\gamma = 0. \quad (2.19)$$

³And in unitary gauge ($\xi = 0$).

⁴The photon will be referred to as γ despite the gauge field appearing as A_μ .

The two neutral fields A_μ and Z_μ are related to B_μ and W_μ^3 by

$$\begin{pmatrix} A_\mu \\ Z_\mu \end{pmatrix} = \begin{pmatrix} \cos \theta_W & \sin \theta_W \\ -\sin \theta_W & \cos \theta_W \end{pmatrix} \begin{pmatrix} B_\mu \\ W_\mu^3 \end{pmatrix}. \quad (2.20)$$

The mixing of B_μ and W_μ^3 is determined by the *Weinberg angle* θ_W . Its value can be captured by the relation [85]

$$\cos \theta_W = \frac{m_{W^\pm}}{m_Z}. \quad (2.21)$$

The Higgs mechanism also grants mass terms to the fermions. Symmetry breaking renders the leptonic Yukawa term

$$\mathcal{L}_{\text{Yuk}}^l \xrightarrow{\text{SSB}} -\frac{y_i^l}{\sqrt{2}}(v+h)(\bar{l}^i e_R^i + \text{h.c.}) \quad (2.22)$$

such that the charged lepton acquires a mass

$$m_{e^i} = \frac{y_i^l}{\sqrt{2}}v. \quad (2.23)$$

In the quark sector, a convenient *mass basis* allows to diagonalize the Yukawa matrices into appropriate matrices M_d and M_u for the down- and up-type quarks, with the respective diagonal components $y_i^{d,u}$ for $i \in \{1, 2, 3\}$. Under the Higgs mechanism, Eq. (2.12) becomes

$$\mathcal{L}_{\text{Yuk}}^q \xrightarrow{\text{SSB}} -(v+h) \left(\frac{y_i^d}{\sqrt{2}} \bar{d}'_L d'^i_R + \frac{y_i^u}{\sqrt{2}} \bar{u}'_L u'^i_R + \text{h.c.} \right) \quad (2.24)$$

with the mass terms

$$m_i^{d,u} = \frac{y_i^{d,u}}{\sqrt{2}}v \quad (2.25)$$

and the apostrophes denoting the quark fields in the mass basis. The misalignment of the mass and flavor states is quantified by the complex unitary Cabibbo-Kobayashi-Maskawa (CKM) matrix [86, 87]. The irreducible complex phase in this matrix is an experimentally verified source of CP violation in the SM [88-90].

Finally, the Higgs boson mass arises from the curvature of the potential (2.13) at its minimum as

$$m_h = \sqrt{2\lambda}v. \quad (2.26)$$

Chapter 3

Quantum field theory essentials

Much of the physics in Lagrangians like Eq. (2.2) is hidden in certain parameter relations. For example, in a ϕ^4 -theory with spontaneous symmetry breaking as encountered in Eq. (2.13), the parameter relations at the potential minimum ϕ_{\min} define the mass of the field. The significance of the potential minimum is somewhat more general in that it classically marks a minimum of the Minkowski action

$$\mathcal{S}_M[\phi] \stackrel{\text{def}}{=} \int d^4x \mathcal{L}(\phi). \quad (3.1)$$

This *classical* action sources the physics of a quantum field theory (QFT). An elegant way in which the physics can be invoked is provided by the path integral formulation of QFT. It rests on so-called *grand canonical partition functions* [91]

$$\mathcal{Z}[J] \stackrel{\text{def}}{=} \int \mathcal{D}\phi \exp \left[i \left(\mathcal{S}_M[\phi] + \int d^4x J(x)\phi(x) \right) \right] \quad (3.2)$$

where $\mathcal{D}\phi$ is the path integral measure and $J(x)$ an external current. $\mathcal{Z}[J]$ is also appropriately known as the *generating functional* of correlation functions: n functional derivatives of Eq. (3.2) with respect to $J(x)$ generate n -point correlation functions $G_{(n)}$ like the propagator ($n = 2$). This motivates the suggestive reexpression of $\mathcal{Z}[J]$ as [91]

$$\mathcal{Z}[J] = \sum_{n=0}^{\infty} \frac{i^n}{n!} \int d^4x_1 \dots d^4x_n J(x_1) \dots J(x_n) G_{(n)}(x_1, \dots, x_n). \quad (3.3)$$

A perturbative diagrammatic expansion of $\mathcal{Z}[J]$ allows to recover the physics of the system in terms of Feynman diagrams.

Corrections induced by loop diagrams will tend to complicate simple tree-level parameter relations at minima of \mathcal{S}_M . Hereby, the procedure of tying physical observables like the mass to critical points in the action becomes somewhat pathological. A mathematical remedy to the ills of the classical action becomes necessary;

going even further, perhaps a surrogate object altogether that allows to “read off”, for example, the vacuum state of the full, loop-corrected theory. The quantum effective action and the corresponding effective potential are precisely such objects and their importance to studies of SSB shall be motivated in this chapter for later use. This will simultaneously serve to settle basic concepts and conventions in QFT and finite-temperature field theory (FTFT) assumed throughout the rest of this work.

For most of the physically meaningful purposes, only a subset of the graphs generated by $\mathcal{Z}[J]$ is of interest – the so called *connected* diagrams. A tool that systematically removes disconnected graphs from the picture is the generating functional $\mathcal{W}[J]$ of connected n -point functions. Such a generating functional can be defined via

$$\mathcal{Z}[J] = \exp(i\mathcal{W}[J]) \iff \mathcal{W}[J] \stackrel{\text{def}}{=} -i\log(\mathcal{Z}[J]). \quad (3.4)$$

In analogy to the formalism for \mathcal{Z} , connected n -point correlation functions $G_{(n)}^c$ will emerge from n -th functional derivatives with respect to $J(x)$. Thus, $\mathcal{W}[J]$ also admits the suggestive expression [91]

$$i\mathcal{W}[J] = \sum_{n=0}^{\infty} \frac{i^n}{n!} \int d^4x_1 \dots d^4x_n J(x_1) \dots J(x_n) G_{(n)}^c(x_1, \dots, x_n). \quad (3.5)$$

The physics of connected diagrams is ultimately sourced by the so-called *quantum effective action* Γ_M , akin to \mathcal{S}_M in Eq. (3.1) in the classical formalism. Γ_M is obtained from $\mathcal{W}[J]$ via Legendre transformation to a suitable field coordinate defined as

$$\bar{\phi}(x) \stackrel{\text{def}}{=} \frac{\delta\mathcal{W}[J]}{\delta J(x)}. \quad (3.6)$$

$\bar{\phi}$ is a background or *mean* field which averages over quantum fluctuation effects. In terms of $\bar{\phi}$, the effective action is formally given by [91]

$$\Gamma_M[\bar{\phi}] \stackrel{\text{def}}{=} \mathcal{W}[J] - \int d^4x \bar{\phi}(x)J(x). \quad (3.7)$$

The definition in Eq. (3.7) possesses a number of interesting properties. First of all, it suggests the quantum field equation

$$\frac{\delta\Gamma_M[\bar{\phi}]}{\delta\bar{\phi}(x)} = -J(x). \quad (3.8)$$

For vanishing external currents $J(x)$, Eq. (3.8) identifies critical points of the action of the full, loop-corrected theory such as the vacuum state $\bar{\phi}_{\text{min}}$. This was the

primary motivation in introducing the effective action formalism. It is stressed that fields $\bar{\phi} = \bar{\phi}(x)$ which satisfy Eq. (3.8) in a translationally invariant theory will not depend on x , *i.e.* they are to be understood as *constant* background fields. A second property is suggested by an expansion of Γ_M as (91)

$$\Gamma_M[\bar{\phi}] = \sum_{n=0}^{\infty} \frac{1}{n!} \int d^4x_1 \dots d^4x_n \bar{\phi}(x_1) \dots \bar{\phi}(x_n) \Gamma_M^{(n)}(x_1, \dots, x_n). \quad (3.9)$$

The $\Gamma_M^{(n)}$ are one-particle irreducible (1PI) correlation functions and formally represent effective n -point vertices that take into account all possible quantum (loop) corrections. Eqs. (3.8) and (3.9) thus lay bare the full power of the effective action formalism: it serves to sweep into the vertices all of the quantum loop effects of a theory. In so doing, it confines many of the crucial physical aspects to a localized object of study, the *effective potential*.

The effective potential is paramount to model-building, as Parts II and III will showcase. The interactions it encodes are what define the physics of a QFT aside from the pertinent gauge symmetries of the model. Assuming a translation- and Lorentz-invariant theory, the effective potential can be interpreted as the surviving term in (91)

$$\begin{aligned} \Gamma_M[\bar{\phi}] &= \int d^4x \left(\mathcal{L}_{\text{kin}}(\bar{\phi}) - V_{\text{eff}}(\bar{\phi}) \right) \\ &= - \int d^4x V_{\text{eff}}(\bar{\phi}). \end{aligned} \quad (3.10)$$

In the last equality, the constancy of the fields cancels the kinetic derivative terms. Furthermore, it reduces the integral of Eq. (3.10) to a space-time volume factor and renders the expression (79)

$$\Gamma_M[\bar{\phi}] = -(V \cdot \mathcal{T}) V_{\text{eff}}(\bar{\phi}). \quad (3.11)$$

Eq. (3.11) shows that the formalism reconciles the critical points of Γ_M and V_{eff} . In particular, at the minima one recovers

$$\left. \frac{\partial}{\partial \bar{\phi}} \Gamma_M[\bar{\phi}] \right|_{\bar{\phi}=\bar{\phi}_{\text{min}}} = \left. \frac{\partial}{\partial \bar{\phi}} V_{\text{eff}}(\bar{\phi}) \right|_{\bar{\phi}=\bar{\phi}_{\text{min}}} = 0. \quad (3.12)$$

The last equation indicates SSB for $\bar{\phi}_{\text{min}} \neq 0$.

The availability of an expansion for Γ_M in Eq. (3.9) and the close relation between Γ_M and V_{eff} in Eq. (3.10) suggest a convenient expansion of V_{eff} itself. Indeed, in

momentum space, under the previous assumptions on the fields and the space-time symmetries, an effective potential can be expressed as [91]

$$V_{\text{eff}}(\bar{\phi}) = - \sum_{n=0}^{\infty} \frac{\bar{\phi}^n}{n!} \Gamma_M^{(n)}(p_i = 0), \quad (3.13)$$

thus as sum of effective vertices with vanishing external momenta p_i . In order to calculate an effective potential to loop order m , each effective vertex $\Gamma_M^{(n)}$ needs to account for the possible 1PI diagrams with vanishing external momenta and up to m loops. At zero-loop order, the fundamental tree-level potential V_{tree} of a theory is recovered. Following Eq. (3.13), the one-loop contribution is obtained when the $\Gamma_M^{(n)}$ account for all appropriate diagrams with up to one loop. This prescription results in the one-loop effective potential [91]

$$V_{\text{eff}}(\bar{\phi}) = V_{\text{tree}}(\bar{\phi}) + V_{\text{CW}}(\bar{\phi}), \quad (3.14)$$

with $V_{\text{CW}}(\bar{\phi})$ signifying the *Coleman-Weinberg* (CW) potential brought about by the one-loop corrections [92]. Radiative corrections such as the ones accounted for by the CW potential are known sources of SSB and hence need to be tracked when a model is set up. Chapter 8 will provide the necessary details to tackle the model setup in Chapters 10 and 11.

The path integral formulation of field theories followed throughout this chapter greatly lives off its analogy to statistical mechanics and thermodynamics. This analogy reflects, for example, in the extensive character of the effective action displayed in Eq. (3.11) [79]. The analogy has motivated the so-called *Euclidean* formulation of field theories typically encountered in¹ the study of *phase transitions* and nucleation theory, which shall be addressed in Chapter 6. The Euclidean formulation relies on a so-called Wick rotation of the temporal coordinate, *i.e.* $\tau \stackrel{\text{def}}{=} -it$. Under its effect, the fundamental quantity \mathcal{S}_M is redefined into its Euclidean version [93, 94]

$$\mathcal{S}_E[\phi] = -i\mathcal{S}_M[\phi] = \int d\tau \int d^3x \mathcal{L}(\phi). \quad (3.15)$$

This change then permeates the entire effective action formalism. In particular, it is noted for later purposes that the effective potential will be related to the Euclidean effective action $\Gamma_E = -i\Gamma_M$ as [95]

$$\Gamma_E[\bar{\phi}] = \int d\tau \int d^3x V_{\text{eff}}(\bar{\phi}). \quad (3.16)$$

¹But of general applicability.

This reformulation of field theory owes its name to the Euclidean space-time structure recovered under the Wick rotation. All space-time dimensions are thus widely treated on an equal footing, especially so in zero-temperature QFT. However, FTFT usually exploits this formulation in order to stress the analogy to thermodynamics and reinterpret many quantities as thermal averages. In Minkowski space-time, FTFT applications typically compactify the temporal variable to $t \in [0, -i\beta]$, with the inverse temperature $\beta = T^{-1}$; the Euclidean formalism instead utilizes the less cumbersome $\tau \in [0, \beta]$.

FTFT lends itself to an effective action formalism as outlined for the zero-temperature case. Besides introducing the pertinent thermal contributions to the potential, it generalizes the property (3.12) to thermal systems. Bridging the conceptual gaps in a sufficiently subtle re-derivation is beyond the scope of this work². However, thermal effects will play a crucial role in future chapters and need to be acknowledged at this point. At high temperatures, such effects can *restore* symmetries that appear spontaneously broken at low temperatures [97–100]. That is, a certain symmetry is regained when thermal effects overpower the effective potential (3.14) at zero temperature. Models presenting this behavior thus possess distinct symmetry phases between which they transition. In the SM, the EW sector is characterized by such a phase transition. Its exact nature is crucial to the viability of EWBG and will be addressed in Chapters 6 and 7. Implementational details of the CW and thermal effective potentials necessary to Part III are postponed until Chapter 8, and the corresponding finite-temperature Feynman rules can be retrieved in Appendix B. Finally, a point regarding notation: for the sake of clarity throughout the equations, background fields will not be distinguished graphically as $\bar{\phi}$ beyond this chapter.

²Readers are referred to Refs. [91, 95, 96] for excellent introductions to FTFT.

Chapter 4

Baryon number violation and Yang-Mills vacua

4.1 Violation of baryon number conservation in the SM

One of the fundamental requirements for baryogenesis is the violation of baryon number conservation – a condition the SM may seem at odds with: no perturbative process conceivable within the theory seems to violate this apparent conservation law. As baryon number violating events – such as proton decay – have yet to be observed, the experimental *status quo* is all but encouraging [38–43]. However, it turns out the SM possesses the tools to accommodate for baryon number violation via so-called anomalies. Anomalies manifest when symmetries of a Lagrangian are not shared by the functional measure of the theory. As a result, classical Noether conservation of certain currents may be violated at quantum level. A prime example is the Adler-Bell-Jackiw (ABJ) anomaly, which features the violation of the chiral current in a $U(1)$ theory with chiral fermions and is related to the non-zero amplitude of certain triangle diagrams [101, 102].

Crucially, anomalies permeate the EW sector of the SM. The so-called $(B + L)$ anomaly is the keystone to EWBG [103]. As the name suggests, it provides a pathway for the non-conservation of the joint baryon-lepton number $(B+L)$ and thus a backdoor to baryon number violation. A very general method for its evaluation is provided by the path integral approach [104, 105]. The starting point is the generating functional [30]

$$\mathcal{Z} = \int \mathcal{D}\Psi \mathcal{D}\bar{\Psi} e^{i \int d^4x \mathcal{L}_{EW}} = \int \mathcal{D}\Psi \mathcal{D}\bar{\Psi} e^{i\mathcal{S}}, \quad (4.1)$$

with the EW Lagrangian introduced in Chapter 2. A first inspection of the covariant derivative structure in \mathcal{L}_{EW} reveals the existence of baryonic and leptonic currents¹,

$$J_B^\mu = \sum_q \frac{1}{3} \bar{q} \gamma^\mu q \quad (4.2)$$

$$J_L^\mu = \sum_l (\bar{l} \gamma^\mu l + \bar{\nu}_l \gamma^\mu \nu_l). \quad (4.3)$$

They emerge as classical Noether currents of global field transformations of the fermions,

$$\Psi(x) \rightarrow e^{i(a+b\gamma_5)\theta} \Psi(x) \quad (4.4)$$

$$\bar{\Psi}(x) \rightarrow \bar{\Psi}(x) e^{i(a+b\gamma_5)\theta}, \quad (4.5)$$

with $\{a = \frac{1}{3}, b = 0\}$ corresponding to a baryon number rotation and $\{a = 1, b = 0\}$, to a lepton number rotation. Under these transformations, the generating functional (4.1) remains invariant. The physical manifestation of these symmetries is the apparent conservation of B and L .

Despite their solid grounding, these conservation laws break down beyond the classical setting [106]. Interesting quantum effects can be captured by treating the parameter θ in Eqs. (4.4) and (4.5) as a local quantity,

$$\Psi(x) \rightarrow e^{i(a+b\gamma_5)\theta(x)} \Psi(x) \quad (4.6)$$

$$\bar{\Psi}(x) \rightarrow \bar{\Psi}(x) e^{i(a+b\gamma_5)\theta(x)}. \quad (4.7)$$

By virtue of the equivalence theorem of QFTs, physics needs to remain invariant under such field redefinitions [107–109]; thus, no new result is expected. And yet, this change is deceptively innocent: under the new prescription, not only the Lagrangian but also the functional measure changes – and it does so in a non-trivial way. On account of the ABJ anomaly, the chiral components of the new transformations do not correspond to symmetries of the functional measure, rendering the Jacobian of the transformation non-trivial. Specifically, the transformed generating functional

$$\mathcal{Z}' = \int \mathcal{D}\Psi' \mathcal{D}\bar{\Psi}' e^{iS'} = \int \mathcal{D}\Psi \mathcal{D}\bar{\Psi} e^{\mathcal{S}_{\text{jac}}} e^{i(S+\delta S)} \quad (4.8)$$

¹Here the quark Dirac fields are denoted by q, \bar{q} . Those of the charged leptons go by l and \bar{l} ; those of neutrinos, by ν_l and $\bar{\nu}_l$.

features the new contributions [30, 75]

$$\delta\mathcal{S} = - \int d^4x \left[\bar{\Psi}(x) m (e^{2ib\gamma_5\theta(x)} - 1) \Psi(x) + \bar{\Psi}(x) \gamma^\mu (a + b\gamma_5) \Psi(x) \partial_\mu \theta(x) \right] \quad (4.9)$$

and

$$\mathcal{S}_{\text{jac}} = i \int d^4x \theta(x) \left[\frac{(a-b)}{8\pi^2} \text{Tr}[F^{(L)\mu\nu} \tilde{F}_{\mu\nu}^{(L)}] - \frac{(a+b)}{8\pi^2} \text{Tr}[F^{(R)\mu\nu} \tilde{F}_{\mu\nu}^{(R)}] \right]. \quad (4.10)$$

Here, m is the nominal fermion mass; $F^{(L)\mu\nu}$ and $F^{(R)\mu\nu}$ are the generic field strengths coupling to left- and right-handed currents (*i.e.* $\{W^{\mu\nu}, B^{\mu\nu}\}$ and $B^{\mu\nu}$, respectively), and $\tilde{F}_{\mu\nu} = \frac{1}{2}\epsilon_{\mu\nu\rho\sigma} F^{\rho\sigma}$ defines the dual field strength tensors. Partial integration of Eq. (4.9) removes any dependence on $\partial_\mu \theta(x)$ and, on the whole, the invariance condition for the generating functional can be made independent of $\theta(x)$

[30]:

$$\begin{aligned} \partial^\mu \left[\bar{\Psi}(x) \gamma_\mu (a + b\gamma_5) \Psi(x) \right] &\stackrel{!}{=} -2ibm \bar{\Psi}(x) \gamma_5 \Psi(x) \\ &\quad - i \frac{(a-b)}{8\pi^2} \text{Tr}[F^{(L)\mu\nu} \tilde{F}_{\mu\nu}^{(L)}] + i \frac{(a+b)}{8\pi^2} \text{Tr}[F^{(R)\mu\nu} \tilde{F}_{\mu\nu}^{(R)}]. \end{aligned} \quad (4.11)$$

For the tuples $\{a, b\}$ introduced earlier, the left-hand side of Eq. (4.11) gives the baryonic and leptonic current divergences $\partial_\mu J_B^\mu$ and $\partial_\mu J_L^\mu$. The right-hand side, however, only vanishes if $a = b = 0$. Therefore, the generating functional cannot be invariant under Eqs. (4.6) and (4.7) and the current divergences must be distinct from zero. In fact, it can be shown that [75]

$$\partial_\mu J_B^\mu = i \frac{N_F}{32\pi^2} (-g_2^2 W^{a\mu\nu} \tilde{W}_{\mu\nu}^a + g_1^2 B^{\mu\nu} \tilde{B}_{\mu\nu}) \quad (4.12)$$

$$\partial_\mu J_L^\mu = i \frac{N_F}{32\pi^2} (-g_2^2 W^{a\mu\nu} \tilde{W}_{\mu\nu}^a + g_1^2 B^{\mu\nu} \tilde{B}_{\mu\nu}), \quad (4.13)$$

with N_F the number of fermion families and the coupling and tensor conventions of Chapter 2. The baryonic and leptonic currents are each not conserved – which discards B and L as fundamentally conserved charges. Furthermore, it is noted that the conservation of both charges is violated by the same quantity. Thus, it is natural to consider the joint currents $J_{B\pm L}^\mu = J_B^\mu \pm J_L^\mu$. They behave as

$$\partial_\mu J_{B+L}^\mu = i \frac{N_F}{16\pi^2} (-g_2^2 W^{a\mu\nu} \tilde{W}_{\mu\nu}^a + g_1^2 B^{\mu\nu} \tilde{B}_{\mu\nu}) \quad (4.14)$$

$$\partial_\mu J_{B-L}^\mu = 0, \quad (4.15)$$

therefore suggesting the violation of $(B+L)$ and the conservation of $(B-L)$. Baryon number violation ΔB is thus very much feasible within the SM and arises naturally in processes where $(B+L)$ is violated: since the baryon number can be decomposed into orthogonal components as

$$B = \frac{(B+L)}{2} + \frac{(B-L)}{2}, \quad (4.16)$$

the conservation of $(B-L)$ implies

$$\Delta B = \frac{\Delta(B+L)}{2}. \quad (4.17)$$

Any physical process able to couple to and violate the conservation of $(B+L)$ will in turn violate the conservation of B .

4.2 $SU(2)$ and its vacuum structure

The results of the previous subsection are in fact not just a happy accident² but symptomatic of a profound misunderstanding. In order to emphasize the situation, the baryonic divergence³ may be recast in terms of derivatives,

$$\partial_\mu J_B^\mu = i \frac{N_F}{32\pi^2} (-g_2^2 \partial_\mu K^\mu + g_1^2 \partial_\mu k^\mu), \quad (4.18)$$

with the definitions ^[75]

$$k^\mu \stackrel{\text{def}}{=} 2\epsilon^{\mu\nu\alpha\beta} (\partial B_\alpha B_\beta) \quad (4.19)$$

$$K^\mu \stackrel{\text{def}}{=} 2\epsilon^{\mu\nu\alpha\beta} (\partial_\nu W_\alpha^a W_\beta^a - \frac{1}{3} g_2 \epsilon_{abc} W_\nu^a W_\alpha^b W_\beta^c). \quad (4.20)$$

The quantities k^μ and K^μ will be related to the vacuum structures of the $U(1)$ and $SU(2)$ sectors, respectively. A typical treatment of Eq. ^(4.18) would involve a redefinition of the current J_B^μ set out to cancel any boundary terms arising from the integration of $\partial_\mu J_B^\mu$. Thereby, Eq. ^(4.18) would vanish altogether and suggest the conservation of B after all. While such a procedure is well-behaved for the term $\partial_\mu k^\mu$, it does not hold for the term $\partial_\mu K^\mu$, as the exotic vacuum structure of the $SU(2)$ sector renders its boundary contributions inherently non-trivial.

²As opposed to the ‘‘accidental symmetry’’ that the conservation of B would entail ^[110].

³And of course all other divergences derived in the previous subsection.

A general feature of Yang-Mills theories is their rich vacuum topology as compared to that of abelian theories [111–115]. A naive but natural guess as to the Yang-Mills vacuum would be $W_j^{\text{vac}}(x) = 0$, which causes the $SU(2)$ kinetic terms in Eq. (2.3) to vanish. However, in line with the gauge transformation behaviour defined in Eq. (A.13), the nominal vacuum is not unique, and the family of pure gauge images defined by

$$W_j^{\text{vac}}(x) = \frac{i}{g_2} U(x) \partial_j U^\dagger(x) \quad (4.21)$$

with $SU(2)$ matrices $U(x)$ features infinitely many degenerate ground states. These states all seem *a priori* physically identical, merely differing in a perceived mathematical artifact. Similarly, one could think of a particle living on a circle with a designated ground state, as in Fig. 4.1: after a full trajectory along the circle, the particle lands on the same ground state [75, 114].

This notion of the Yang-Mills vacuum is fundamentally erroneous: different classes of vacua can be identified which need to be treated as separate, distinguishable entities, akin to counting the integer-valued *winding number* of the particle on the circle. To show this, the following discussion will be limited to the subset of gauge transformations $U(x)$ such that

$$U(x) \rightarrow 1 \text{ as } |x| \rightarrow \infty \quad (4.22)$$

(or, more generally, some constant, unitary matrix as $|x| \rightarrow \infty$ [114]). This condition pursues one goal: it restricts the argument to vacuum states separated by finite actions, which are the ones of interest⁴. In so doing, it compactifies the original

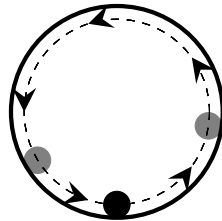


Figure 4.1: A particle living on a circle, with the ground state at the bottom. If the particle has enough energy to perform a full rotation, it lands on a physically identical vacuum with a different winding number. Adapted from Ref. [114].

⁴As transitions only happen between such vacua.

coordinate space upon its projection⁵ onto $SU(2)$ group space via $U(x)$. As now both $\mathbb{R}^4 \sim S^3$ and $SU(2) \sim S^3$, it follows that the functions $U(x)$ represent mappings

$$U(x) : S_{\text{dom}}^3 \rightarrow S_{\text{range}}^3. \quad (4.23)$$

Such mappings possess a very general property: they cover S_{range}^3 n -times upon one closed *loop* over S_{dom}^3 . The number n of coverings or *windings* induces a natural classification of the mappings into different topological, so-called *homotopy* classes.

Mappings $U(x)$ within the same homotopy class are homotopically equivalent: they can be continuously deformed into each other without changes to the fundamental properties of the object. In particular, the number of coverings n they induce on S_{range}^3 – formally, the *topological degree* of the mapping – is left untouched [115]. n thus acts as a conserved topological charge; all $U_n(x)$ sharing the same charge define one and the same ground state in Eq. (4.21). Gauge mappings in different homotopy classes, however, will define topologically inequivalent ground states, *i.e.* ground states associated to different charges n and m . Integers and integer charges cannot be continuously transformed into each other. Therefore, if transitions between homotopically distinct vacua occur, they will sweep non-vacuum configurations on field space along the way [116]. This justifies the quasiperiodic vacuum structure of Yang-Mills theories portrayed in Fig. 4.2. A slightly pedantic point is in order which should help maintain formal clarity: one needs to distinguish between the charge n of the object $U_n(x)$ – a gauge transformation acting on some state which may be different from $W_j^{\text{vac}}(x) = 0$, as per Eq. (A.13) – and the topological charge of the vacuum state thereby defined via Eq. (4.21).

It is now possible to address the opening issue of this subsection. In Eq. (4.18), the divergence of the baryonic current was rewritten in terms of two convenient quantities, K^μ and k^μ . These quantities are the so-called *Chern-Simons currents* of the $SU(2)$ and $U(1)$ sectors and define the corresponding Chern-Simons (CS) charges [75, 106]

$$N_{CS} \stackrel{\text{def}}{=} \frac{g_2^2}{32\pi^2} \int d^3x K^0(x) \quad (4.24)$$

$$n_{CS} \stackrel{\text{def}}{=} \frac{g_1^2}{32\pi^2} \int d^3x k^0(x). \quad (4.25)$$

⁵ $U(x) : \mathbb{R}^4 \rightarrow SU(2)$ group space. Furthermore, $SU(2) \sim S^3$ on account of the $su(2)$ Lie algebra.

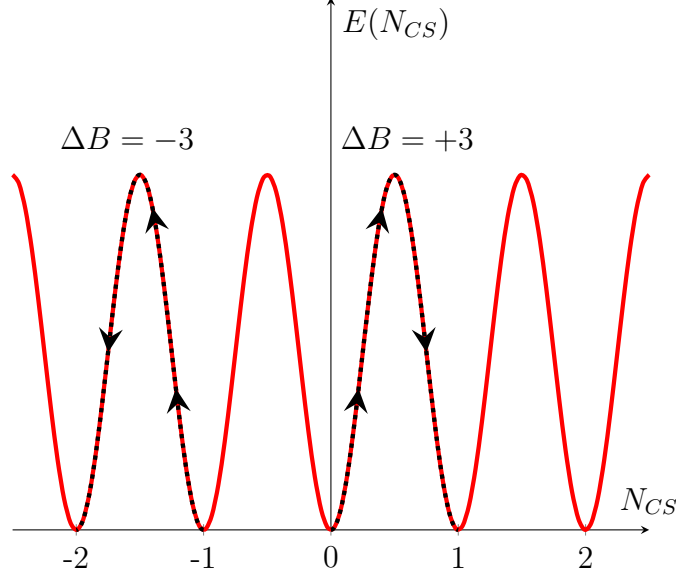


Figure 4.2: Energy of the gauge field configuration as a function of N_{CS} . Transitions between the ground states bring about a change in the system's charge N_{CS} . The difference can be positive or negative. Hence, the change in B is also sign-dependent. Adapted from Refs. [74, 114].

N_{CS} reflects the topological charge of the Yang-Mills vacua: for each vacuum defined by a class of mappings $U_n(x)$, Eq. (4.24) delivers the charge $N_{CS} = n$. For a transition between two vacua defined by the classes of mappings $U_n(x)$ and $U_m(x)$, $n \neq m$, arises a change $\Delta N_{CS} = n - m$. The latter cannot emerge in the topologically trivial abelian case, *i.e.* $\Delta n_{CS} = 0$.

Defining the baryonic charge as

$$B \stackrel{\text{def}}{=} i \int dt \int d^3x \partial_\mu J_B^\mu, \quad (4.26)$$

one gathers from Eq. (4.18) that a transition between vacuum states in a finite time interval $\Delta t = t_f - t_i$ results in a net violation of baryonic charge conservation by

$$\begin{aligned} \Delta B &= i \int_{t_i}^{t_f} dt \int d^3x \partial_\mu J_B^\mu \\ &= \frac{N_F}{32\pi^2} \int_{t_i}^{t_f} dt \int d^3x (g_2^2 \partial_\mu K^\mu - g_1^2 \partial_\mu k^\mu) \\ &\stackrel{(*)}{=} \frac{N_F}{32\pi^2} \left[\int d^3x (g_2^2 K^0 - g_1^2 k^0) \right] \Big|_{t_i}^{t_f} \\ &= N_F \cdot (\Delta N_{CS} - \Delta n_{CS}) \\ &= N_F \cdot \Delta N_{CS}. \end{aligned} \quad (4.27)$$

At (*) it is assumed the calculation is carried out in a gauge such that the spatial components K_i vanish at infinity; the non-triviality of the $SU(2)$ vacuum is thus swept into K^0 altogether [116]. For transitions between adjacent minima and assuming the SM fermion content, one obtains a violation of the baryon and lepton numbers by three units, $\Delta B = \Delta L = \pm 3$. Thus, such transitions violate the composite charge $B + L$ by $\Delta(B + L) = \pm 6$.

The last few pages should sufficiently motivate the interest in processes by which such vacuum transitions take place: so far, they are the only known baryon number violating processes within the mathematical architecture of the SM. Nonetheless, one important question remains open – namely, the exact transition process. Naively, two scenarios are possible. On the one hand, one should consider quantum tunneling between the vacua of Fig. 4.2. These transitions correspond to so-called *instanton* processes in the $SU(2)$ EW sector, which have been widely investigated. With an amplitude the order of 10^{-173} , their suppression is manifest [103]. There also exists the possibility of classical, thermally-aided trajectories over the barrier. Such is the class of the sphaleron process which this work studies.

Chapter 5

The electroweak sphaleron

The sphaleron is a field configuration which catalyzes transitions between the topologically distinct Yang-Mills ground states. In Fig. 4.2, it would correspond to half-integer states and sit on top of the barrier. More precisely though, the sphaleron is a saddle-point in field configuration space \mathcal{C} (hence its name, Greek for “ready to fall” [75]). It needs to be understood as the least-energy configuration interpolating between vacuum states atop a multidimensional potential barrier, as represented by Fig. 5.1.

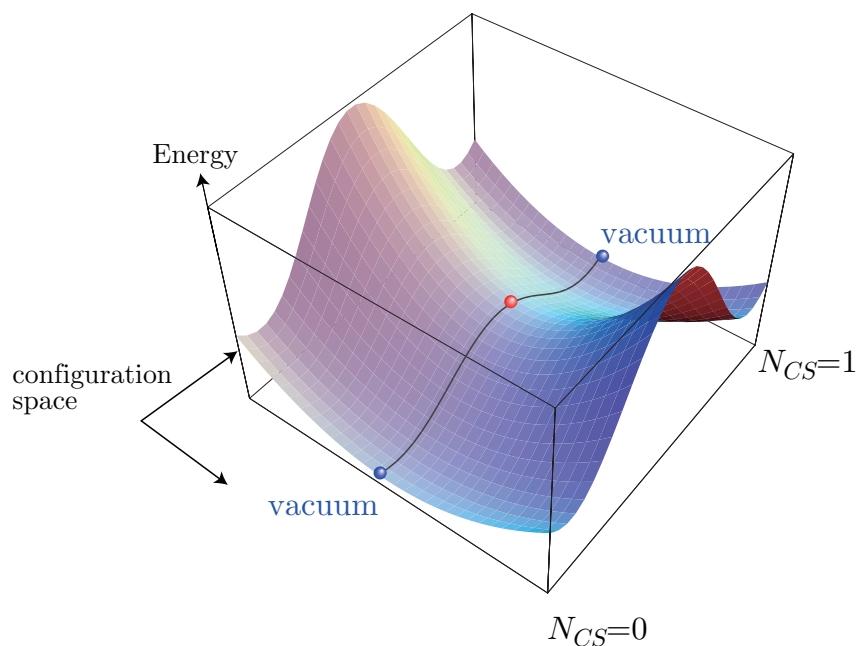


Figure 5.1: The sphaleron configuration (red) corresponds to the lowest-energy mountain pass between adjacent minima in the Yang-Mills potential, quasiperiodic as a function of the Chern-Simons number N_{CS} [30, 117]. (Copyright ©Koichi Funakubo)

Revealing the existence of saddle-points of the energy on \mathcal{C} was the great achievement of Ref. [54]. At its core, the proof consists in showing that \mathcal{C} is topologically equivalent to a manifold M of non-zero genus (*i.e.* with holes, as in Fig. 5.2). This follows from the existence of non-contractible loops of mappings on \mathcal{C} and ties in closely with the vacuum structure described in Chapter 4. Yang-Mills vacuum states associated to different topological charges n and n' are connected by trajectories on \mathcal{C} which topologically correspond to loops that wind the hole $\Delta n = |n - n'|$ times. For $\Delta n = 1$, there exist loops that correspond to transition trajectories between adjacent ground states separated by the potential barrier, as depicted in Fig. 5.1. The path of least action crosses the barrier along the lowest-energy mountain pass, *i.e.* the static, lowest energy configuration atop the barrier. This configuration corresponds to the EW sphaleron. This section will outline its mathematical structure, closely following the original construction in Ref. [54] as well as two more pedagogical reviews thereof in Refs. [115, 118]. Additional details can be inferred from Appendix E.

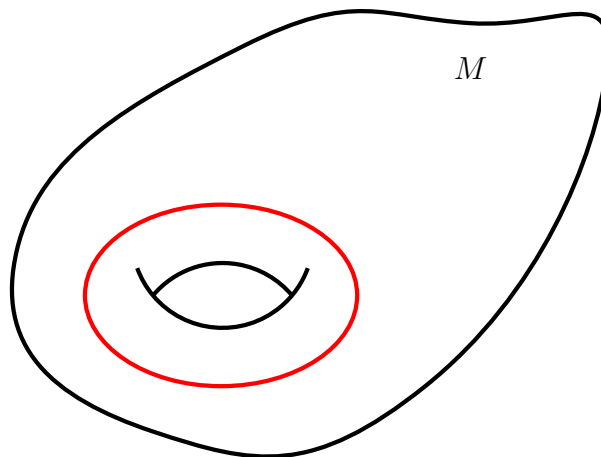


Figure 5.2: Manifold M with a hole. In red, a *non-contractible loop* on M , *i.e.* a loop which cannot not be homotopically contracted into a single point.

5.1 Sphaleron field configuration

The character of the SM EW sphaleron is governed by the standard Higgs doublet Φ and the three $SU(2)$ gauge fields W_μ^a , whereas the fermion fields are largely negligible. Furthermore, the initial discussion will be restricted to a pure $SU(2)$ sphaleron, whereby the mixing angle θ_W and therefore g_1 are assumed to vanish. Thus, the $U(1)_Y$ field B_μ decouples and can be set to zero for the present purposes, as can the corresponding field strength tensor. Strictly speaking, this assumption is justified *a posteriori* given the negligible effects induced by B_μ . At any rate, this ansatz will be amended later on for the sake of completeness and in order to account for the physical mixing angle. For now, the bosonic EW Lagrangian is truncated to

$$\mathcal{L} = -\frac{1}{4}W_{\mu\nu}^a W^{a\mu\nu} + (\mathcal{D}_\mu\Phi)^\dagger(\mathcal{D}^\mu\Phi) - V(\Phi), \quad (5.1)$$

with the tensor and covariant derivative structures introduced in Chapter 2. The Higgs doublet is evaluated in unitary gauge and in the conventional basis that sees

$$\Phi = \frac{1}{\sqrt{2}} \begin{pmatrix} 0 \\ h \end{pmatrix}, \quad (5.2)$$

where h is the CP-even component that obtains a vacuum expectation value v in the phase of broken EW symmetry. The SM tree-level Higgs potential introduced in Eq. (2.13) and appearing in Eq. (5.1) can then be expressed as

$$V(\Phi) = \lambda \left(\Phi^\dagger\Phi - \frac{1}{2}v^2 \right)^2 \quad (5.3)$$

and the Lagrangian is fully characterized. This minimal approach to the EW sphaleron defines the static energy functional [54]

$$\mathcal{E}[W_\mu^a, \Phi] \stackrel{\text{def}}{=} \int d^3x \left[\frac{1}{4}W_{ij}^a W^{aij} + (\mathcal{D}_i\Phi)^\dagger(\mathcal{D}^i\Phi) + V(\Phi) \right], \quad (5.4)$$

with $\{a, i, j = 1, 2, 3\}$, on the infinite-dimensional manifold of field configuration space \mathcal{C} . While the functional (5.4) sets the stage, the prescription for a saddle-point in configuration space is incomplete without a field ansatz. Ansätze usually presuppose some degree of understanding of the fields, which in this case may not be entirely intuitive. However, a first-principle reexamination of the theory will provide a number of helpful insights [54, 115, 118].

First of all, physicality of the sphaleron field configuration requires finiteness of its energy. This is accomplished if the fields reach their known vacuum values at spatial infinity. Secondly, it is necessary to partly fix the gauge. Otherwise, there will always exist a flat direction on \mathcal{C} associated to the gauge symmetry for every field configuration, thus rendering saddle-point searches inherently pathological. Both requirements are best implemented in spherical coordinates (ξ, θ, ϕ) , with $\xi = g_2 v r$ a convenient radial coordinate. A radial gauge condition – which will be relaxed later – has the gauge fields satisfy $W_\xi^a = 0$ everywhere; their remaining components will start at the canonical vacuum and need to reach an adjacent gauge image of the vacuum at spatial infinity. Similarly, the Higgs field h needs to converge to v at spatial infinity. A useful piece of notation defines the Higgs doublet at infinity as

$$\Phi^\infty(\theta, \phi) \stackrel{\text{def}}{=} \lim_{\xi \rightarrow \infty} \Phi(\xi, \theta, \phi). \quad (5.5)$$

The boundary condition on h requires the 2-manifold defined by (5.5) to fulfill

$$|\Phi^\infty(\theta, \phi)| = \frac{v}{\sqrt{2}} \quad (5.6)$$

for all θ and ϕ . While this greatly constrains the behaviour of Φ^∞ , it is not yet uniquely defined. A last gauge freedom is exhausted by requiring

$$\Phi^\infty(\theta = 0, \phi) \stackrel{\text{def}}{=} \frac{v}{\sqrt{2}} \begin{pmatrix} 0 \\ 1 \end{pmatrix}, \quad (5.7)$$

which is identified with Eq. (5.2) for $\langle h \rangle = v$ and thus uniquely fixes the Higgs vacuum configuration. The canonical vacuum of the theory is thus given by

$$W_{\text{vac}}(\xi, \theta, \phi) = 0 \quad , \quad \Phi_{\text{vac}}(\xi, \theta, \phi) = \frac{v}{\sqrt{2}} \begin{pmatrix} 0 \\ 1 \end{pmatrix}. \quad (5.8)$$

The non-contractible loop on \mathcal{C} of Higgs vacuum manifold configurations at infinity is given by (5.4)

$$\Phi^\infty(\theta, \phi; \mu) \stackrel{\text{def}}{=} \begin{pmatrix} \Phi_1^\infty \\ \Phi_2^\infty \end{pmatrix} = \frac{v}{\sqrt{2}} \begin{pmatrix} \sin \mu \sin \theta e^{i\phi} \\ e^{-i\mu} (\cos \mu + i \sin \mu \cos \theta) \end{pmatrix}. \quad (5.9)$$

It takes an external loop parameter $\mu \in [0, \pi]$ and thus starts and ends at (5.7). When the gauge is completely fixed, Eq. (5.9) describes a loop from and to one identical vacuum. It can be reinterpreted as the path in Fig. 5.1 that attains the sphaleron configuration for some μ by lifting the radial gauge condition on the W^a .

For all choices of $\{\theta, \phi, \mu\}$, Φ^∞ needs to be a finite-energy configuration. This constrains the asymptotic behaviour of the kinetic terms of Φ^∞ . In particular, it implies the angular covariant derivatives [54, 118]

$$\mathcal{D}_\theta \Phi^\infty(\theta, \phi; \mu) = 0 \quad \mathcal{D}_\phi \Phi^\infty(\theta, \phi; \mu) = 0. \quad (5.10)$$

Generality of Eqs. (5.10) holds if the covariant derivatives, and thus the corresponding components of the gauge fields, meet a certain structure. The $U(2)$ matrix

$$U^\infty(\theta, \phi; \mu) \stackrel{\text{def}}{=} \frac{\sqrt{2}}{v} \begin{pmatrix} \Phi_2^{\infty*} & \Phi_1^\infty \\ -\Phi_1^{\infty*} & \Phi_2^\infty \end{pmatrix}, \quad (5.11)$$

defined such that

$$\Phi^\infty(\theta, \phi; \mu) = \frac{v}{\sqrt{2}} U^\infty(\theta, \phi; \mu) \begin{pmatrix} 0 \\ 1 \end{pmatrix} \quad (5.12)$$

for all θ, ϕ and μ , provides the necessary ingredient. The angular components of the ‘pure’ gauge field at spatial infinity can be fixed as¹

$$W_\theta^\infty(\theta, \phi; \mu) \stackrel{\text{def}}{=} -\frac{i}{g_2} \partial_\theta U^\infty (U^\infty)^{-1} \quad W_\phi^\infty(\theta, \phi; \mu) \stackrel{\text{def}}{=} -\frac{i}{g_2} \partial_\phi U^\infty (U^\infty)^{-1} \quad (5.13)$$

and make sure that Eqs. (5.10) are met². The tools at hand allow for a general ansatz of the Higgs and gauge fields as [54]

$$\Phi(\xi, \theta, \phi; \mu) = h(\xi) \Phi^\infty(\theta, \phi; \mu) + (1 - h(\xi)) \frac{v}{\sqrt{2}} \begin{pmatrix} 0 \\ e^{-i\mu} \cos \mu \end{pmatrix} \quad (5.14)$$

$$W_\xi(\xi, \theta, \phi; \mu) = 0 \quad (5.15)$$

$$W_\theta(\xi, \theta, \phi; \mu) = f(\xi) W_\theta^\infty(\theta, \phi; \mu) \quad (5.16)$$

$$W_\phi(\xi, \theta, \phi; \mu) = f(\xi) W_\phi^\infty(\theta, \phi; \mu). \quad (5.17)$$

With this choice of functions, and omitting the explicit radial dependence of f and h for the sake of clarity, the energy functional (5.4) can be rewritten as [30]

$$\begin{aligned} \mathcal{E}(\mu) = & \frac{4\pi v}{g_2} \int_0^\infty d\xi \sin^2 \mu \left\{ \left[4 \left(\frac{df}{d\xi} \right)^2 + \frac{8}{\xi^2} [f(1-f)]^2 \sin^2 \mu \right] + \frac{\xi^2}{2} \left(\frac{dh}{d\xi} \right)^2 \right. \\ & + [h(1-f)]^2 - 2h(1-h)f(1-f) \cos^2 \mu + (1-h)^2 f^2 \cos^2 \mu \\ & \left. + \frac{\lambda}{4g_2^2} \xi^2 (h^2 - 1)^2 \sin^2 \mu \right\} \quad (5.18) \end{aligned}$$

¹The condition of $U(x)$ being an $SU(2)$ matrix is lifted [54]: the loop in \mathcal{C} along vacua of the Higgs doublet and between $SU(2)$ vacua sweeps non-vacuum states of the latter, as discussed in Chapter 4.

²An explicit proof can be recovered in *e.g.* Ref. [118].

in agreement with Ref. [54]. The fields should be well-defined at the origin. Furthermore, the ansatz needs to behave as expected at spatial infinity, *i.e.* converge to the desired vacuum configuration of the fields, such that the sphaleron energy attain a finite value. This motivates the boundary conditions

$$\lim_{\xi \rightarrow 0} h(\xi) = 0 \qquad \lim_{\xi \rightarrow 0} \frac{1}{\xi} f(\xi) = 0 \qquad (5.19)$$

$$\lim_{\xi \rightarrow \infty} h(\xi) = 1 \qquad \lim_{\xi \rightarrow \infty} f(\xi) = 1, \qquad (5.20)$$

which fully characterize the sphaleron and its energy. The value of μ emerges from the requirement that it deliver a configuration along the loop of Φ^∞ atop the potential barrier. Ref. [54] showed this will in general be the case for $\mu = \pi/2$, as it maximizes the terms³ in \mathcal{E} and thus marks the barrier top along the path between vacua. This further characterizes sphalerons as field configurations with half-integer N_{CS} sitting midway between states of integer-valued N_{CS} [55].

The radial field profiles f and h corresponding to the mountain pass of minimal energy – thus, a saddle-point – are obtained by solving the Euler-Lagrange equations that follow from Eq. (5.18) [55]:

$$\begin{aligned} \xi^2 \frac{d^2 f}{d\xi^2} &= 2f(1-f)(1-2f) - \frac{\xi^2}{4} h^2(1-f) \\ \frac{d}{d\xi} \left(\xi^2 \frac{dh}{d\xi} \right) &= 2h(1-f)^2 + \frac{\lambda}{g_2^2} \xi^2 (h^2 - 1)h. \end{aligned} \qquad (5.21)$$

This set of equations is yet to be solved analytically. Integration of approximate solution ansätze and numerical solutions to the field equations as shown in Fig. (5.3) place the sphaleron energy for the tree-level SM in the range 9 – 10 TeV [30]. Slight shifts to, in general, lower energies will arise in the presence of a non-vanishing $U(1)$ field. Introducing a profile function $q(\xi)$ for the $U(1)$ field, such shifts can be calculated perturbatively as [55]

$$\Delta \mathcal{E} = -\frac{\pi}{3} \frac{g_1^2 v}{g_2^3} \int_0^\infty d\xi \xi^2 h^2(\xi) [1 - f(\xi)] q(\xi). \qquad (5.22)$$

Details on the $U(1)$ corrections can be found in Appendix E.

³Although, as the original paper states, this might not hold for all terms for contrived choices of f and h [54]. After all, and as Ref. [119] notes, the original construction proves the existence of a sphaleron in EW theory, *i.e.* the canonical sphaleron presented here and generally considered for EWBG in the literature; it does not rule out the existence of other sphaleron-like solutions or saddle-points of \mathcal{E} . At any rate, neither f , h nor μ are to be understood as a free choices in the standard construction, but as consequences of the saddle-point condition on \mathcal{E} .

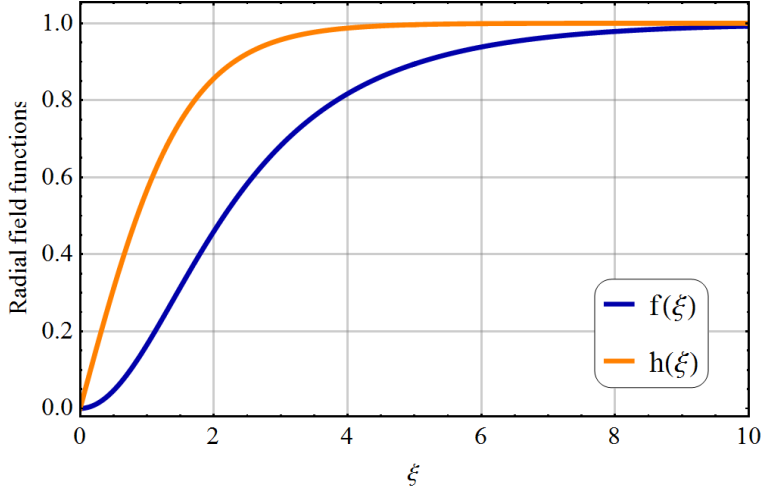


Figure 5.3: Field profiles $f(\xi)$ and $h(\xi)$ in the tree-level SM as a function of the dimensionless radial coordinate $\xi = g_2 vr$. These curves were obtained using a relaxation algorithm (see Chapter 9).

Although this section has introduced the sphaleron at zero temperature, this work is mainly interested in both its energy and its effects at finite temperature. The calculation of \mathcal{E} at finite temperature is straightforward from Eq. (5.18), merely requiring the replacements of v and $V(\phi)$ by their temperature-dependent equivalents. Thermal effects, however, raise additional questions. Sphalerons are phenomenologically bound to the phase of broken EW symmetry [75]. They are saddle-points of Eq. (5.4) featuring a doublet $\langle \Phi \rangle \neq 0$, a feature not shared by the EW symmetric phase. The nominal “sphaleron” configuration does not exist in this phase, yet potential barriers between the $SU(2)$ vacua still do. They must still exist, as the $SU(2)_L$ vacua remain topologically distinct. Despite the lack of a sphaleron configuration, transitions do still take place in the symmetric phase by means of gauge field configurations which, as the sphaleron, are able to prompt $\Delta N_{CS} = 1$. In line with the general lack of semantic nuance found in the literature, this work will be generous in its use of nomenclature and still refer to “sphalerons” when discussing transitions before EWSB.

5.2 The sphaleron rate

In Chapter 4, the late assumption that over-the-barrier transitions can deliver a statistically meaningful source of baryon number violation provided the motivation

behind the present chapter. The rate of such processes thus requires closer inspection. In the symmetric phase, transitions between $SU(2)_L$ vacua are particularly enhanced. On dimensional grounds, their rate per volume can be derived as [75]

$$\frac{\Gamma_{\text{sph}}^{\text{s}}}{V} \sim \alpha_W^4 T^4, \quad (5.23)$$

although more recent lattice calculations suggest up to $\sim \alpha_W^5 T^4$ [120, 121]. In the phase of broken symmetry, semi-classical calculations are a typical procedure: a sphaleron process can be modeled as a particle on top of a potential barrier overcoming the latter in the correct direction. This approach, which yields [56, 122]

$$\begin{aligned} \frac{\Gamma_{\text{sph}}^{\text{b}}}{V} &\approx \frac{\omega_-}{2\pi} \mathcal{N}_{\text{tr}}(\mathcal{N}_{\text{rot}} \mathcal{V}_{\text{rot}}) \left(\frac{\alpha_W T}{4\pi} \right)^3 \alpha_{W,T}^{-6} \kappa e^{-\mathcal{E}(T)/T} \\ &= \left[2\mathcal{N}_{\text{tr}}(\mathcal{N}_{\text{rot}} \mathcal{V}_{\text{rot}}) \frac{\omega_-}{g v(T)} \right] T^4 \left(\frac{\alpha_W}{4\pi} \right)^4 \left(\frac{4\pi v(T)}{g T} \right) \kappa e^{-\mathcal{E}(T)/T}, \end{aligned} \quad (5.24)$$

suffices to characterize the relation of the sphaleron rate and its energy⁴. Such calculations require a careful treatment of the underlying symmetries of the system – this is the origin of the normalization factors \mathcal{N}_{tr} and \mathcal{N}_{rot} , as well as of the volume factor of the rotation group $\mathcal{V}_{\text{rot}} = 8\pi^2$. The rate (5.24) also features $\alpha_W = g_2^2/4\pi$, which is the weak fine structure constant at zero temperature, which evaluates to $\alpha_{W,T} = \alpha_W T/g_2 v(T)$ at high temperatures. $v(T)$ is the Higgs VEV at finite temperature. ω_- is the negative eigenmode of the saddle-point configuration atop the barrier, while κ is a determinant associated to the quantum and thermal fluctuations about the sphaleron background configuration which drive the process [119, 123–125]. The full derivation of the sphaleron rate and typical values of the above constants in the SM may be recovered in Appendix F.

In view of this short discussion, as well as Eqs. (5.23) and (5.24), one might be led to question the significance of *sphalerons*. After all, nominal sphaleron processes are Boltzmann-suppressed, not so the pure gauge field transitions briefly mentioned above. As will become clear in Chapter 7, however, both behaviours are crucial elements of EWBG.

⁴The calculation invokes a finite-temperature treatment as hinted at in Chapter 3; this is the origin of the $1/T$ -factor in the exponential. A brief and conceptual introduction to rate calculations is provided in Chapter 6, while a derivation of the rate (5.24) can be found in Appendix F.

Chapter 6

Thermal phase transitions

One of the key features of the GWS theory is a phase transition in the EW sector of the SM at EWSB. Although theoretical and phenomenological studies of the EW-PhT in the SM have deemed it inadequate for the purposes of EWBG, experimental verification of its nature remains pending [61–65, 126]. The mechanism of EWBG takes advantage of the knowledge gap and relies on a first-order phase transition with additional properties which may be realized in BSM scenarios. This chapter reviews basic aspects of quantum and thermal phase transitions in preparation for Chapter 7.

6.1 First-order phase transitions

The free energy of a thermal system is essential in defining the nature of a phase transition. For a system with a grand canonical partition function $\mathcal{Z}(T)$, and ignoring any chemical potentials μ , the free energy as a function of temperature T is [95]

$$F(T) \stackrel{\text{def}}{=} -T \log(\mathcal{Z}(T)). \quad (6.1)$$

In a volume V , the corresponding free energy density is given by

$$f(T) \stackrel{\text{def}}{=} \frac{F(T)}{V}. \quad (6.2)$$

The quantities $F(T)$ and $f(T)$ arise naturally in the effective action formalism in relation to $\Gamma[\phi, T]$ and $V_{\text{eff}}(\phi, T)$. Assuming translation-invariant, classical fields in the sense of Chapter 3, and a Euclidean formulation of the theory such that $\Gamma_E[\phi] = (V/T)V_{\text{eff}}(\phi)$ as suggested by Eq. (3.16), the free energy density of a model can be related directly to the ground state energy of its effective potential as [95]

$$f(T) \approx V_{\text{eff}}(\phi_{\min}) + \mathcal{O}\left(\frac{\log V}{V}\right). \quad (6.3)$$

Phase transitions in general emerge as non-analyticities of the grand canonical free energy density $f(T)$ upon changes in the temperature¹. Phase transitions which further exhibit discontinuities in the derivative of the free energy density are called *first-order* phase transitions (FOPhT), as opposed to *second-order* phase transitions (SOPhT). Given relation (6.3) and assuming the analyticity of $V_{\text{eff}}(\phi, T)$, it is straightforward to show that [95]

$$\frac{df(T)}{dT} = \left[\frac{\partial V_{\text{eff}}(\phi, T)}{\partial \phi} \frac{\partial \phi_{\text{min}}}{\partial T} + \frac{\partial V_{\text{eff}}(\phi, T)}{\partial T} \right]_{\phi=\phi_{\text{min}}} = \frac{\partial V_{\text{eff}}(\phi, T)}{\partial T} \Big|_{\phi=\phi_{\text{min}}}. \quad (6.4)$$

The left-hand side term in parentheses after the first equality vanishes when evaluated at the minimum ϕ_{min} . Discontinuities in df/dT therefore arise from discontinuities in the temperature-dependent evolution of the ground state of $V_{\text{eff}}(\phi, T)$, as showcased to the LEFT of Fig. (6.1). In comparison, SOPhTs display a smooth evolution of the ground state, as suggested to its RIGHT. In FOPhTs, the minimum ϕ_{min} thus acts as an *order parameter* of the phase transition: its value will characterize the present phase of the system. In many systems (such as the EW sector of the SM), such a classification is binary and reduces to whether $\phi_{\text{min}} = 0$ or $\phi_{\text{min}} \neq 0$.

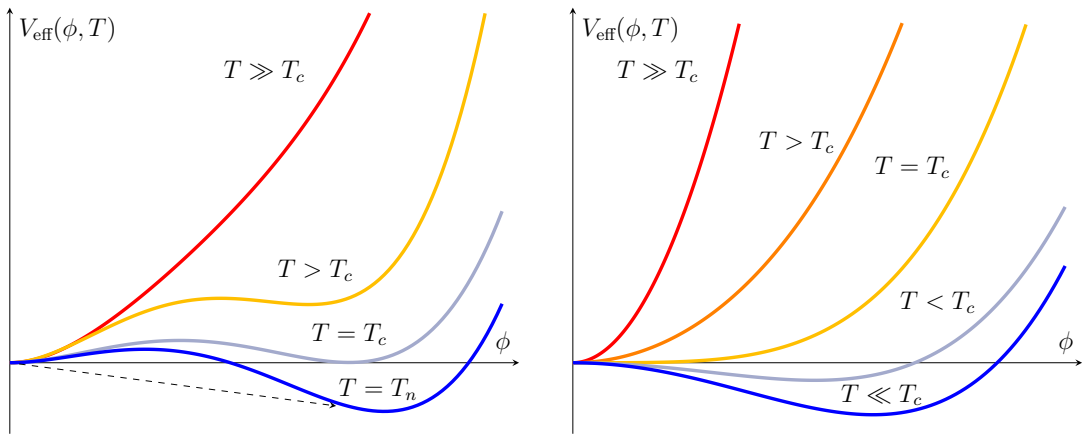


Figure 6.1: LEFT: Evolution of the potential in a FOPhT. The critical temperature T_c is defined by the degeneracy of the minima at $\phi = 0$ and $\phi \neq 0$. The *discontinuous* phase transition takes place at the nucleation temperature $T_n \lesssim T_c$ (see section 6.4). RIGHT: Evolution of the potential in a SOPhT. As the temperature drops, the minimum develops away *continuously*. T_c is defined by the condition $d^2V_{\text{eff}}(\phi)/d\phi^2|_{\phi=0} = 0$. Figures adapted from Refs. [74, 127].

¹And the chemical potential μ , if considered. *Idem* for $df/d\mu$.

FOPhTs are also related to discontinuities in another quantity, the energy density

[95]

$$e(T) \stackrel{\text{def}}{=} f(T) - T \frac{\partial f}{\partial T}. \quad (6.5)$$

As the energy cannot simply vanish, there needs to exist a mechanism able to dissipate the *latent heat* implied by the non-analyticity in e . FOPhTs transfer this energy into the nucleation and growth of bubbles of the new phase. Bubble nucleation is studied within the context of quantum and thermal tunneling through potential barriers, depicted in Fig. [6.2]. The essentials of the formalism will be addressed in the following sections.

6.2 Barrier penetration and quantum tunneling

In quantum mechanics (QM), the ground state energy E_+ of metastable *false vacua* is characterized by an imaginary component that induces a decay rate to a true vacuum [95, 128, 129],

$$\Gamma(E_+) \stackrel{\text{def}}{=} -2 \text{Im}(E_+). \quad (6.6)$$

The Euclidean path integral formulation of QM provides a method for the calculation of such decay rates [130]. The central object is the Euclidean vacuum-to-vacuum transition amplitude [131]

$$\mathcal{Z}_E[0] = \langle \phi_+ | e^{-H\tau} | \phi_+ \rangle = \int \mathcal{D}\Phi e^{-\mathcal{S}_E[\phi]}, \quad (6.7)$$

for some point particle, where ϕ_+ is to be understood as a QM state, H is the Hamiltonian of the system and $\mathcal{S}_E[\phi]$ is the Euclidean action with a potential bounded from below. This amplitude can be related to the energy E_+ by introducing a complete set of eigenstates such that

$$\langle \phi_+ | e^{-H\tau} | \phi_+ \rangle = \sum_{n \in \mathbb{N}} e^{-E_n \tau} \langle \phi_+ | n \rangle \langle n | \phi_+ \rangle. \quad (6.8)$$

For large times τ , the false ground state energy will become the major contributor to the partition function,

$$\lim_{\tau \rightarrow \infty} \langle \phi_+ | e^{-H\tau} | \phi_+ \rangle \sim e^{-E_+ \tau}, \quad (6.9)$$

and hence defines the decay behaviour to leading order [131]:

$$\Gamma = -2 \text{Im}(E_+) = \frac{2}{\tau} \text{Im}(\log \mathcal{Z}_E[0]). \quad (6.10)$$

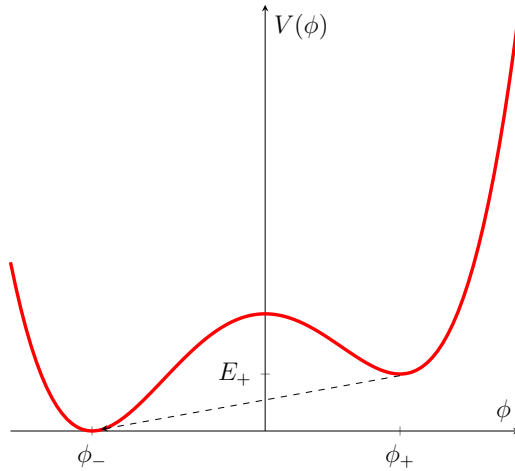


Figure 6.2: Potential with two non-degenerate minima. In a quantum FOPhT, the system tunnels under the barrier at the origin [131].

On the whole, the study of tunneling rates reduces to calculating partition functions of false vacuum transitions. Exact calculations of Eq. (6.10) are notably difficult, and care is required in approximation schemes in order to avoid introducing non-physical artifacts. The semi-classical scheme that underpins calculations relevant to this work is the *saddle-point method* [93]. It restricts the functional integration in Eq. (6.7) only to critical points of the action, *i.e.* points $\hat{\phi}$ such that

$$\left. \frac{\delta \mathcal{S}_E[\phi]}{\delta \phi} \right|_{\phi=\hat{\phi}} = 0, \quad (6.11)$$

and so $\mathcal{Z}_E \sim \exp[-\mathcal{S}_E(\hat{\phi})]$. When such points are saddle-points with suitable properties, the amplitude (6.7) can be shown to be complex valued (see Appendix C), thus inducing a transition rate in the spirit of Eq. (6.10).

The form of Eq. (6.7) might suggest the adoption of this formalism by QFT. Although illustrative, the QM approach cannot entirely capture the field theoretical nuances beyond good order of magnitude estimates. Ultimately, formal subtleties beyond the scope of this short introduction render the rate (6.10) [131]

$$\Gamma \sim \text{Im} (\mathcal{Z}_E[0]), \quad (6.12)$$

amended by a prefactor A that accounts for the effects of quantum fluctuations. Thus, with ϕ upgraded to a scalar field and $\mathcal{Z}_E \sim \exp[-\mathcal{S}_E(\hat{\phi})]$, a working definition for the rate of false vacuum transitions in QFT can be obtained as [132, 133]

$$\Gamma \sim A e^{-\mathcal{S}_E[\hat{\phi}]} [1 + \mathcal{O}(\hbar)]. \quad (6.13)$$

6.2.1 The bounce

In principle, applying Eq. (6.13) requires knowledge of all saddle-points $\hat{\phi}$ for which the action becomes sizeable, which could quickly become intractable. However, semi-classical calculations typically single out one special saddle-point. It is the solution to the classical equation of motion in the inverted potential $-V(\phi)$. In this picture, the prescription (6.7) for paths starting at the false vacuum, climbing uphill and returning to the false vacuum suggests a bouncing motion (LEFT of Fig. 6.3). Consequently, the associated field configuration is deemed the *bounce* (132). It can be shown that, despite the existence of a plethora of saddle-points, the decay rate may generally be related back to the bounce action (134, 135). This is but one of its features. For a scalar field, the generic bounce action in D dimensions reads

$$\mathcal{S}_E^D[\phi] = \int d^D x \left(\frac{1}{2} \partial_\mu \phi \partial^\mu \phi + V(\phi) \right), \quad (6.14)$$

from which the Euler-Lagrange equation of motion can be easily derived. As Euclidean time is assumed, Eq. (6.14) is subject to an $O(D)$ symmetry, which can be exploited by spherical coordinates. Defining a radial coordinate $\rho = (\tau^2 + |\vec{x}|^2)^{1/2}$, the equation of motion can be cast as (27)

$$\frac{d^2 \phi}{d\rho^2} + \frac{D-1}{\rho} \frac{d\phi}{d\rho} = \frac{d}{d\phi} V(\phi) \quad (6.15)$$

with the boundary conditions

$$\lim_{\rho \rightarrow \infty} \phi(\rho) = \phi_+, \quad (6.16)$$

$$\left. \frac{d\phi}{d\rho} \right|_{\rho=0} = 0. \quad (6.17)$$

Bounce solutions ϕ_b to Eq. (6.15) correspond to field configurations interpolating between the false and the absolute vacua. They can be interpreted as the radial profile of the Euclidean bubble and extremize its action S_E . Except for isolated cases, bounce solutions cannot be found exactly and require either strong approximations or numerical methods, most often in combination.

Back in Minkowski spacetime, competition between the volume and surface energies determines the nucleation of Minkowski bubbles (RIGHT of Fig. 6.3). The minimal radius R_M at which these bubbles begin to exist is given precisely by R_E , which further stresses the importance of the bounce solution.

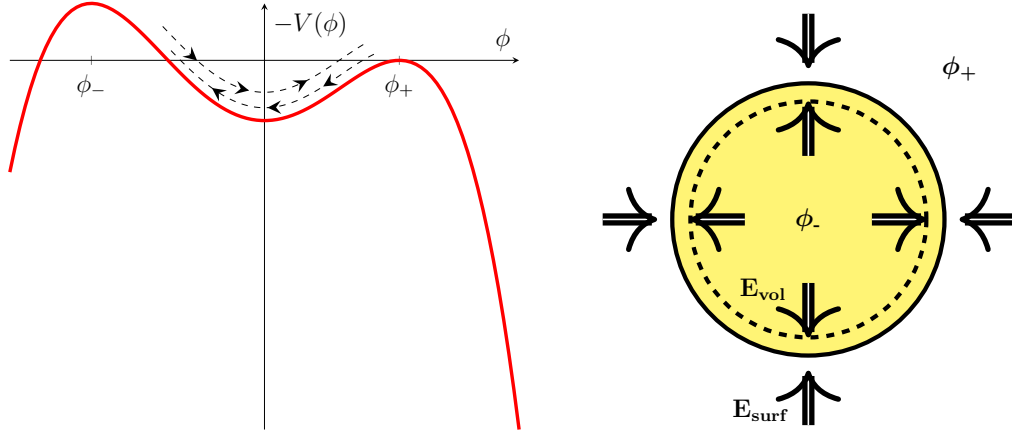


Figure 6.3: LEFT: Inversion $-V(\phi)$ of the the potential in Fig. 6.2. Now in Euclidean spacetime, the field rolls down from ϕ_+ , uphill to ϕ_- and downhill again back to ϕ_+ . Adapted from Ref. 114. RIGHT: In Minkowski spacetime, bubbles nucleate with radius $R_M = R_E$ as soon as the outward pressure generated by the volume energy $\sim V(\phi_-)$ exceeds the inward acting surface tension 114.

6.3 Nucleation in finite-temperature field theory

Extension of nucleation theory to finite temperatures requires some attention to detail. One important update is the replacement of the bare energy E by the free energy F in decay rate considerations, *i.e.* $\Gamma \sim \text{Im}(F)$. Furthermore, symmetry needs to be properly treated. As higher temperatures are considered, the time coordinate τ undergoes compactification as outlined in Chapter 3 and the original $O(D)$ symmetry is lost in favour of $O(D-1)$. The net effect of this change in the formalism is

$$\mathcal{S}_E^D[\phi] \rightarrow \frac{1}{T} \mathcal{S}_E^{D-1}[\phi] \quad (6.18)$$

and the equation of motion becomes

$$\frac{d^2\phi}{d\rho^2} + \frac{D-2}{\rho} \frac{d\phi}{d\rho} = \frac{d}{d\phi} V(\phi). \quad (6.19)$$

Furthermore, in a thermal setting, the dominant fluctuations prompting the transition will be of thermal nature. Thus, the nucleation rate in a thermal theory of four spacetime dimensions behaves as 91, 136–138

$$\Gamma \sim A(T) e^{-S_E^3[\phi]/T} \quad \text{with} \quad A(T) \sim T^4. \quad (6.20)$$

6.4 Electroweak nucleation in a thermal universe

The EWPhT needs to be viewed in the context of an expanding thermal universe. In the chronology of cosmic events, the EWPhT is theorized to happen while the universe is still hot – $T \approx \mathcal{O}(10^2 \text{ GeV})$ – and dominated by radiation. Its energy density is thus [122]

$$\rho(T) = \frac{\pi^2}{30} g_*(T) T^4 \quad (6.21)$$

for $g_*(T)$ relativistic degrees of freedom. It governs an expansion described by the first Friedmann equation [91, 122, 139]

$$\mathcal{H}^2(T) \stackrel{\text{def}}{=} \left(\frac{\dot{a}}{a} \right)^2 = \frac{\rho(T)}{3M_{\text{Pl}}^2} \quad (6.22)$$

with the scale factor $a = a(t(T))$ and the reduced Planck mass $M_{\text{Pl}} = 2.43 \cdot 10^{18} \text{ GeV}$ (see Appendix A). The EW potential evolves as the universe expands and its temperature decreases. The initial scenario typically considered in the SM and beyond is one of restored $SU(2)_L \times U(1)_Y$ symmetry: the temperature-dependent effective potential starts out with a global minimum at $\langle \Phi \rangle = 0$ at high temperatures such that the ground state respect the full EW gauge group. With decreasing temperatures and assuming a FOPhT, the potential develops a local vacuum manifold M for at least one $\langle \Phi \rangle \neq 0$. Degeneracy of this manifold with the minimum at the origin defines a critical temperature T_c , as suggested by LEFT of Fig. 6.1. For temperatures below T_c , one point on M takes over via SSB as the global ground state of EW theory, where the gauge group reduces from $SU(2)_L \times U(1)_Y$ to $U(1)_{\text{em}}$.

The phase transition is potentially viable as early as T_c is reached. In practice, for the transition to complete, at least one bubble needs to nucleate within the cosmic horizon. As indicated in LEFT of Fig. 6.1, this happens at some nucleation temperature $T_n \lesssim T_c$. The requirement that nucleation probability reach unity within the horizon² sets a condition that defines T_n [91, 140, 141], *i.e.*

$$\begin{aligned} \int_{-\infty}^{t_n} dt \Gamma(t) \mathcal{H}^{-3}(t) &\stackrel{(*)}{=} \int_{T_n}^{\infty} \frac{dT}{T} \Gamma(T) \mathcal{H}^{-4}(T) \\ &= \int_{T_n}^{\infty} \frac{dT}{T} \left(\sqrt{\frac{90}{g_*(T)}} \frac{M_{\text{Pl}}}{\pi T} \right)^4 e^{-S_E^3/T} \sim \mathcal{O}(1) \end{aligned} \quad (6.23)$$

²Adiabaticity in the expansion of the universe is assumed, *i.e.* $a(t(T)) \cdot T(t) = \text{const.}$ at (*).

$$\implies \frac{\mathcal{S}_E^3}{T_n} \sim 137 - 4 \log \left(\frac{T_n}{100 \text{ GeV}} \right) \sim \mathcal{O}(100). \quad (6.24)$$

T_n is thus the temperature at which the phase transition sets in, often overlooked on account of its cumbersome evaluation and the rough order-of-magnitude estimate $T_n \approx T_c$. Its computational inconvenience notwithstanding, it is stressed that Eq. (6.24) represents a general constraint in searches for viable transition scenarios: models featuring a critical temperature do not intrinsically get to satisfy the requirement for nucleation, meaning the correct low-temperature EW phase may not be reached.

6.5 The EWPhT in BSM physics

An important feature of many theories beyond the SM resides in additional field-dimensions of the effective potential on account of new, exotic fields. Typically, models with extended scalar sectors – like the ones considered later on in this work – have been shown to possess non-trivial phase transition dynamics [127, 142–150]. Furthermore, and depending on the model assumptions, high-temperature EW symmetry may be complemented by further symmetry requirements, such as an additional \mathbb{Z}_2 symmetry [148]. Therefore, such models can present complex landscapes of phase transition patterns. The transition to the present EW vacuum may thus happen in several steps by virtue of intermediate phases, not all of which feature instances of broken EW symmetry. The class of singlet scalar extensions (Chapter 11) is a paradigmatic example: intermediate transitions *may* be restricted to the new field dimensions, thus preserving the EW gauge group. More generally, these *multi-step* scenarios may present a mixture of first- and second-order transitions. While the latter require separate treatment, the former can be described in terms of the physics outlined in this chapter. At any rate, the crucial element with regards to successful EWBG in such scenarios is at least one instance of a first-order EW-symmetry-breaking step.

Chapter 7

Electroweak baryogenesis

7.1 Outline of the mechanism

EWBG is specifically tailored to match one of the strengths of the SM – its description of EW physics, with particular emphasis on the Higgs sector – while exploiting the knowledge gaps in the present state of the art in order to incorporate all of Sakharov’s conditions for baryogenesis (Chapter [1](#)):

- (i) It features baryon number violation in the form of the sphaleron process introduced in Chapters [4](#) and [5](#).
- (ii) It postulates a first-order EWPhT, as described in Chapter [6](#), that provides the required thermal off-equilibrium conditions.
- (iii) It accounts, at the very least, for the degree of CP violation already present in the SM, although this will be insufficient. Further sources of CP violation can be added in SM extensions.

The fundamental idea behind the mechanism is that, under the off-equilibrium conditions of a FOPhT, asymmetries in C and CP can be reprocessed by the sphaleron process into a baryonic asymmetry.

Before the phase transition

The starting assumption is a primitive universe with no net baryon number. In this early stage, the universe expands at a rate given by the temperature-dependent Hubble constant implied by [\(6.22\)](#), where $g_*(T) \approx 106.75$ are the relativistic degrees of freedom in the SM at $T \sim \mathcal{O}(10^2 \text{ GeV})$ and $M_{\text{Pl}} = 2.43 \cdot 10^{18} \text{ GeV}$ is the reduced Planck mass [\[122\]](#). The universe is permeated by the symmetric EW phase with

$\langle \Phi \rangle = 0$ and therefore sees baryon number violating processes thrive on account of Eq. (5.23). However, thermodynamic equilibrium makes sure no net baryon number arises: any single process generating new baryons will be countered by a process inducing the same number of antibaryons.

Onset of the phase transition

As the temperature of the universe gradually decreases on account of its expansion, the temperature-dependent effective potential develops a local minimum at a non-vanishing value $\langle \Phi \rangle$, and hence a phase where EW symmetry is broken. At some temperature $T_n \lesssim T_c$, the first bubbles of the broken symmetry phase begin to nucleate, as shown in Fig. 7.1. From then on, two phases with drastically different features coexist, separated by the bubble walls: whereas sphalerons remain highly active in the symmetric phase, they become heavily Boltzmann-suppressed within the bubbles (Eq. (5.24)).

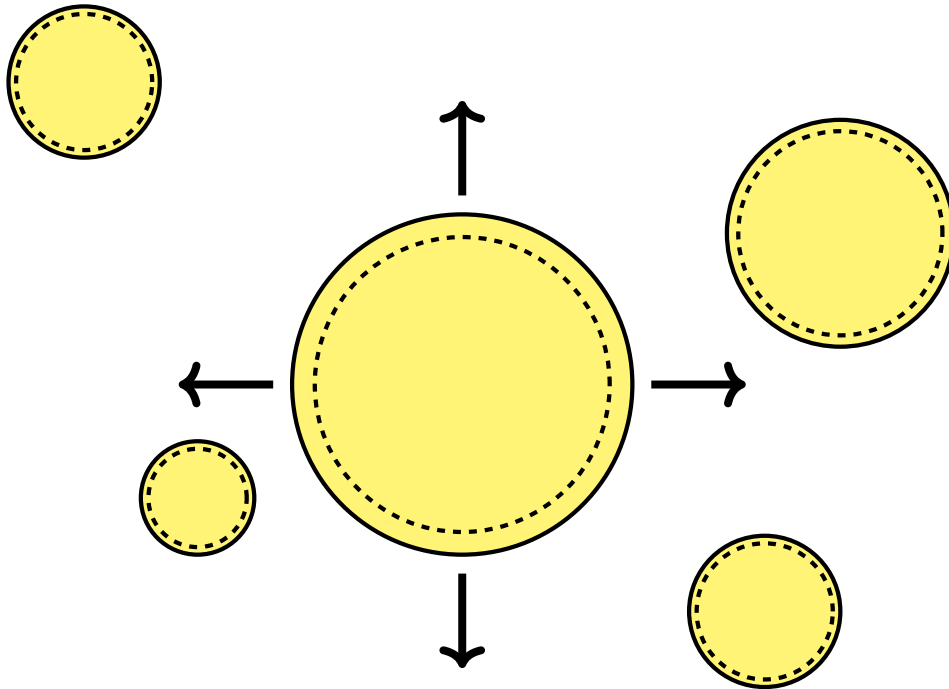


Figure 7.1: When the phase transition sets in, bubbles of the broken phase appear throughout space. The bubble wall is comprised between the continuous and the dashed lines. Adapted from Ref. [30].

Effects of C and CP violation

The structure of weak interactions makes sure that C symmetry is violated maximally in the SM. The Yukawa interactions in the quark sector in turn are endowed with an irreducible complex phase and thus CP violation on account of the CKM matrix (Chapter 2). These ingredients source C and CP violating interactions with the bubble wall, *i.e.* transmission rates into the bubble¹ will differ between particles and antiparticles as well as between (anti-)particles of different chirality [151, 152]. In the scenario showcased by Fig. 7.2, the nature of these interactions with the bubble wall results in a surplus of quarks within the bubble, whereas antiquarks will dominate in the symmetric phase. Overall, a CP asymmetry sets in on both sides of the wall.

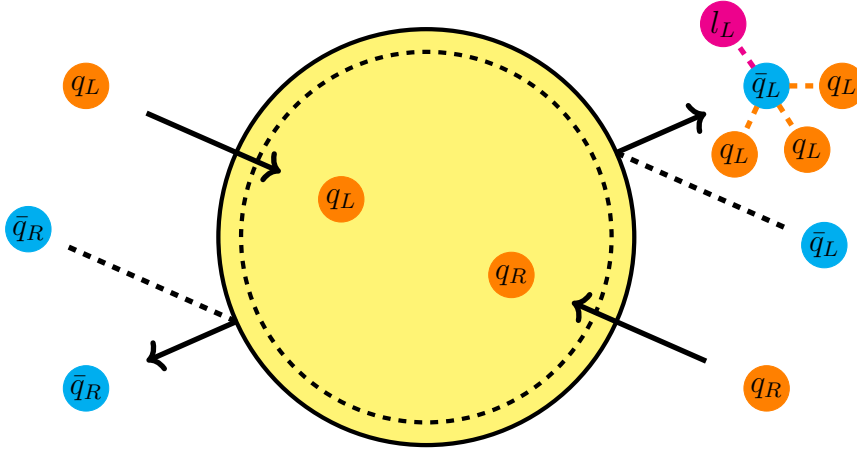


Figure 7.2: C and CP violating interactions with the bubble wall result in different transmission and reflection rates of the quarks. Sphaleron processes couple to q_L and – as in the figure – \bar{q}_L . Overall, a production of baryons over antibaryons is induced in attempts to reestablish a chemical equilibrium between the two in the symmetric phase. This in turn generates an overall net baryon number. The sphaleron process in this figure is simplified such as to produce $\Delta B = \Delta L = 1$ for the sake of clarity. Adapted from Ref. [30].

¹Essentially, a case of quantum mechanical transmission and reflection off a potential barrier. Quantum transport aspects of EWBG are discussed in Ref. [27].

Effects of the non-equilibrium conditions

Ahead of the wall, sphalerons still have free rein to carry out baryon number violating transitions. As before, processes resulting in both positive *and* negative baryonic numbers will take place. However, due to the prevalence of *antibaryons* in the symmetric phase, sphalerons are biased into the production of *baryons* in an attempt to reestablish a local chemical equilibrium. Thus, the CP asymmetry ahead of the bubble is reprocessed into a net positive baryon number (Fig. 7.2). As the bubbles expand and their walls sweep the plasma, these newly formed baryons are transmitted into the phase of broken symmetry, where sphaleron suppression increases as the temperature drops further (Fig. 7.3). The phase transition proceeds to permeate the universe as the bubbles keep on expanding and coalescing.

This stage is critical to EWBG on two accounts. On the one hand, bubble expansion needs to proceed at a rate high enough that the EW broken phase spread throughout the entire universe, yet low enough that baryon number violating processes have time to generate the asymmetry. On the other hand, the baryon number absorbed into the bubbles is only conserved as long as the sphaleron rate in this phase is low enough at the moment of the phase transition. Both assumptions are non-trivial; the former is beyond the scope of this work and treated in some detail in Ref. [27, 75], while the latter constitutes the essence of this work.

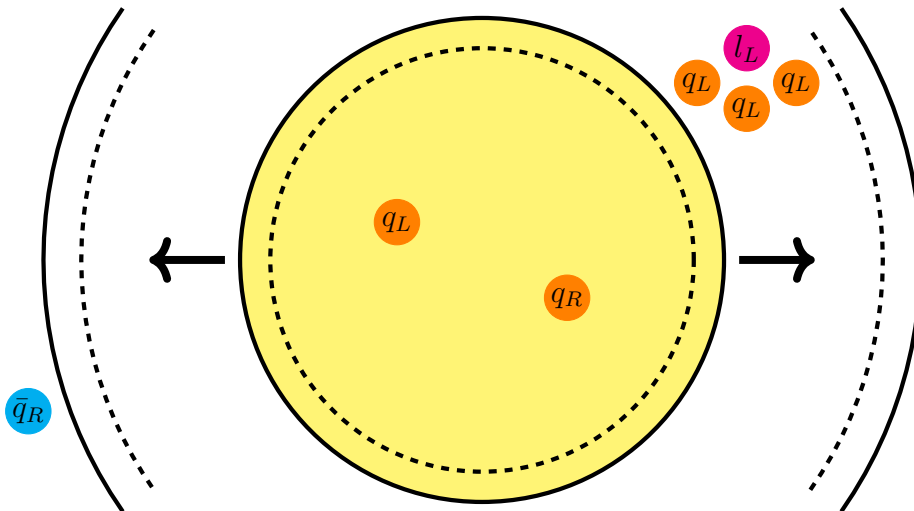


Figure 7.3: The net positive baryon number generated by sphalerons in the symmetric phase is absorbed by the expanding bubble. Adapted from Ref. [30].

7.2 Sphaleron decoupling condition

As suggested by the rate Γ_{sph}^b of sphaleron processes claimed in Chapter 5, sphalerons are subject to a severe Boltzmann suppression in the phase of broken symmetry. With a vanishing sphaleron activity, the baryon number entering the bubbles should thus be preserved. However, it can still succumb to total washout if the suppression is insufficient around the time of bubble nucleation. In a model with c baryonic degrees of freedom², the baryon number density n_B inside the bubbles evolves according to⁵⁶

$$\frac{dn_B(t)}{dt} = -c\Gamma_{\text{sph}}^b n_B(t). \quad (7.1)$$

For the sake of illustration, $\Gamma_{\text{sph}}^b = \Gamma_{\text{sph}}^b(T(t))$ and $T = T(t)$ will first be assumed constant. Then, for a phase transition between the initial and final times t_i and t_f , the fraction of net baryon number density remaining at t_f scales as²⁷

$$\frac{n_B(t_f)}{n_B(t_i)} \sim \exp\left[-c \cdot \text{const.} \cdot \exp(-\mathcal{E}(T)/T)\right] \quad (7.2)$$

on account of $\Gamma_{\text{sph}}^b \sim \exp(-\mathcal{E}(T)/T)$ in Eq. (5.24). The *washout factor* (7.2) is thus extremely sensitive to the sphaleron energy: if too low, sphaleron processes are not suppressed enough and much of the asymmetry will be erased by the end of the phase transition. More formally, Eq. (7.1) implies

$$\frac{n_B(t_f)}{n_B(t_i)} = \exp\left\{-c \int_{t_i}^{t_f} dt \Gamma_{\text{sph}}^b\right\}. \quad (7.3)$$

Washout avoidance is attained if the left-hand side of Eq. (7.3) remains of order one, which implies a similar order of magnitude for the term in parentheses on the right-hand side²⁷. A more formal approach refers back to the Hubble expansion rate (6.22). For $t_f = \infty$, $T_i = T(t_i)$ and $T(t_f) = 0$, and the scale factors $a_i = a(t_i)$ and $a_f = a(t_f)$, Eq. (7.3) can be recast as³¹²²

$$\frac{n_B(t_f)}{n_B(t_i)} = \exp\left\{-c \int_{a_i}^{a_f} \frac{da}{a} \frac{\Gamma_{\text{sph}}^b(a)}{\mathcal{H}(a)}\right\} \quad (7.4)$$

$$= \exp\left\{-c \int_0^{T_i} \frac{dT}{T} \frac{\Gamma_{\text{sph}}^b(T)}{\mathcal{H}(T)}\right\}. \quad (7.5)$$

² $c \approx 13N_F/2$ with N_F the number of generations is thermodynamically motivated^{106, 122}.

³And, again, assuming that $a(t(T)) \cdot T = \text{const.}$ for adiabaticity.

In this form, the requirement that the right-hand side remain of order one roughly translates to [30, 122]

$$\Gamma_{\text{sph}}^b(T_i) < \alpha \mathcal{H}(T_i), \quad (7.6)$$

where $\alpha \sim 0.1$ captures the effects of the integral in Eq. (7.5). Eq. (7.6) is the seminal *baryon washout avoidance criterion* [122]. It can be interpreted as sphalerons decoupling from the remaining processes in the universe and is therefore also known as the *sphaleron decoupling condition* [145]. With the definitions of Γ_{sph}^b in Eq. (5.24) and \mathcal{H} in Eq. (6.22), Eq. (7.6) can be shown to require [122]

$$\begin{aligned} \frac{\mathcal{E}(T_i)}{T_i} &> \log\left(2\mathcal{N}_{\text{tr}}\mathcal{N}_{\text{rot}}\mathcal{V}_{\text{rot}}\frac{\omega_-}{g_2 v(T_i)}\right) + 7\log\left(\frac{4\pi v(T_i)}{g_2 T_i}\right) \\ &\quad - \log\left(\frac{T_i}{M_{\text{Pl}}}\right) - \frac{1}{2}\log\left(\frac{\pi^2 g_*}{90}\right) + 4\log\left(\frac{\alpha_W}{4\pi}\right) + \log\kappa - \log\alpha, \end{aligned} \quad (7.7)$$

with the constants introduced in Chapters 5 and 7.1 and the temperature-dependent Higgs vacuum expectation value $\langle h(T) \rangle = v(T)$. Numerical evaluation⁴ of Eq. (7.7) renders the condition [122]

$$\frac{\mathcal{E}(T_i)}{T_i} > (35.9 - 42.8) + 7\log\frac{v(T_i)}{T_i} - \log\frac{T_i}{100 \text{ GeV}}, \quad (7.8)$$

with an uncertainty sourced by the range $10^{-4} < \kappa < 10^{-1}$ assumed for the sphaleron fluctuation determinant κ . Eq. (7.8) marks the condition for a sufficiently abrupt decoupling of the sphaleron processes. In EWBG, it defines the notion of a *strong* first-order phase transition (SFOPhT). Models not satisfying the criterion do not qualify for EWBG; this renders Eq. (7.8) a decisive criterion. Its evaluation is a central aspect of this work. To this aim, it will be conveniently reexpressed: the quantity [153]

$$\sigma_i \stackrel{\text{def}}{=} \frac{\mathcal{E}(T_i)}{T_i} - 7\log\frac{v(T_i)}{T_i} + \log\frac{T_i}{100 \text{ GeV}} \quad (7.9)$$

will be a measure of the sphaleron decoupling required to satisfy

$$\sigma_i > (35.9 - 42.8) \quad (7.10)$$

in order to mark it as sufficiently abrupt, with the upper (lower) bound corresponding to the upper (lower) bound on κ . In later chapters, (7.10) will be referred to as the σ -*criterion*. As in Eq. (7.2), the importance of $\mathcal{E}(T)/T$ to sphaleron decoupling

⁴The values of the constants can be inferred from Appendix F.

is stressed yet again, given that it dominates the behaviour of σ compared to the remaining logarithmic dependences.

Resting on the SM-inspired *scaling law* of the sphaleron energy with the Higgs VEV given by [154]

$$\mathcal{E}(T) \approx \mathcal{E}_0 \frac{v(T)}{v_0}, \quad (7.11)$$

the condition for sufficient sphaleron decoupling can be recast as [122]

$$\frac{v(T_i)}{T_i} > \left((0.973 - 1.16) + 0.190 \log \frac{v(T_i)}{T_i} - 0.027 \log \frac{T_i}{100 \text{ GeV}} \right) \cdot \left(\frac{1.91 \cdot 4\pi v_0 / g_2}{\mathcal{E}_0} \right), \quad (7.12)$$

i.e. as a condition on the order parameter of the phase transition

$$\xi_i \stackrel{\text{def}}{=} \frac{v(T_i)}{T_i}. \quad (7.13)$$

It is typically simplified to the order-of-magnitude estimate [75]

$$\xi_i \gtrsim 1 \quad (7.14)$$

on account of the magnitude of the right-hand side terms⁵ in Eq. (7.12). Some references suggest the range [91]

$$\xi_i \gtrsim (1.0 - 1.3) \quad (7.15)$$

as the onset for SFOPhTs, where the upper (lower) bound is induced by the upper (lower) bound on κ . Condition (7.14), henceforth the ξ -*criterion*, has come to prevail in the literature in view of its numerical convenience; instead, the σ -criterion has for the most part been relegated to selected papers for specialists (*e.g.* Refs. [122, 145, 153, 155, 156]). Another front on which evaluation of the phase transition strength has historically been simplified is the onset of the phase transition t_i and the corresponding temperature T_i , at which Eqs. (7.8) and (7.14) need to be evaluated. Since T_c is easier to handle numerically than T_n , it has been far more widely employed, to the point where most reviews of EWBG, such as Refs. [27, 75], largely omit any mention of T_n . While this omission may be well justified when $T_n \approx T_c$, a physically strict treatment requires the evaluation at T_n . Finally⁶, Ref. [157] reports problems of gauge dependence in standard treatments of quantities like T_i and – especially – v_i , which in turn implicate both σ_i and ξ_i .

⁵As noted in Chapter 6, $T_i \sim \mathcal{O}(10^2)$ GeV is assumed.

⁶Although crucial, this issue is beyond the scope of the present work.

7.3 Status of electroweak baryogenesis

The success of EWBG banks as much on the viability of each subprocess outlined in section [7.1](#) as on their overall harmonization. In the *status quo* of the SM, the theory is quick to run into problems. First of all, and as pointed out in the introduction, it has been noted that the amount of CP violation provided by known sources (most notably the CKM matrix) is largely insufficient to explain the observed baryon asymmetry [\[57–60\]](#). Secondly, as discussed in section [7.2](#), EWBG only works in case of a SFOPhT. However, the decoupling condition is known to place a modest upper limit on the Higgs quartic coupling and thus on the Higgs boson mass in SM perturbative and lattice calculations alike [\[61–65, 126\]](#). As of the boson’s discovery, vanilla EWBG in the SM has become a dead end [\[158\]](#).

Despite these drawbacks, EWBG still remains an attractive explanation to the BAU. Interest persists as the shortcomings of the SM become more and more glaring. As it stands, the SM fails to deliver on certain areas besides the BAU [\[1–5, 7–10\]](#). Some of these issues, such as the hierarchy problem and even DM⁷, closely tie in with the EW sector [\[11–13, 159\]](#). As the scientific community persists in its efforts to tackle these issues, the question arises of whether some exotic model is able to provide a comprehensive solution. Revisiting EWBG thus becomes mandatory. One of the many aspects which merit review in BSM scenarios is condition [\(7.14\)](#) for a SFOPhT, which – despite an uneven assessment across a range of different models – prevails as a “golden rule” in studies of EWBG. The present work aims to shed some light on the reliability of condition [\(7.14\)](#), derived under SM assumptions on the scaling law [\(7.11\)](#) and the order of magnitude of the sphaleron-related constants in Eq. [\(7.7\)](#), in two BSM scenarios featuring extended scalar sectors.

⁷Obviously, its relevance to EW physics depends on the specifics of the DM candidate.

Part II

Methods

Chapter 8

Constructing the effective potential

The one-loop, thermal effective potential, briefly hinted at in Chapter 3, constitutes an integral aspect of the analyses and results presented in Part III of this work. The essence of its character is largely determined by model-specific features, which are therefore treated in detail throughout Chapters 10 and 11. The present chapter aims to showcase the general principles, structures and implementations applied throughout Part III.

8.1 Coleman-Weinberg potential

The Coleman-Weinberg (CW) potential used in this work is obtained in Landau gauge from dimensional regularization in the modified minimal subtraction ($\overline{\text{MS}}$) on-shell renormalization scheme at a scale $\mu = v \approx 246.22 \text{ GeV}$. It reads [91, 160]

$$V_{\text{CW}}(\phi) \stackrel{\text{def}}{=} \frac{1}{64\pi^2} \sum_i (-1)^{2s_i} n_i m_i^4(\phi) \left\{ \ln \left(\frac{m_i^2(\phi)}{\mu^2} \right) - C_i \right\}. \quad (8.1)$$

The sum runs over all the particles i appearing in the model. Their spins s_i , degrees of freedom n_i and renormalization constants C_i are specific to each species and are indicated respectively in Table 8.1. The masses m_i are mostly model-dependent and will be addressed in Chapters 10 and 11.

By using Eq. (8.1), one tacitly drops the infinities inherent to loop calculations, as they are removed by the renormalization scheme. Nonetheless, it will be necessary to introduce a finite counterterm potential V_{CT} to fully settle the renormalization [91]. The coefficients of the counterterm potential can be fixed through specific renormalization conditions. In general, they will be chosen such as to keep the tree-level minima and masses intact. Further details can be inferred from the respective model-building sections in Chapters 10 and 11.

Table 8.1: Specifications for the spins s_i , the degrees of freedom n_i and renormalizations constants C_i appearing in the CW and one-loop thermal potentials of the models featured in this work. Fields marked with the subscript \mathcal{L} correspond to longitudinal components; those with \mathcal{T} , to transverse ones. Values adapted from Refs. [149, 156].

Species	s_i	n_i	C_i
Quarks	1/2	12	3/2
Charged leptons	1/2	4	3/2
Neutral scalars	0	1	3/2
Charged scalars	0	2	3/2
Goldstones	0	1×3	3/2
$W_{\mathcal{L}}^{\pm}$	1	2	3/2
$W_{\mathcal{T}}^{\pm}$	1	4	1/2
$Z_{\mathcal{L}}$	1	1	3/2
$Z_{\mathcal{T}}$	1	2	1/2
$\gamma_{\mathcal{T}}$	1	2	0
$\gamma_{\mathcal{L}}$	1	1	0

8.2 Thermal one-loop corrections

In order to track phase transitions, Chapter 3 suggested to account for thermal effects. The dominant contributions are provided by the thermal one-loop corrections

$$V_1^{\text{th}}(\phi; T) \stackrel{\text{def}}{=} \frac{T^4}{(2\pi)^2} \sum_i n_i J_{B,F} \left(\frac{m_i^2(\phi)}{T^2} \right), \quad (8.2)$$

with a sum over i sweeping the particle content, where

$$J_{B,F}(x) \stackrel{\text{def}}{=} \pm \int_0^{\infty} dz z^2 \ln(1 \mp e^{-\sqrt{z^2+x}}) \quad (8.3)$$

are the thermal functions for bosons and fermions, respectively [97]. Various approximation schemes can handle the numerically cumbersome integrals. In the high-temperature range defined as $|x| \ll 1$ for $x \stackrel{\text{def}}{=} m^2/T^2$, the expansions [161]

$$J_B(x) \approx -\frac{\pi^4}{45} + \frac{\pi^2}{12}x - \frac{\pi}{6}x^{\frac{3}{2}} - \frac{1}{32}x^2 \ln \left(\frac{x}{a_b} \right) \quad (8.4)$$

$$J_F(x) \approx -\frac{7\pi^4}{360} + \frac{\pi^2}{24}x + \frac{1}{32}x^2 \ln \left(\frac{x}{a_f} \right) \quad (8.5)$$

with $a_b = 16\pi^2 \exp(3/2 - 2\gamma_E)$ and $a_f = \pi^2 \exp(3/2 - 2\gamma_E)$ are justified and widely employed in the literature. Another approach, developed in Ref. [162], consists in an expansion of the J -functions in terms of Bessel functions of the second kind,

$$J_{B,F}(x) = \lim_{N \rightarrow \infty} \mp \sum_{r=1}^N \frac{(\pm 1)^r}{r^2} K_2(r\sqrt{x}). \quad (8.6)$$

This approach has been shown to provide a highly reliable approximation over a wide range of temperatures for as low as $N = 5$ [160]. For the present work, this was the chosen implementation.

8.3 Thermal resummation

Thermal dependence in FTFT prompts a competition between the temperature and the mass scales which needs to be tracked. A careful revision of the leading-order diagrams will reveal the breakdown of the one-loop perturbative expansion at high temperatures and the need for a scheme that fixes this conduct. A standard, real ϕ^4 -theory [163] with a mass parameter $\mu^2 > 0$ and self-coupling λ will serve to showcase this rather general issue (cf. Refs. [91, 95, 161]). Its self-energy diagrams induce temperature-dependent corrections to the mass parameter term of the potential [163],

$$-\mu^2 \rightarrow -\mu_{\text{eff}}^2 = -\mu^2 + \Pi(T). \quad (8.7)$$

The exact temperature dependence of $\Pi(T)$ is determined by the superficial degree of divergence \mathcal{D} of the diagram [2]. $\Pi(T)$ will scale at least linearly with T on account of the prescription for loop integrals in FTFT (Appendix B, Eq. (B.5)). However, with $\mathcal{D} > 0$ and in absence of infrared (IR) divergences in loops associated to bosonic propagators, $\Pi(T)$ will scale as $\lambda T^{\mathcal{D}}$ for the generic, so-called ‘‘hard thermal loop’’ [161]. The crucial quantities to assessing the validity of the perturbative expansion are λ and

$$\alpha \stackrel{\text{def}}{=} \frac{\lambda T^2}{\mu^2}. \quad (8.8)$$

As long as $\alpha, \lambda \ll 1$, the expansion is well-behaved. However, in high-temperature scenarios, the occurrence of symmetry restoration brought about by a vanishing of μ_{eff}^2 suggests that hard loops will typically reach the scale of μ^2 and thus $\alpha \sim 1$. At this stage, neglecting higher-order loop diagrams like those in Fig. 8.1 becomes untenable, as they will constitute leading contributions to the effective potential.

¹*i.e.* the tree-level potential $V_{\text{tree}}(\phi) = -\frac{1}{2}\mu^2\phi^2 + \frac{1}{4}\lambda\phi^4$ is assumed.

² $\mathcal{D} = D \cdot \#\text{loops} - 2 \cdot \#G_B - \#G_F$, where D is the number of space-time dimensions and $\#\text{loops}$ and $\#G_{B,F}$ are the number of loops and gauge boson/fermion propagators in the diagram [79].



Figure 8.1: On the left, the hard thermal loop goes like λT^2 to leading order. On the right, n loops were added on top of it. Close to symmetry restoration one has $\alpha \sim 1$, which means such *daisy* diagrams are not just unsuppressed but might constitute leading contributions to the self-energy. Adapted from Refs. [91, 127].

Different prescriptions exist in order to deal with such thermal misbehaviour of the theory. The widely used (*truncated*)³ *full dressing* scheme proposes the generic replacement

$$m_i^2(\phi) \rightarrow m_i^2(\phi) + \Pi_i(T) \quad (8.9)$$

for all field-dependent masses entering the effective potential via Eqs. (8.1) and (8.2) [164, 165]. This standard procedure amounts to a resummation of all modes in Eq. (B.5) and comes at the cost of irregularly blending the ultraviolet (UV) and IR dynamics of the system [166]. In order to avoid such inconsistencies, Ref. [167] instead suggests restricting the thermal treatment to the bosonic *zero modes* in loops, *i.e.* the massless modes corresponding to $n = 0$ in Eq. (B.5). This approach comes with its own problems, as its consistency relies on the steady assumption that $m_i^2/T^2 \ll 1$, which may not hold throughout parameter scans of a model [161].

8.4 Thermal Debye masses

Self-energy corrections are specific to each model as they depend on the available couplings. For this reason, all of the thermal Debye masses will be indicated in Chapters [10] and [11]. Some general statements are in order, however. For a scalar ϕ sourcing a thermal potential (8.2), the corrections can be captured by [141, 161]

$$\Pi_\phi(T) \approx \frac{d^2 V_1^{\text{th}}(\phi; T)}{d\phi^2} \quad (8.10)$$

³Truncated because the cumbersome integral expressions for $\Pi_i(T)$ are usually replaced by leading order approximations, as detailed in the next section [96, 161].

with V_1^{th} evaluated at the zero-temperature masses. To leading order in x in the expansions (8.4) and (8.5), the corrections become field-independent. Fermions and gauge bosons also acquire thermal mass corrections. As the former are largely negligible for the present work, only the corrections to the boson masses will be accounted for. It is worth pointing out that the transverse modes do not obtain such corrections, being shielded by custodial symmetry [168].

8.5 Full thermal effective potential

In summary, there exist two *a priori* inequivalent implementations of the effective potential. For the case of one field dimension, the standard truncated full dressing procedure yields [161]

$$V_{\text{eff}}(\phi; T) = V_{\text{tree}}(\phi) + V_{\text{CW}}(\phi) + V_{\text{CT}}(\phi) + V_1^{\text{th}}(\phi; T) \quad (8.11)$$

with the replacement $m_i^2(\phi) \rightarrow \tilde{m}_i^2(\phi) = m_i^2(\phi) + \Pi_i(T)$ everywhere. The alternative treatment keeps the zero temperature masses throughout V_{CW} and V_1^{th} and delivers

$$V_{\text{eff}}(\phi; T) = V_{\text{tree}}(\phi) + V_{\text{CW}}(\phi) + V_{\text{CT}}(\phi) + V_1^{\text{th}}(\phi; T) + V_{\text{daisy}}(\phi; T), \quad (8.12)$$

where

$$V_{\text{daisy}}(\phi; T) \stackrel{\text{def}}{=} -\frac{T}{12\pi} \sum_i n_i \left[(\tilde{m}_i^2(\phi, T))^{\frac{3}{2}} - (m_i^2(\phi))^{\frac{3}{2}} \right] \quad (8.13)$$

takes care of the daisy resummation [161].

Chapter 9

Numerical methods

Model implementation in line with Chapter 8 is followed by essentially threefold numerical efforts. First, suitable model parameters need to be found. The theoretical and experimental screening criteria are model-dependent and thus treated in Chapters 10 and 11. Successful parameter sets are then passed onto `CosmoTransitions`, which returns information on the viability and the character of phase transitions in the model. This output is finally fed into a relaxation algorithm which allows to solve the sphaleron equations – and thus to calculate its energy – both at zero and finite temperature. A brief description of the numerical methods is provided hereinafter.

9.1 CosmoTransitions

Finding solutions to the bounce equation (6.19) is a challenging task: whereas quasi-analytical methods like the overshoot/undershoot method may find a satisfactory numerical implementation in one field dimension (see *e.g.* Refs. [169, 170]), the scope of the problem increases dramatically with the number of fields. The package `CosmoTransitions` makes use of a *path deformation method* which by contrast remains stable in higher field dimensions [171]. It takes advantage of the fact that, in N field dimensions, Eq. (6.19) can be decomposed into a parallel and a perpendicular component along the bounce path between the vacua in field space. More precisely: in N field dimensions, one has $\phi(y) = (\phi_1(y), \dots, \phi_N(y))$ for some parametrization $y = y(\rho)$. Then, the bounce equation (6.15) can be reexpressed as

$$\frac{d^2 y}{d\rho^2} + \frac{\epsilon}{\rho} \frac{dy}{d\rho} = \frac{\partial}{\partial y} V(\phi(y)) \quad (9.1)$$

$$\frac{d^2 \phi(y)}{dy^2} \left(\frac{dy}{d\rho} \right)^2 = \nabla_{\perp} V(\phi(y)) \quad (9.2)$$

with $\epsilon = D - 1$ or $\epsilon = D - 2$ depending on the thermal scenario. The algorithm initializes a straight bounce path and solves the one-dimensional (9.1) via shooting. It then checks whether the solution satisfies Eq. (9.2). If not, it iteratively deforms the path and reevaluates the equations until a solution to both is obtained. In this manner, `CosmoTransitions` is able to provide the bounce action as well as the nucleation temperature T_n and vacuum expectation values $\langle \phi(y) \rangle_n = (v_{1,n}, \dots, v_{N,n})$. The corresponding and more trivially accessible critical quantities T_c and $\langle \phi(y) \rangle_c = (v_{1,c}, \dots, v_{N,c})$ are provided as well.

The analysis carried out with the package for the present work relies on two implementations of the code accessible at [172] (for the analysis in Ref. [148]) and [173] (implemented for Ref. [174]).

9.2 Relaxation algorithm

The system of equations (5.21) of the sphaleron falls under the category of so-called boundary value problems, for which a wide variety of solvers exist in conventional computational software. They usually correspond to implementations of two classes of methods: “shooting” and collocation [170]. However, these standard solvers quickly reach their limits when confronted to the sphaleron equations. Most solutions are plagued by divergences towards vanishing radii; and, as one attempts to increase the domain of interest, these methods quickly meet their doom. Depending on the solver, implementing different types of boundary conditions can be a challenge in itself. It is therefore crucial to develop a method that takes care of the boundary conditions and of potentially large domains of interest. At the same time, the chosen method needs to remain stable as the number of fields increases. The relaxation method was found to meet all of these needs, and the study of sphalerons has in fact seen successful implementations thereof in the past (see *e.g.* Refs. [145, 155, 156]). In the following, the implementation suggested by Ref. [169] and used for this work is presented.

Higher order ordinary differential equations and coupled systems thereof can typically be recast as systems of N first-order differential equations

$$\frac{d\mathbf{y}}{dx} = g[x, \mathbf{y}], \quad (9.3)$$

where $\mathbf{y} = \mathbf{y}(x)$ is the N -dimensional state vector of the system evaluated at the point x . Computational methods generally profit from this feature, and finite-difference methods like the relaxation algorithm take Eq. (9.3) as a starting point. These methods then proceed by discretizing the domain of the independent variable x into a finite mesh of M points x_k . In general, there is no unique discretization prescription [169]. However, a typical approach calculates the derivative of \mathbf{y} on the interval $(x_{k-1}, x_k]$ as

$$\frac{d\mathbf{y}_k}{dx} \approx \frac{\mathbf{y}_k - \mathbf{y}_{k-1}}{x_k - x_{k-1}}, \quad (9.4)$$

with $\mathbf{y}_q \stackrel{\text{def}}{=} \mathbf{y}(x_q)$; the right-hand side of Eq. (9.3) is in turn evaluated at the midpoint of the interval. At every interior point x_k , Eq. (9.3) is thus ideally rendered

$$\mathbf{y}_k - \mathbf{y}_{k-1} - (x_k - x_{k-1}) g \left[\frac{1}{2}(x_k + x_{k-1}), \frac{1}{2}(\mathbf{y}_k + \mathbf{y}_{k-1}) \right] = \mathbf{0}_N. \quad (9.5)$$

The finite difference (9.5) relates two adjacent mesh points and two state vectors in a system of N algebraic equations at every interior x_k . Solutions to Eq. (9.3) are found as sets of \mathbf{y}_k that optimally satisfy Eq. (9.5) all over the mesh.

The method is initialized with an educated guess of the solution, which is translated into a set of initial \mathbf{y}_k throughout the mesh. This choice will in general not satisfy the equality in Eq. (9.5) and lead to the N -dimensional deviation

$$\mathbf{D}_k(\mathbf{y}_k, \mathbf{y}_{k-1}) = \mathbf{y}_k - \mathbf{y}_{k-1} - (x_k - x_{k-1}) g \left[\frac{1}{2}(x_k + x_{k-1}), \frac{1}{2}(\mathbf{y}_k + \mathbf{y}_{k-1}) \right] \quad (9.6)$$

for each interior x_k . The boundary equations at $k = 1$ and $k = M$ instead have a special form: they are manually set to fix the boundary conditions. To this aim, the n_1 -dimensional \mathbf{D}_1 at the boundary x_1 is made to meet

$$\mathbf{D}_1(\mathbf{y}_1) = \mathbf{B}(x_1, \mathbf{y}_1) = \mathbf{0}_{n_1} \quad (9.7)$$

for some algebraic relation \mathbf{B} involving x_1 and \mathbf{y}_1 . Similarly, at x_M and with $n_2 = N - n_1$, the n_2 -dimensional \mathbf{D}_M is set such that

$$\mathbf{D}_M(\mathbf{y}_M) = \mathbf{C}(x_M, \mathbf{y}_M) = \mathbf{0}_{n_2}. \quad (9.8)$$

For M meshpoints and a system (9.3) of N equations, the full vectors

$$\tilde{\mathbf{y}} \stackrel{\text{def}}{=} \begin{pmatrix} \mathbf{y}_1 \\ \mathbf{y}_2 \\ \vdots \\ \mathbf{y}_M \end{pmatrix} \quad \text{and} \quad \mathbf{D}(\tilde{\mathbf{y}}) \stackrel{\text{def}}{=} \begin{pmatrix} \mathbf{D}_1(\mathbf{y}_1) \\ \mathbf{D}_2(\mathbf{y}_1, \mathbf{y}_2) \\ \vdots \\ \mathbf{D}_M(\mathbf{y}_M) \end{pmatrix} \quad (9.9)$$

are $(M \cdot N)$ -dimensional. The system is solved when a $\tilde{\mathbf{y}}$ is found such that $\mathbf{D}(\tilde{\mathbf{y}}) = \mathbf{0}_{M \cdot N}$. Educated initializations of $\tilde{\mathbf{y}}$ will minimize the components of \mathbf{D} from the start. However, a scheme is needed which provides information on how to vary each component of $\tilde{\mathbf{y}}$ in order to better render the solution. One such scheme is provided by the multivariate Newton-Raphson method for root-finding, which iteratively improves $\tilde{\mathbf{y}}$ until $\mathbf{D}(\tilde{\mathbf{y}}) = \mathbf{0}_{M \cdot N}$ within a chosen degree of tolerance.

Newton's method assumes a linear perturbation of the system, *i.e.* $\tilde{\mathbf{y}} \rightarrow \tilde{\mathbf{y}} + \Delta\tilde{\mathbf{y}}$. Under this perturbation, finding a solution to the system of equations (9.3) means finding $\Delta\tilde{\mathbf{y}}$ such that

$$\mathbf{D}(\tilde{\mathbf{y}} + \Delta\tilde{\mathbf{y}}) = \mathbf{0}_{M \cdot N}. \quad (9.10)$$

The left-hand side can be expanded to first order in the perturbation as

$$\mathbf{D}(\tilde{\mathbf{y}} + \Delta\tilde{\mathbf{y}}) \approx \mathbf{D}(\tilde{\mathbf{y}}) + \mathbf{S} \cdot \Delta\tilde{\mathbf{y}}, \quad (9.11)$$

where \mathbf{S} is a $(MN \times MN)$ -dimensional Jacobian matrix which encodes in its structure the coupling between adjacent state vectors (Appendix G). Under this expansion, the original system of differential equations is finally reduced to an algebraic linear system of equations for $\Delta\tilde{\mathbf{y}}$,

$$\mathbf{S} \cdot \Delta\tilde{\mathbf{y}} = -\mathbf{D}(\tilde{\mathbf{y}}). \quad (9.12)$$

Solving Eq. (9.12) is a straightforward task for conventional computational software. Upon obtaining $\Delta\tilde{\mathbf{y}}^{(i)}$ for some iteration (i) , the perturbation is added to the original state vector in order to seed the next iteration, *i.e.*

$$\tilde{\mathbf{y}}^{(i+1)} = \tilde{\mathbf{y}}^{(i)} + \Delta\tilde{\mathbf{y}}^{(i)}. \quad (9.13)$$

Starting from Eq. (9.5), the entire process is reiterated until, ideally, $\mathbf{D}^{(i')}(\tilde{\mathbf{y}}^{(i')}) = 0$ for some iteration (i') . In practice, a convergence criterion has to be introduced, such as

$$\frac{1}{M \cdot N} \sum_{j=1}^{M \cdot N} |D_j^{(i)}| < c \quad \text{or} \quad \frac{1}{M \cdot N} \sum_{j=1}^{M \cdot N} |\Delta y_j^{(i)}| < c \quad (9.14)$$

for some convergence parameter c . The corresponding $\tilde{\mathbf{y}}^{(i')}$ provides the solution to Eq. (9.3) on the mesh.

The code developed for this work builds on the preexisting Mathematica implementation of Ref. [175], in turn inspired by a Matlab version developed for the

work in Ref. [176]. One aspect of the code which shall not remain uncommented is the imposition of boundary conditions on the interval $[0, \infty]$. It is possible to compactify the solution domain by an appropriate reparametrization of the independent variable; thus, the boundary conditions on Eqs. (5.21) at infinity can be restated in computationally accessible terms. However, under such typically non-linear reparametrizations, the uniformity of the mesh is lost. This becomes problematic upon interpolation and integration of the mesh solutions, as linear interpolations can become too rough and higher order interpolations are found to introduce unphysical artifacts. The issue may be averted by choosing a high enough mesh density – at the cost of drastical increases in the computational complexity, with \mathcal{S} scaling as $\mathcal{O}(M^2)$. As a compromise solution, all sphaleron equations in this work are solved on finite, uniformly discretized domains. The appropriateness of this approach relies on a fast convergence of the solutions; in the case of Eqs. (5.21), this is well supported by Fig. 5.3. An overall sanity check was carried out by calculating the sphaleron energy in the tree-level SM at different values of λ/g_2^2 and comparing the results to benchmarks in Ref. [55]. As Fig. 9.1 shows, results slightly depend on the length ξ_{\max} of the solution domain as well as on the mesh density. Maximal discrepancies of $\sim 6\%$ are noted for values of λ/g_2^2 at which the relaxation method is particularly ill-behaved on account of numerical effects.

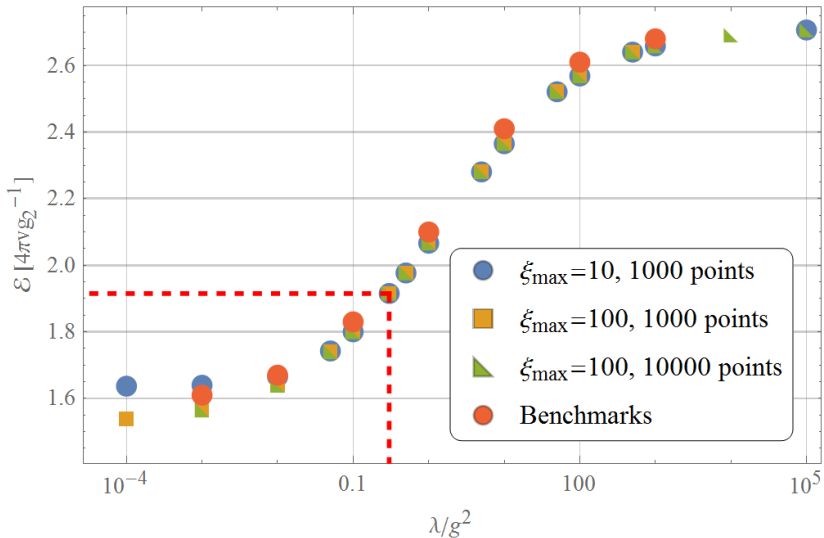


Figure 9.1: Sphaleron energies in the tree-level SM for different values of λ/g_2^2 . The red markers represent the benchmark points of Ref. [55]. The red lines mark the energy at $\lambda/g_2^2 \approx 0.3$, approximately the tree-level SM value [122]. Missing points did not converge.

Part III

Criterion for a strong first-order electroweak phase transition in BSM scenarios

Chapter 10

Inert Doublet Model

An important class of natural BSM scenarios is provided by multi-doublet extensions of the Higgs sector. The simplest such scenario is the inert doublet model, which consists of just one additional exotic $SU(2)_L$ doublet both decoupled from the fermions and presenting a vanishing VEV at zero temperature [174]. Just like the two-Higgs doublet model (2HDM) – its more general counterpart –, the IDM possesses a number of features which render it an attractive model to study. Part of the allure lies in the additional scalars and pseudoscalars it supplies, which have been touted as dark matter (DM) candidates. Furthermore, the inertness of the second doublet largely enforces standard EW physics at zero temperature, thus reconciling known phenomenology with the landscape of possibilities arising at high energies. As pertains to this work, the model crucially presents non-trivial phase transition dynamics and thus a wide playground for EWBG. As recent studies have shown, the realization of both a correct DM relic abundance and a strong first-order EWPhT is highly constrained but still feasible within selected regions of parameter space [127, 149, 174, 177–181]. It thus becomes imperative that the condition for a SFOPhT be revisited as a means of refining the search for viable sets of model parameters.

10.1 The model

This chapter contemplates the EW Lagrangian

$$\mathcal{L}_{\text{EW}}^{\text{IDM}} \stackrel{\text{def}}{=} \mathcal{L}_{\text{kin}}^{\text{SM}} \Big|_{\Phi=\Phi_1} + \mathcal{L}_{\text{Yuk}}^{\text{SM}} \Big|_{\Phi=\Phi_1} + (\mathcal{D}_\mu \Phi_2)^\dagger (\mathcal{D}^\mu \Phi_2) - V_{\text{eff}}(\Phi_1, \Phi_2). \quad (10.1)$$

The structure of (10.1) is fundamentally SM-like: $\mathcal{L}_{\text{kin}}^{\text{SM}}$ and $\mathcal{L}_{\text{Yuk}}^{\text{SM}}$ are the SM kinetic and Yukawa terms seized from Chapter 2, each featuring the SM-like Higgs doublet

Φ_1 . Additionally, the IDM counts a second $SU(2)_L$ doublet Φ_2 . In both standard notation (cf. Refs. [149, 160]) and unitary gauge, the doublets are expressed as

$$\Phi_1 = \begin{pmatrix} \phi^+ \\ (h + i\phi)/\sqrt{2} \end{pmatrix}, \quad \Phi_2 = \begin{pmatrix} H^+ \\ (H + iA)/\sqrt{2} \end{pmatrix}, \quad (10.2)$$

with the standard Higgs boson h , the new scalars H , H^\pm , the Goldstone bosons ϕ , ϕ^\pm and the pseudo-scalar A . The proposed tree-level potential consists of two SM-inspired sectors to which interaction terms between the Higgs doublets are added [149],

$$V_{\text{tree}}(\Phi_1, \Phi_2) = \mu_1^2 |\Phi_1|^2 + \mu_2^2 |\Phi_2|^2 + \lambda_1 |\Phi_1|^4 + \lambda_2 |\Phi_2|^4 \\ + \lambda_3 |\Phi_1|^2 |\Phi_2|^2 + \lambda_4 |\Phi_1^\dagger \Phi_2|^2 + \frac{\lambda_5}{2} \left[(\Phi_1^\dagger \Phi_2)^2 + \text{h.c.} \right]. \quad (10.3)$$

Both h and H are treated as dynamic degrees of freedom which eventually attain their VEVs $\langle h \rangle = v_1 = v_{\text{EW}}^{\text{SM}}$ and $\langle H \rangle = v_2 = 0$. All other fields are assumed to vanish when evaluated at the vacuum. Correspondingly, the tree-level potential in terms of its degrees of freedom boils down to

$$V_{\text{eff}}(h, H) = \frac{\mu_1^2}{2} h^2 + \frac{\mu_2^2}{2} H^2 + \frac{\lambda_1}{4} h^4 + \frac{\lambda_2}{4} H^4 \\ + \frac{\lambda_3}{4} h^2 H^2 + \frac{\lambda_4}{4} (hH)^2 + \frac{\lambda_5}{2} \left[\frac{1}{4} (hH)^2 + \text{h.c.} \right]. \quad (10.4)$$

Unlike general 2HDM scenarios, the IDM imposes a discrete \mathbb{Z}_2 symmetry under which alone Φ_2 is odd. Under this symmetry, the lightest \mathbb{Z}_2 -odd particle is rendered stable and thus a DM candidate. Furthermore, the couplings will all be real, and so this model on its own provides no new source of CP violation [149, 174].

10.2 Construction of the effective potential

The analysis featured in this chapter is motivated by the recent results of Refs. [127, 149]. In order to build on them, the model was set up by closely adapting the prescriptions laid out therein. The present section outlines the shared construction of the effective potential and the parameter constraints implemented throughout.

10.2.1 Parametrization

First of all, the quartic couplings λ_3 , λ_4 and λ_5 will be absorbed into [\[149\]](#)

$$\lambda_{345} \stackrel{\text{def}}{=} \lambda_3 + \lambda_4 + \lambda_5 \quad (10.5)$$

$$\bar{\lambda}_{345} \stackrel{\text{def}}{=} \lambda_3 + \lambda_4 - \lambda_5 = \lambda_{345} - 2\lambda_5. \quad (10.6)$$

Secondly, the masses of the new particles associated to the Higgs doublets will be used as input parameters for the analysis. At tree-level, the scalar and pseudoscalar mass matrices, evaluated in the unitary gauge at the EW minimum $(h, H) = (v, 0)$, present the mass-square eigenvalues

$$m_h^2 = 2\lambda_1 v^2 \quad m_H^2 = \frac{1}{2}(2\mu_2^2 + \lambda_{345}v^2) \quad (10.7)$$

$$m_{\phi^\pm}^2 = 0 \quad m_{H^\pm}^2 = \frac{1}{2}(2\mu_2^2 + \lambda_3 v^2) \quad (10.8)$$

$$m_\phi^2 = 0 \quad m_A^2 = \frac{1}{2}(2\mu_2^2 + \bar{\lambda}_{345}v^2). \quad (10.9)$$

Consequently, the quartic couplings λ_3 , λ_4 and λ_5 can be completely removed via

$$\lambda_3 = \lambda_{345} + 2\frac{m_{H^\pm}^2 - m_H^2}{v^2}, \quad \lambda_4 = \frac{m_A^2 + m_H^2 - 2m_{H^\pm}^2}{v^2}, \quad \lambda_5 = \frac{m_H^2 - m_A^2}{v^2}. \quad (10.10)$$

In summary, the model admits a parameter transformation

$$\{\mu_1, \mu_2, \lambda_1, \lambda_2, \lambda_3, \lambda_4, \lambda_5\} \rightarrow \{v, \lambda_2, \lambda_{345}, m_h, m_H, m_{H^\pm}, m_A\} \quad (10.11)$$

with fixed $v \approx 246$ GeV and $m_h \approx 125$ GeV which will be exploited hereinafter.

10.2.2 Zero-temperature, field-dependent masses

The full, one-loop effective potential is constructed in line with the prescriptions of Chapter [8](#). The zero-temperature, one-loop corrections are provided by the CW potential [\(8.1\)](#), which features a dependence on the field-dependent masses of the model. Fermion masses in the IDM are inherited from the SM, as fermions completely decouple from the second doublet. The mass squares are thus

$$m_f^2(h, H) = \frac{y_f^2}{2} h^2. \quad (10.12)$$

This analysis restricts the fermion content to the top quark t . The zero-temperature mass squares of the gauge bosons γ , W^\pm and Z in turn are [\[149\]](#)

$$m_\gamma^2(h, H) = 0 \quad (10.13)$$

$$m_W^2(h, H) = \frac{g_2^2}{4}(h^2 + H^2) \quad (10.14)$$

$$m_Z^2(h, H) = \frac{g_1^2 + g_2^2}{4}(h^2 + H^2). \quad (10.15)$$

The model is complemented by the masses of the different scalars and pseudoscalars.

Their field-dependent mass matrices¹ are given as [\[149\]](#)

$$\mathcal{M}_s^2(h, H) = \begin{pmatrix} 3\lambda_1 h^2 - \lambda_1 v^2 + \frac{\lambda_{345}}{2} H^2 & hH\lambda_{345} \\ hH\lambda_{345} & 3\lambda_2 H^2 + \frac{1}{2}\lambda_{345} h^2 + \mu_2^2 \end{pmatrix} \quad (10.16)$$

$$\mathcal{M}_p^2(h, H) = \begin{pmatrix} \lambda_1 h^2 - \lambda_1 v^2 + \frac{1}{2}\bar{\lambda}_{345} H^2 & hH\lambda_5 \\ hH\lambda_5 & \lambda_2 H^2 + \frac{1}{2}\bar{\lambda}_{345} h^2 + \mu_2^2 \end{pmatrix} \quad (10.17)$$

$$\mathcal{M}_c^2(h, H) = \begin{pmatrix} \lambda_1 h^2 - \lambda_1 v^2 + \frac{1}{2}\lambda_3 H^2 & \frac{1}{2}hH(\lambda_4 + \lambda_5) \\ \frac{1}{2}hH(\lambda_4 + \lambda_5) & \lambda_2 H^2 + \frac{1}{2}\lambda_3 h^2 + \mu_2^2 \end{pmatrix}. \quad (10.18)$$

Their diagonalization delivers the field-dependent mass squares at zero temperature, which coincide with the mass squares [\(10.7\)](#) – [\(10.9\)](#) when evaluated at the vacuum.

10.2.3 Counterterm potential

Renormalization is completed by introducing the counterterm potential [\[149\]](#)

$$V_{\text{CT}}(h, H) = \delta\mu_h^2 h^2 + \delta\mu_H^2 H^2 + \delta\lambda_1 h^4. \quad (10.19)$$

Its coefficients are fixed by a set of renormalization conditions chosen such as to preserve the zero-temperature EW vacuum and the tree-level masses m_h and m_H after the CW corrections have been accounted for. It is pointed out that such renormalization schemes are often challenging: second and higher order derivatives of the Goldstone contributions to the CW potential [\(8.1\)](#) are dangerously ill-defined at the vacuum. A strict treatment of such pathological terms requires the introduction of IR cutoffs. Refs. [\[182\]](#), [\[183\]](#) provide a systematic procedure for renormalization conditions featuring up to second order derivatives, which was successfully applied

¹s: scalars – p: pseudoscalars – c: charged scalars.

to the recent analyses of Refs. [149, 160] and therefore also followed here. Its renormalization conditions impose

$$\left. \frac{\partial V_{\text{CT}}(h, H)}{\partial h} \right|_{\text{vev}} \stackrel{!}{=} - \left. \frac{\partial V_{\text{CW}}(h, H)}{\partial h} \right|_{\text{vev}} \quad (10.20)$$

$$\left. \frac{\partial^2 V_{\text{CT}}(h, H)}{\partial h^2} \right|_{\text{vev}} \stackrel{!}{=} - \left(\left. \frac{\partial^2 \tilde{V}_{\text{CW}}(h, H)}{\partial h^2} + \frac{1}{32\pi^2} \sum_{i=\phi, \phi^\pm} n_i \left(\frac{\partial m_i^2(h, H)}{\partial h} \right)^2 \ln \frac{m_{\text{IR}}^2}{Q^2} \right) \right|_{\text{vev}} \quad (10.21)$$

$$\left. \frac{\partial^2 V_{\text{CT}}(h, H)}{\partial H^2} \right|_{\text{vev}} \stackrel{!}{=} - \left(\left. \frac{\partial^2 \tilde{V}_{\text{CW}}(h, H)}{\partial H^2} + \frac{1}{32\pi^2} \sum_{i=\phi, \phi^\pm} n_i \left(\frac{\partial m_i^2(h, H)}{\partial h} \right)^2 \ln \frac{m_{\text{IR}}^2}{Q^2} \right) \right|_{\text{vev}} . \quad (10.22)$$

Notably, the scheme requires the CW potential \tilde{V}_{CW} on the right-hand side of Eqs. (10.21) and (10.22) to be evaluated without its Goldstone modes. The latter are added by hand, modulated by the logarithm of an IR cutoff set to $m_{\text{IR}}^2 = m_h^2$ at the vacuum. In return for curing the IR illness of the counterterm scheme, and as Ref. [149] points out, this set of conditions leaves the masses m_{A, H^\pm} as loop-corrected parameters, while the couplings λ_2 and λ_{345} in turn become running quantities. A refined and simultaneously IR divergence-free renormalization is left for future work.

10.2.4 Thermal mass corrections

The Debye masses of the scalars and pseudoscalars emerge as eigenvalues of the thermal mass matrices

$$\tilde{\mathcal{M}}_i^2(h, H, T) = \mathcal{M}_i^2(h, H) + \Pi(T) \quad (10.23)$$

with $i = \{s, p, c\}$. For all three matrices, the components of $\Pi(T)$ are given by [149, 160]

$$\Pi_{11}(T) = \left(6y_t^2 + \frac{3}{2}g_1^2 + \frac{9}{2}g_2^2 + 12\lambda_1 + 4\lambda_3 + 2\lambda_4 \right) \frac{T^2}{24} \quad (10.24)$$

$$\Pi_{22}(T) = \left(\frac{3}{2}g_1^2 + \frac{9}{2}g_2^2 + 12\lambda_2 + 4\lambda_3 + 2\lambda_4 \right) \frac{T^2}{24} \quad (10.25)$$

$$\Pi_{12}(T) = \Pi_{21}(T) \approx 0. \quad (10.26)$$

The thermal self-energies of the gauge boson modes are

$$\Pi_{W^\pm}^{\mathcal{L}}(T) = \Pi_{W^3}^{\mathcal{L}}(T) = 2g_2^2 T^2 \quad \Pi_{W^\pm}^{\mathcal{T}}(T) = \Pi_{W^3}^{\mathcal{T}}(T) = 0 \quad (10.27)$$

$$\Pi_B^{\mathcal{L}}(T) = 2g_1^2 T^2 \quad \Pi_B^{\mathcal{T}}(T) = 0 \quad (10.28)$$

Thus, the mass square of the longitudinal W boson modes becomes

$$\tilde{m}_{W_{\tilde{L}}^\pm}^2(h, H, T) = \frac{g_2^2}{2}(h^2 + H^2) + 2g_2^2 T^2. \quad (10.29)$$

For the longitudinal photon and Z boson modes, the thermal corrections deliver

$$\tilde{m}_{Z_{\mathcal{L}}, \gamma_{\mathcal{L}}}^2(h, H, T) = \frac{1}{8}(g_1^2 + g_2^2)(h^2 + H^2) + (g_1^2 + g_2^2)T^2 \pm \Delta \quad (10.30)$$

with

$$\Delta^2 = \frac{1}{64}(g_1^2 + g_2^2)(h^2 + H^2 + 8T^2)^2 - g_1^2 g_2^2 T^2 (h^2 + H^2 + 4T^2). \quad (10.31)$$

The thermal mass corrections will be applied in line with the standard truncated full dressing procedure of Eq. (8.11), since – as noted by Ref. [149] – the high-temperature assumption for the alternative treatment may not hold in the region studied. The full thermal effective potential is thus

$$V_{\text{eff}}(h, H; T) = V_{\text{tree}}(h, H) + V_{\text{CW}}(h, H) + V_{\text{CT}}(h, H) + V_1^{\text{th}}(h, H; T), \quad (10.32)$$

with the replacement $m_i^2(h, H) \rightarrow \tilde{m}_i^2(h, H) = m_i^2(h, H) + \Pi_i(T)$ in V_{CW} and V_1^{th} .

10.3 Constraints on the model parameters

As has been pointed out, Refs. [127], [149] have highlighted specific regions of parameter space. Within these, it is possible to account for both a SFOPhT as well as a correct DM relic abundance. The present work aims to shed some light on these regions in the hopes of refining the search for viable parameter sets. This goal has motivated all parameter choices of the later analysis; the ranges considered are showcased in Table [10.1]. The last parameter appearing in the table is the *mass splitting*, defined as

$$\Delta m \stackrel{\text{def}}{=} m_{A, H^\pm} - m_H. \quad (10.33)$$

The mass splitting has been shown to be a convenient input parameter in studies

Table 10.1: Parameter space used throughout this chapter, on the basis of Refs. [127, 149]. The upper bounds on m_{H^\pm} and m_A follow from the bound considered for Δm , which was chosen such as to generously cover the regions explored by the mentioned references while remaining well within the EW scale. The lower bound on m_{H^\pm} is motivated by reassessments of LEP data with regards to new physics [149, 184–186]. The same analyses also exclude the intersection of regions $m_A > 100 \text{ GeV} \cup m_A - m_H < 8 \text{ GeV}$.

Parameter space					
λ_2	λ_{345}	$m_H [\text{GeV}]$	$m_A [\text{GeV}]$	$m_{H^\pm} [\text{GeV}]$	$\Delta m [\text{GeV}]$
≤ 10	$[-0.01, 0.01]$	$[55, 75]$	≤ 675	$[70, 675]$	≤ 600

of the EWPhT, as it allows to easily cover heterogeneous phase transition regimes (see *e.g.* Refs. [127, 149, 160, 174, 187]). The underlying assumption when using Δm throughout this work is $m_A = m_{H^\pm}$, which is very restrictive. Nonetheless, Δm will be a useful asset.

Parameter selections within the ranges considered were examined for a number of theoretical and experimental constraints outlined in the following (cf. Refs. [127, 149]).

10.3.1 Theoretical constraints

Boundedness and vacuum stability

Firstly, in order to ensure a charge-conserving ground state,

$$\lambda_4 - |\lambda_5| < 0 \quad (10.34)$$

is required. Furthermore, as the behaviour of the potential at large field values is dictated by its quartic terms, stability is enforced by restricting their parameters such that [149, 181]

$$\lambda_1, \lambda_2 > 0, \quad \lambda_3 > -2\sqrt{\lambda_1\lambda_2}, \quad \lambda_3 + \lambda_4 - |\lambda_5| > -2\sqrt{\lambda_1\lambda_2}. \quad (10.35)$$

Perturbative unitarity

Perturbative unitarity is imposed on the S matrix for all processes involving scalars. This requires all of its eigenvalues to satisfy

$$|w_l| \leq 8\pi. \quad (10.36)$$

Details on the S matrix can be inferred from Appendix H and Ref. [181].

10.3.2 Experimental constraints

Suppression of exotic gauge boson decays

In conformity with Refs. [149, 181], decays of the gauge bosons into H , H^\pm or A shall be kinematically excluded by requiring

$$m_A + m_{H^\pm} > m_{W^\pm} \qquad m_H + m_{H^\pm} > m_{W^\pm} \qquad (10.37)$$

$$m_A + m_H > m_Z \qquad 2m_{H^\pm} > m_Z. \qquad (10.38)$$

Suppression of exotic Higgs decays

In the SM, the total Higgs decay width is estimated as [188]

$$\Gamma_h^{\text{SM}} = 4.07 \text{ MeV}_{-3.9\%}^{+4.0\%}. \qquad (10.39)$$

Exotic and so far unobserved decays of the Higgs h into the new state H should widen Γ_h^{SM} by [127, 149]

$$\Gamma_h^{\text{inv}} = \frac{\lambda_{345}^2 m_{W^\pm}^2}{8\pi g_2^2 m_h} \sqrt{1 - 4 \left(\frac{m_H}{m_h} \right)^2}. \qquad (10.40)$$

The invisible decay width Γ_h^{inv} is restricted by upper limits on the branching ratio

$$\mathcal{B}_h^{\text{inv}} \stackrel{\text{def}}{=} \frac{\Gamma_h^{\text{inv}}}{\Gamma_h^{\text{SM}} + \Gamma_h^{\text{inv}}} \qquad (10.41)$$

claimed independently by the ATLAS and CMS collaborations at 95% confidence level [189, 190]. Parameter sets in this analysis were required to meet the limit $\mathcal{B}_h^{\text{inv}} < 0.26$ of the former.

Oblique parameters S , T and U

Overall, in order to satisfy experimental bounds, the effects of exotic physics on EW precision observables need to be small [191]. This is quantified by the Peskin-Takeuchi observables (*e.g.* Ref. [192]). Parameter sets making it into the final analysis all satisfy the bounds [191]

$$S = 0.06 \pm 0.09 \qquad (10.42)$$

$$T = 0.10 \pm 0.07 \qquad (10.43)$$

with the fit constraint $U = 0$. The parametrizations of S and T can be found in Appendix [H](#).

10.4 Construction of the electroweak sphaleron

The generic two-doublet case presents the energy functional [153, 193]

$$\mathcal{E}[W_\mu^a, \Phi_1, \Phi_2] = \int d^3x \left[\frac{1}{4} W_{ij}^a W^{aj} + (\mathcal{D}_i \Phi_k)^\dagger (\mathcal{D}^i \Phi_k) + \Delta V_{\text{eff}}^T(\Phi_1, \Phi_2) \right], \quad (10.44)$$

with $a, i, j = 1, 2, 3$ and $k = 1, 2$. In order to evaluate the energy with respect to the absolute vacuum of the theory at temperature T , and thus in agreement with the implicit normalization of Eq. (5.3), the quantity

$$\Delta V_{\text{eff}}^T(\Phi_1, \Phi_2) \stackrel{\text{def}}{=} V_{\text{eff}}(\Phi_1, \Phi_2, T) - V_{\text{eff}}(\Phi_1, \Phi_2, T)|_{\text{vev}} \quad (10.45)$$

is introduced. Furthermore, in order to impose a radial gauge condition, spherical coordinates are favored anew. This motivates the use of a standard radial coordinate r , which can be made dimensionless via

$$\xi \stackrel{\text{def}}{=} g_2 r \Omega \quad \text{with} \quad \Omega \stackrel{\text{def}}{=} \sqrt{v_1^2 + v_2^2}, \quad (10.46)$$

the quantities $v_1 = v_1(T)$ and $v_2 = v_2(T)$ being the temperature-dependent VEVs of the fields h and H . Following Chapter 5 and the derivation for the general 2HDM case in Ref. [153], the spherically symmetric field ansatz

$$\Phi_1(\xi, \theta, \phi; \mu) = h_1(\xi) \Phi^\infty(\theta, \phi; \mu) + (1 - h_1(\xi)) \frac{v_1}{\sqrt{2}} \begin{pmatrix} 0 \\ e^{-i\mu} \cos \mu \end{pmatrix} \quad (10.47)$$

$$\Phi_2(\xi, \theta, \phi; \mu) = h_2(\xi) \Phi^\infty(\theta, \phi; \mu) + (1 - h_2(\xi)) \frac{v_2}{\sqrt{2}} \begin{pmatrix} 0 \\ e^{-i\mu} \cos \mu \end{pmatrix} \quad (10.48)$$

$$W_\xi(\xi, \theta, \phi; \mu) = 0 \quad (10.49)$$

$$W_\theta(\xi, \theta, \phi; \mu) = f(\xi) W_\theta^\infty(\theta, \phi; \mu) \quad (10.50)$$

$$W_\phi(\xi, \theta, \phi; \mu) = f(\xi) W_\phi^\infty(\theta, \phi; \mu) \quad (10.51)$$

is used, where the loop Φ^∞ is defined according to Eq. (5.12) with the loop parameter $\mu \in [0, \pi]$. The fields h and H

$$h(\xi) \stackrel{\text{def}}{=} v_1 h_1(\xi) \quad \quad \quad H(\xi) \stackrel{\text{def}}{=} v_2 h_2(\xi) \quad (10.52)$$

are thus treated as the sole dynamical fields, while all other fields in the doublets are consistently set to zero. For $\mu = \pi/2$, and omitting the ξ -dependences for the

sake of clarity, the ansatz delivers the energy functional

$$\begin{aligned} \mathcal{E}[f, h_1, h_2] = & \frac{4\pi\Omega}{g_2} \int_0^\infty d\xi \left\{ 4 \left(\frac{df}{d\xi} \right)^2 + \frac{8}{\xi^2} f^2 (1-f)^2 + \frac{\xi^2 v_1^2}{2 \Omega^2} \left(\frac{dh_1}{d\xi} \right)^2 \right. \\ & \left. + \frac{\xi^2 v_2^2}{2 \Omega^2} \left(\frac{dh_2}{d\xi} \right)^2 + \left(\frac{v_1^2}{\Omega^2} h_1^2 + \frac{v_2^2}{\Omega^2} h_2^2 \right) (1-f)^2 + \frac{\xi^2}{g_2^2 \Omega^4} \Delta V_{\text{eff}}^T(h_1, h_2) \right\}. \end{aligned} \quad (10.53)$$

In conformity with Eq. (10.45), the quantity $\Delta V_{\text{eff}}^T(h_1, h_2)$ is to be understood as

$$\Delta V_{\text{eff}}^T(h_1, h_2) = V_{\text{eff}}(v_1 h_1, v_2 h_2, T) - V_{\text{eff}}(v_1, v_2, T). \quad (10.54)$$

The radial functions f , h_1 and h_2 need to satisfy

$$\lim_{\xi \rightarrow 0} f(\xi) = 0 \quad \lim_{\xi \rightarrow 0} h_1(\xi) = 0 \quad \lim_{\xi \rightarrow 0} h_2(\xi) = 0 \quad (10.55)$$

$$\lim_{\xi \rightarrow \infty} f(\xi) = 1 \quad \lim_{\xi \rightarrow \infty} h_1(\xi) = 1 \quad \lim_{\xi \rightarrow \infty} h_2(\xi) = 1. \quad (10.56)$$

The static equations for the generic two-doublet case are obtained as

$$\xi^2 \frac{\partial^2 f}{\partial \xi^2} = 2f(1-f)(1-2f) - \left(\frac{v_1^2}{4\Omega^2} \xi^2 h_1^2 + \frac{v_2^2}{4\Omega^2} \xi^2 h_2^2 \right) \cdot (1-f) \quad (10.57)$$

$$\frac{\partial}{\partial \xi} \left(\xi^2 \frac{\partial h_1}{\partial \xi} \right) = 2h_1(1-f)^2 + \frac{\xi^2}{g_2^2 v_1^2 \Omega^2} \frac{\partial}{\partial h_1} \Delta V_{\text{eff}}^T(h_1, h_2) \quad (10.58)$$

$$\frac{\partial}{\partial \xi} \left(\xi^2 \frac{\partial h_2}{\partial \xi} \right) = 2h_2(1-f)^2 + \frac{\xi^2}{g_2^2 v_2^2 \Omega^2} \frac{\partial}{\partial h_2} \Delta V_{\text{eff}}^T(h_1, h_2). \quad (10.59)$$

However, a special scenario arises whenever one of the doublets is evaluated at $\langle \Phi_l \rangle = 0$ and thus $v_l = 0$. In such cases, the kinetic terms in Eq. (10.53) corresponding to the degree of freedom of the doublet ϕ_l all vanish, which reduces the system of equations to

$$\xi^2 \frac{\partial^2 f}{\partial \xi^2} = 2f(1-f)(1-2f) - \frac{1}{4} \xi^2 h_k^2 \cdot (1-f) \quad (10.60)$$

$$\frac{\partial}{\partial \xi} \left(\xi^2 \frac{\partial h_k}{\partial \xi} \right) = 2h_k(1-f)^2 + \frac{\xi^2}{g_2^2 v_k^4} \frac{\partial}{\partial h_k} \Delta V_{\text{eff}}(h_k, 0) \quad (10.61)$$

for $k \in \{1, 2\}$, $k \neq l$. The boundary conditions for the remaining radial functions correspond to (10.55) – (10.56).

The sphaleron energy is obtained by evaluating Eq. (10.53) at the solutions f , h_1 and h_2 to the static equations. Furthermore, as long as no mixed kinetic Higgs terms appear in the Lagrangian, $U(1)$ corrections to the sphaleron energy are easily accounted for in generic multi-Higgs-doublet scenarios: each doublet gives rise to a term (5.22). For any inert doublets, such terms automatically result in zero.

10.5 Investigation of the decoupling criteria

10.5.1 Selection of benchmark points

Ref. [149] reports the dominance of a one-step phase transition pattern which has the doublet Φ_2 remain inert throughout the entire process, *i.e.* it presents a zero VEV in both EW phases at all temperatures. This pattern features first- and second-order processes alike, of which only the former will be of interest. Selected benchmark points (BMPs) displaying such FOPhT are kept in Table 10.2 for future reference. Furthermore, Ref. [149] crucially remarks the existence of narrow but well-defined regions of parameter space allowing for two-step phase transitions, with a first instance of symmetry breaking solely along the axis of the second Higgs field. Although a study of the transition strength in such cases should be interesting, the tentative scans of parameter space carried out with `CosmoTransitions` did not find suitable two-step phase transitions. It is pointed out that comprehensive scans of the space spanned by Table 10.1 are beyond the scope of this work; nonetheless, the scan setup was chosen such as to accurately resolve the narrow regions in question – to no avail. Accordingly, the following analysis of the sphaleron decoupling criterion is restricted to the one-step pattern available.

Table 10.2: BMPs used for a first characterization of the sphaleron.

	BMP1	BMP2	BMP3
PT pattern	1-step	1-step	1-step
m_H [GeV]	65	70	55
m_A [GeV]	340	364	400
m_{H^\pm} [GeV]	340	364	400
λ_2	0.0025	0.0025	1.5000
λ_{345}	0.0050	-0.0050	-0.0030
\mathcal{E}_0 [GeV]	9055.01	9080.05	9073.80
T_n [GeV]	106.41	99.85	81.99
$v_{1,n}$ [GeV]	187.78	203.49	228.58
\mathcal{E}_n [GeV]	6477.03	7167.86	8138.50
T_c [GeV]	111.23	104.95	95.11
$v_{1,c}$ [GeV]	168.51	188.79	211.44
\mathcal{E}_c [GeV]	5726.6	6326.90	7404.13

10.5.2 Characterization of the sphaleron

The BMPs of Table 10.2 provided first insights into the sphaleron. To this aim, the sphaleron solutions to Eqs. (10.60)–(10.61) were obtained with the relaxation algorithm introduced in Chapter 9. Resting on the phase transition pattern considered, the sphaleron solutions for the gauge and standard Higgs fields showcased in Fig. 10.1 exhibit the physiognomy and convergence behaviour known from Chapter 5. In addition, the figure also displays the effects of temperature on the sphaleron: whereas the continuous lines correspond to the sphaleron solution at zero temperature, the dotted lines showcase solutions obtained at the respective T_n , which were obtained with CosmoTransitions. One observes that the lower T_n and T altogether, the higher the radial field profile. This explains the contrast between the upper and lower rows of the figure. In the case of BMP3, the phase transition occurs at a temperature about 20 GeV below those of BMP1 and BMP2, which results in nucleation curves that closer resemble the zero-temperature profiles.

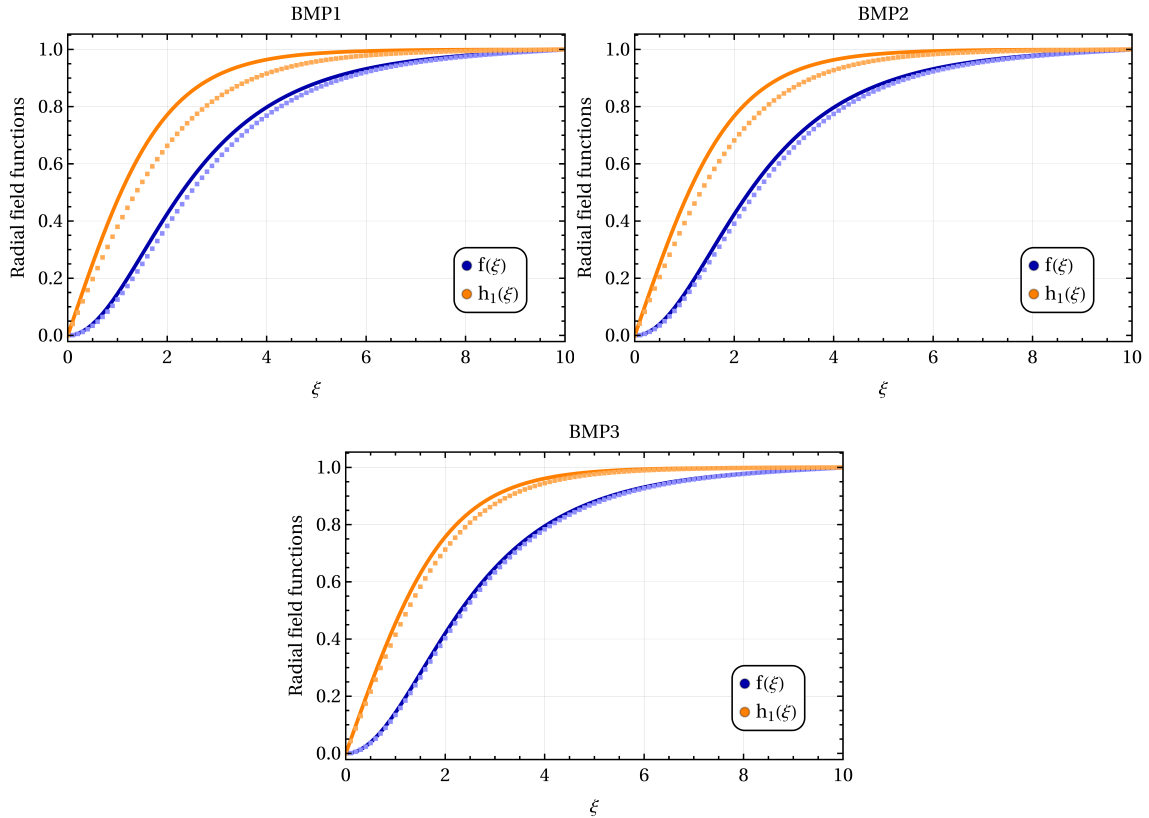


Figure 10.1: Exemplary sphaleron curves for the BMPs in Table 10.2. The continuous lines correspond to the zero-temperature solutions of Eqs. (10.60)–(10.61), whereas the dotted lines were obtained at the respective nucleation temperatures.

This trend is symptomatic of a general temperature dependence which acts, in particular, through the temperature-dependent VEV $v_1(T)$. The sphaleron character and its energy are ultimately pinned down by the evolution of $v_1(T)$, as showcased by Fig. 10.2. The sphaleron energies $\mathcal{E}(T)$ were calculated from Eqs. (10.53) and (5.22) on the basis of solutions to Eqs. (10.60)–(10.61) obtained at the corresponding temperature. The thermal evolution of $v_1(T)$ was tracked with `CosmoTransitions`. The inertness of Φ_2 in Eq. (10.53) on account of $v_2(T) = 0$ is stressed again for later reference. The left-hand side plots hint at the close relation of $\mathcal{E}(T)$ and $v_1(T)$, for which the evolution is displayed from the critical temperature all the way down to zero temperature. This behaviour is the consequence of an approximate scaling law for $v_1(T)$ as given by Eq. (7.11). In view of the right-hand side plots of Fig. 10.2, the validity of the scaling law is suggested for these BMPs. The proportionality is not exact; however, it does coincide well for the BMPs displayed.

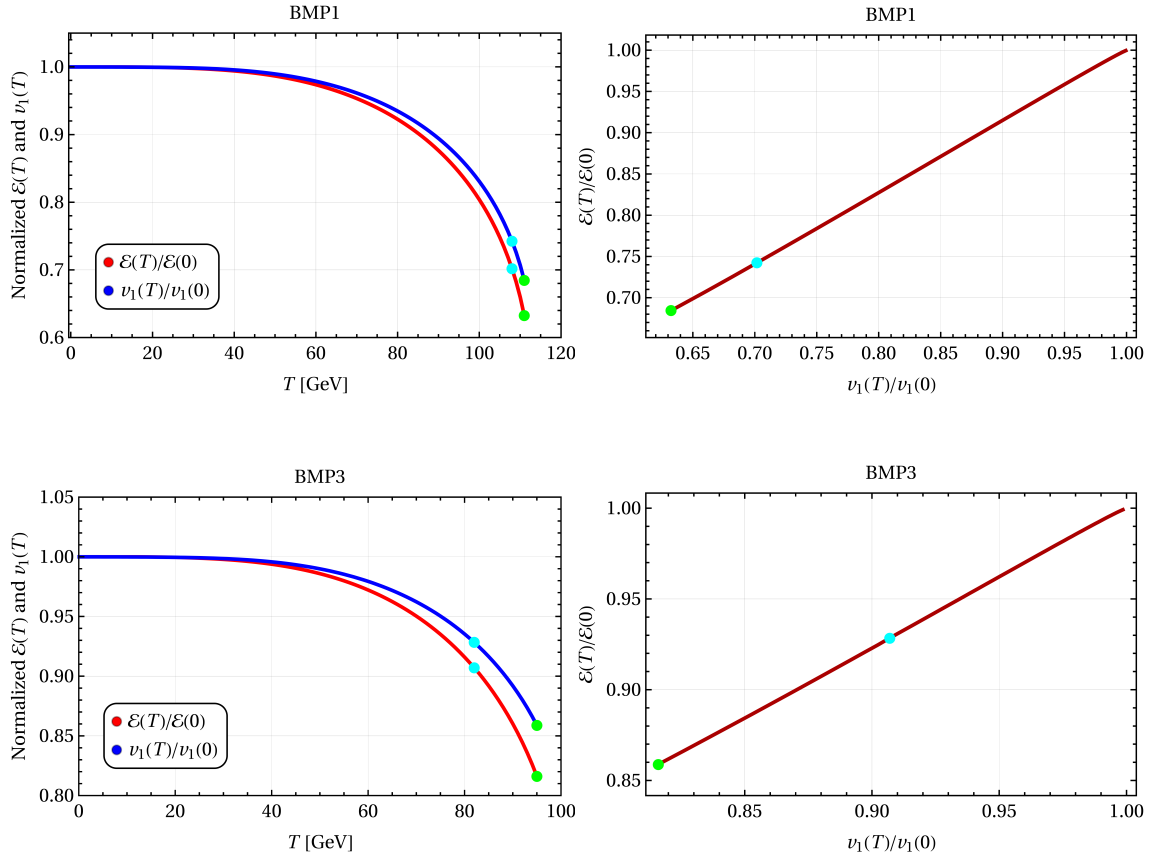


Figure 10.2: LEFT: Temperature-dependent evolution of the normalized vacuum expectation values and sphaleron energies for BMP1 and BMP3 in Table 10.2. RIGHT: Scaling of the $U(1)$ -corrected $\mathcal{E}(T)$ with $v_1(T)$. Cyan (green) points were obtained at T_n (T_c).

10.5.3 SFOPhTs and sphaleron decoupling in the IDM

The preliminary case study of BMPs 1 and 3 suggests the validity of the approximate scaling law (7.11) for $v_1(T)$ in the IDM. This is the essential ingredient in reducing the unwieldy σ -criterion to a more convenient condition on the order parameter $\xi = v_1(T)/T$ for the transition pattern considered. Given the modest additional structure of the IDM and the inertness of the second doublet in this process, the canonical $\xi \gtrsim 1$ should be safe. It is noted that in the derivation of this criterion, the only free scale featured in Eq. (7.12) aside from v_i and T_i is that of $\mathcal{E}(0)$. As can be inferred from Table 10.2, for the selected BMPs this scale is of 9 TeV and thus tallies with that of $\mathcal{E}_{\text{SM}}(0)$ as suggested in the literature (see *e.g.* Ref. [30]) and Fig. 9.1. For this reason, a criterion $\xi \gtrsim \mathcal{O}(1)$ can be expected.

Nonetheless, this work sets out to optimize this criterion by comparing and contrasting it to the seminal σ -criterion (7.10). A non-trivial assumption that underlies the following analysis concerns the sphaleron-related parameters which appear in Eq. (7.7) and define the range of the σ -criterion. The SM values of Appendix F will be assumed for them, since – to the knowledge of the author – their calculation in exotic models is largely missing to this day. Relying on the modest extension that the IDM constitutes, the large bounds chosen for κ and the sub-leading logarithmic impact of these parameters on Eq. (7.7), this work follows Refs. [122, 153, 155] in assuming that the canonical σ -criterion should remain reliable.

The first part of this analysis proceeded as an extension of the BMP case study: in order to track ξ , BMPs 1 and 3 of Table 10.2 were used as seeds for two one-dimensional scans through parameter space along Δm within the ranges indicated by Table 10.1. This choice was motivated by the dependence of three quartic couplings on the masses m_A , m_{H^\pm} and m_H via Eqs. (10.10). Under the degeneracy condition of m_A and m_{H^\pm} , it is possible to recast three quartic couplings in terms of Δm and thus to maximize the impact of a single parameter on the phase transition. This simple reparametrization permits to cover heterogeneous regions of parameter space in a simple manner, as shown by Ref. [149]. In particular, Δm was found to have a greater impact on the evolution of ξ as compared to the remaining independent parameters², λ_2 and λ_{345} , thus justifying the approach.

²This holds especially for λ_{345} as a result of the highly constrained parameter space considered.

A basic understanding of the phase transition strength ξ is provided by preliminary results of these scans. Fig. 10.3 displays the evolution of T and $v_1(T)$ at the phase transition, while Fig. 10.4 showcases the corresponding development of the phase transition strength. The scans were carried out at criticality and nucleation; the relevant quantities are correspondingly deemed T_i , v_i , ξ_i for $i \in \{c, n\}$. The first observation concerns the temperatures and VEVs: beyond the range of low Δm , the T_c are markedly higher and the v_c lower than their counterparts at nucleation. These differences increase further as Δm rises and can have a sizeable impact on the evaluation of ξ . For BMPs 1 and 3, marked in red (green) for evaluation at T_n (T_c), the effects are moderate: the greatest difference is obtained for BMP3, with $|\xi_n - \xi_c| \approx 0.6$. However, the stark decrease of T_n with Δm , as opposed to the more moderate behaviour of T_c , v_c and v_n , results in a rapidly augmenting $|\xi_n - \xi_c|$. The evolution of ξ_c in Fig. 10.4 is rendered overall flatter than that of ξ_n . As a result, the phase transition strength ξ_c will generally be weaker than its counterpart ξ_n .

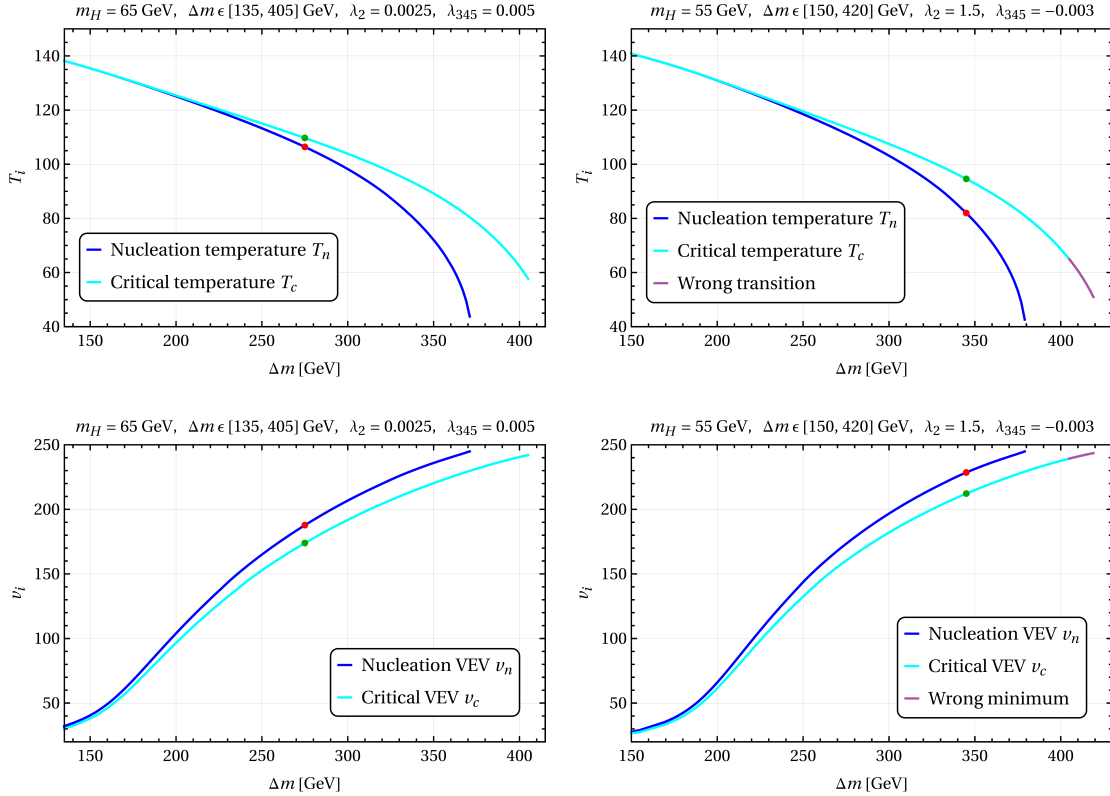


Figure 10.3: Evolution of T_i and $v_1(T_i)$ evaluated at criticality and bubble nucleation as a function of the mass splitting Δm . The green and red points mark the BMP in the respective evaluation. The cutoff towards large Δm stems from the requirement of correct minimality of the model at zero temperature. LEFT: Containing BMP1. RIGHT: Containing BMP3.

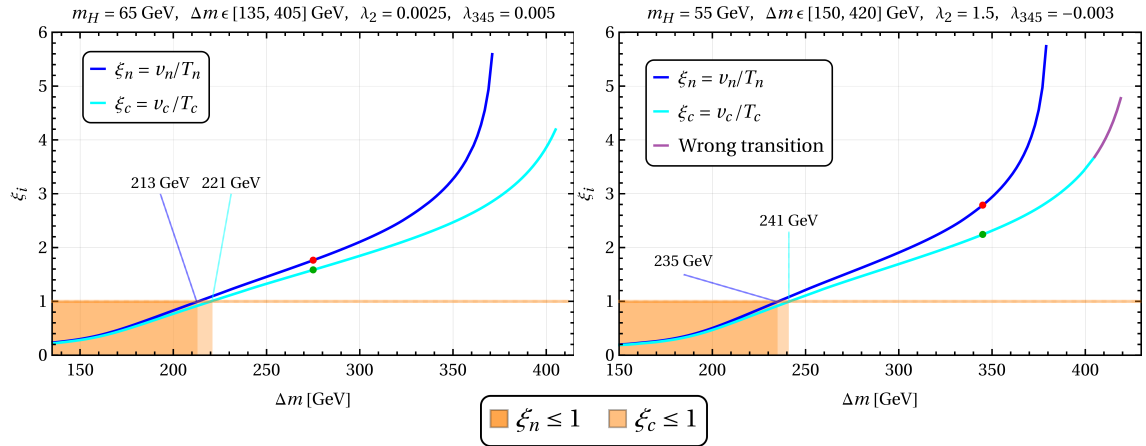


Figure 10.4: Evolution of the standard phase transition strength ξ_i evaluated at criticality and bubble nucleation. The green and red points mark the BMP in the respective evaluation.

Under the standard requirement that $\xi \gtrsim 1$, the lower bound on the scan parameter Δm is thus consistently shifted upwards when evaluated for ξ_c . For the scans featured in Fig. 10.4, this shift amounts to 6 – 8 GeV with respect to the parameter bound set by $\xi_n \gtrsim 1$. Additionally, an evaluation of the phase transition strength ξ_c spuriously extends the range available for a SFOPhT towards large values of the scan parameter: it includes regions of Δm which feature no bubble nucleation as judged by Eq. (6.24) in Chapter 6 (*i.e.* beyond approximately $\Delta m \gtrsim 370 - 380$ GeV for the scans displayed). Altogether, evaluation of the phase transition strength at criticality shifts the bounds available for a SFOPhT and thus leads to systematic misjudgements of the parameter space available for EWBG.

Another point regarding the independent issue of nucleation needs to be addressed on account of the right-hand side plots of Figs. 10.3 and 10.4. As the left-hand side plots, they are cut off to the right by the requirement that the EW vacuum be the absolute potential minimum at zero temperature. This includes the purple sections of the curves for T_c , v_c and ξ_c . In these regions, `CosmoTransitions` also detects a T_c for a transition to the correct vacuum which, however, does not come to pass. Instead, a SOPhT below T_c is reported which eventually lands on a wrong phase at zero temperature – despite the EW minimum being the true vacuum. This phenomenology shows that standard evaluations of phase transitions at the critical temperature fail to capture the finer details of transition dynamics on a fundamental level. Although the importance of this realization goes beyond EWBG, it suggests inherent flaws to standard evaluations of the phase transition strength

in the literature: the widely missing checks for successful nucleation are imperative. This work is not the first one to remark the importance of nucleation and T_n in the context of EWBG (see *e.g.* Ref. [145]), and previous studies of the IDM such as Ref. [174] have already implemented checks for nucleation in their framework. To the best knowledge of the author, however, a thorough qualitative and quantitative assessment of the effects of such checks on the phase transition strength ξ as in Fig. 10.4 has been pending in the context of the IDM.

The differences between evaluations of ξ at T_c and T_n are largely passed on to evaluations of the seminal decoupling condition σ , which were performed for the same scans of Δm . As can be inferred from Fig. 10.5, the bounds³ on the scan parameter Δm set by σ_c are consistently higher than those set by σ_n . In particular, the more stringent requirement that $\sigma_c > 42.8$ (upper edge of the orange stripes) projects onto a bound on Δm about 11 GeV more severe than the bound set by the $\sigma_n > 42.8$ in both scans. More fundamentally, and as pertains to the nature of this work, the modesty of the ξ -criterion for a SFOPhT is hinted at in comparison to Fig. 10.4. Irrespective of evaluation at criticality or nucleation, the σ -criterion reduces the available parameter space at the lower end of the spectrum of Δm for the cases studied. For instance, for the left-hand side plots of Figs. 10.4 and 10.5, one can track shifts of between 7 – 30 GeV depending on the bound for σ .

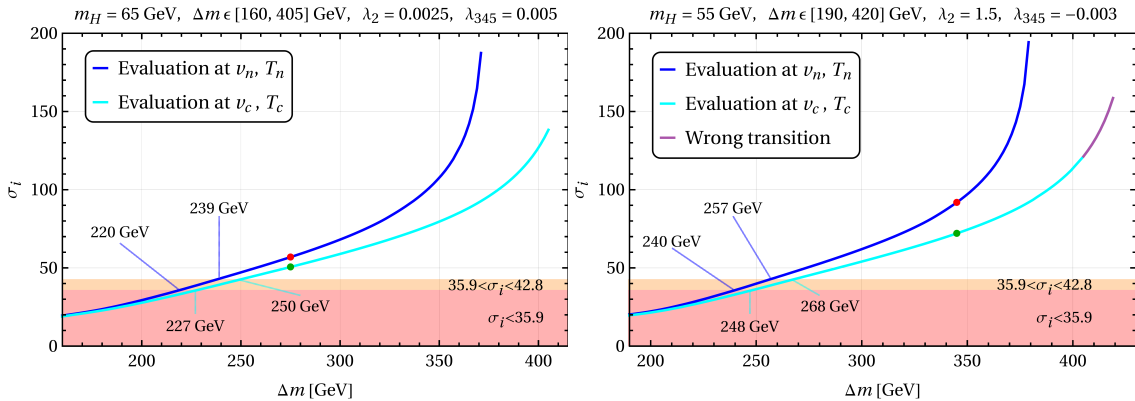


Figure 10.5: Evolution of σ_i at criticality and bubble nucleation. LEFT: Scan containing BMP1. RIGHT: Scan containing BMP3. In red (orange), the exclusion limit as set by the lower (upper) bound of σ_i . Red (green) points mark σ_n (σ_c) for the respective BMP.

³Also, note the reduced plotting range as compared to previous figures. Calculations of $\mathcal{E}(T)$ and σ can be spoiled by finite-mesh effects at low Δm , as explained in Appendix H.1.3.

Overall, two preliminary conclusions can be drawn. Firstly, in studies of SFOPhTs, the criteria σ_c and ξ_c need to be complemented by checks for nucleation and are instead best evaluated at T_n altogether. This should serve to avoid both an overestimation and a systematic misinterpretation of the parameter space available for such transitions. Secondly, the σ -criterion appears to be slightly more exclusive than the ξ -criterion. The corrections it provides are arguably modest; nonetheless, they can serve to refine the bound on ξ in what could constitute a procedural improvement to studies of the phase transition in the model.

In order to estimate the shift in the canonical ξ -condition, both criteria are plotted against each other. For the sake of completeness, this is first done in Fig. 10.6 for the benchmark scans considered so far. The upper row showcases the basic relation between ξ_i and σ_i for $i \in \{c, n\}$. The lower row displays the dominant contribution to σ_i , the quotient $\mathcal{E}(T_i)/T_i$, which sources the overall linear scaling of σ_i with ξ_i .

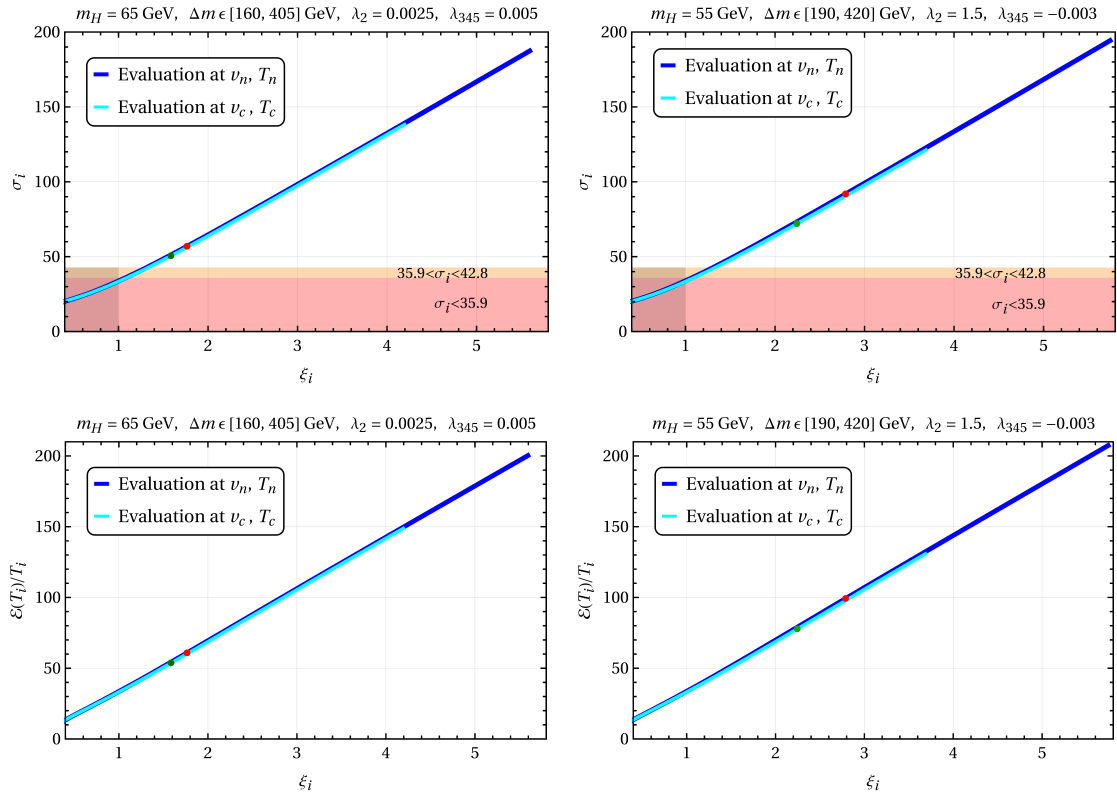


Figure 10.6: UPPER ROW: Comparison of the criteria on σ_i and ξ_i for a SFOPhT along the previous scans of Δm . The shaded region in the lower left corners marks the exclusion zone of the standard $\xi \gtrsim 1$. LOWER ROW: Scaling behaviour of $\mathcal{E}(T_i)/T_i$ with ξ_i along the previous scans of Δm . In both rows, the red (green) points correspond to the BMPs as evaluated at T_n (T_c), respectively. The purple regions from earlier plots were not included.

However, the proportionality in the σ - ξ relation is spoiled for $\xi_i \lesssim 1$ as the sub-leading logarithmic contributions to Eq. (7.9) become sizeable. Specifically, it is the term proportional to $\log(\xi_i)$ that raises σ_i for low values of ξ_i .

On a separate note, Fig. 10.6 shows $\mathcal{E}(T_i)/T_i$ and σ_i to possess the same scaling with ξ_i irrespective of evaluation at criticality or nucleation. The values of σ and ξ for single points will still vary between both temperature schemes, as shown by the relative shift of the red and green points. The phase transition will always be stronger when evaluated at T_n , in agreement with the analysis so far, and thus suggest better prospects of a SFOPhT. However, the updated bounds of the ξ -criterion, determined as the abscissae at which the curves cross the σ -bounds, will be comparable for both temperature schemes.

The improved bounds on the ξ -criterion are determined on the basis of a random sample of 800 points within the space of parameters of Table 10.1, unconstrained by the degeneracy condition on m_A and m_H^\pm and evaluated at T_n . Fig. 10.7 showcases the scaling of $\mathcal{E}(T_n)/T_n$, the dominant contribution to σ_n , while Fig. 10.8 presents σ_n itself. The color schemes of these plots provide some interesting insights. For instance, many sample points present $\mathcal{E}(T_n)$ at or above the 9 TeV scale of the zero temperature SM sphaleron according to Fig. 10.7. As the color scheme of Fig. 10.8 reveals, such high sphaleron energies are linked to temperature-dependent VEVs close to the zero-temperature value. More fundamentally, a comparison of the schemes suggests a linear scaling between $\mathcal{E}(T_n)$ and $v_{1,n}$ across the sample.

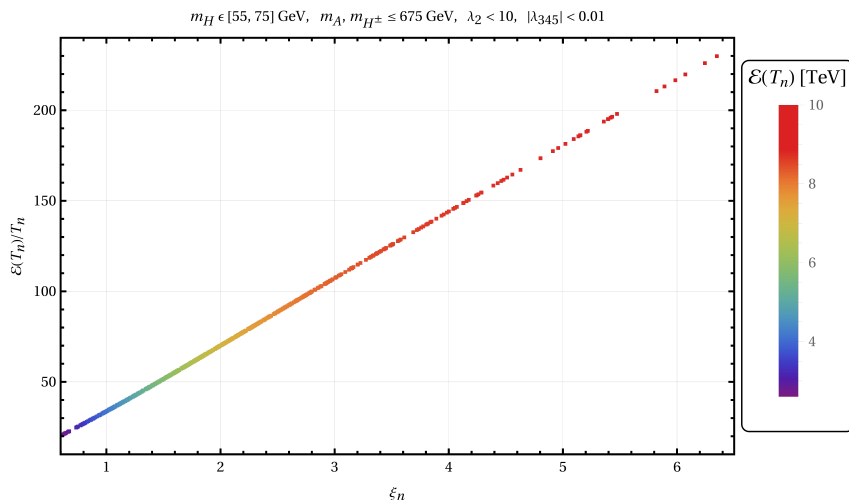


Figure 10.7: Scaling of $\mathcal{E}(T_n)/T_n$ in the IDM for a random sample of 800 points. The sphaleron energy at T_n appears color-coded.

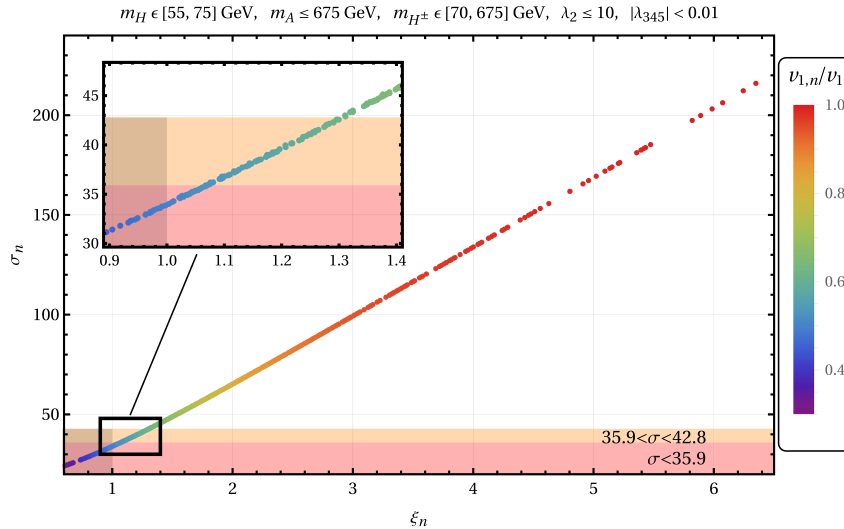


Figure 10.8: Comparison of the criteria on σ_n and ξ_n corresponding to a random selection of 800 points within the space of parameters of Table 10.1. The condition $m_A = m_{H^\pm}$ is lifted. The color code of the points showcases the normalized nucleation VEVs.

Fig. 10.8 ultimately compares the criteria on σ_n and ξ_n . As can be deduced from the magnification in Fig. 10.8, the standard condition that $\xi \gtrsim 1$ falls slightly short, as the curve implied by the data does not manage to cross any of the bounds on σ within the shaded regions. Instead, it suggests the formal condition (7.10) on σ_n to be satisfied for

$$\xi_n \gtrsim (1.05 - 1.30). \quad (10.62)$$

The minimal dispersion of the sample points along slices of constant σ is noted. It is recalled that the parameter space considered in Table 10.1 is very reduced for selected parameters; in addition, the experimental constraints imposed throughout section 10.3 further limit the variability of the final data points. In view of the sampling procedure, and noting that parametric dependences of ξ_n on the sampling parameters seem to be well reproduced by σ_n as suggested by Figs. 10.4 and 10.5, the negligible horizontal dispersion in the $\sigma - \xi$ relation should be a natural consequence. This could be put to the test in another random scan by either enlarging the parameter space of 10.1 or dropping some of the constraints imposed – which was beyond the scope and goals of this work. At any rate, the minimal dispersion renders the uncertainty on σ – the height of the orange stripe in Fig. 10.8 – the predominant uncertainty factor in the final result. In light of the state of the art in multi-model calculations of the fluctuation determinant κ , which sources the bounds

on σ , this final uncertainty is at present irreducible.

To the knowledge of the author, this is the first analysis of the sphaleron decoupling criterion in the IDM and thus eludes direct comparisons to equivalent results. A comparable reference value may lie in an analysis of the decoupling condition in the general 2HDM case. On the basis of a BMP case study at the critical temperature and in an approach equivalent to assuming the upper limit on σ_c , Ref. [187] suggests the improved condition $\xi_c \gtrsim 1.2$. This lies well within the bounds of the present work, yet falls short of the upper limit herein proposed. Ultimately, within the bounds on σ_n , the result (10.62) heightens the standardized ξ -criterion by 5% – 30%. The increased severity cannot, however, be unequivocally attributed to the effects of new physics and instead largely agrees with the more nuanced bounds suggested in Eq. (7.15) in a SM context.

Chapter 11

Real scalar singlet extension

The class of real scalar singlet extensions of the Higgs sector is one of the workhorses in the study of physics beyond the SM. Albeit attractive as toy models due to their largely trivial gauge structure, scalar singlet extensions do feature a rich phenomenology that may provide comprehensive solutions to a number of problems plaguing the SM (cf. Ref. [194–196]). One of their greatest assets are their non-trivial phase transition dynamics, which have prompted ample research in the field of EWBG (see *e.g.* Refs. [146, 148, 197, 198]). Consequently, the EW sphaleron in singlet scalar extensions has garnered much attention over the years, and its behaviour has been well studied at the zero and critical temperatures (cf. Refs. [145, 156, 199, 200]). In this work, the sphaleron decoupling condition will be revisited by taking advantage of a comparatively recent software development such as `CosmoTransitions`, which permits to reevaluate the condition at the nucleation temperature. A similar framework was implemented for a simplified study of the sphaleron in Ref. [155]. The present analysis generalizes these procedures to the full one-loop thermal effective potential.

11.1 The model

The addition of a real-valued EW gauge singlet to the Lagrangian in Eq. (2.2) defines

$$\mathcal{L}_{\text{EW}}^{\text{rSM}} \stackrel{\text{def}}{=} \mathcal{L}_{\text{kin}}^{\text{SM}} + \mathcal{L}_{\text{Yuk}}^{\text{SM}} + (\partial_\mu s)(\partial^\mu s) - V_{\text{eff}}(\Phi, s), \quad (11.1)$$

with the Higgs doublet in unitary gauge [145]

$$\Phi = \begin{pmatrix} \phi^+ \\ (h + i\phi)/\sqrt{2} \end{pmatrix} \quad (11.2)$$

and the real scalar singlet field s . The elements $\mathcal{L}_{\text{kin}}^{\text{SM}}$ and $\mathcal{L}_{\text{Yuk}}^{\text{SM}}$ in Eq. (11.1) cover the SM kinetic and Yukawa terms as introduced in Chapter 2, whereas the third

term represents the kinetic contribution of the singlet. The interactions of the new field with the SM content are mediated by the Higgs sector via portal couplings in the effective potential V_{eff} . At tree-level, it is given by

$$V_{\text{tree}}(\Phi, s) = -\mu^2 \Phi^\dagger \Phi + \lambda (\Phi^\dagger \Phi)^2 + \frac{a_1}{2} \Phi^\dagger \Phi s + \frac{a_2}{2} \Phi^\dagger \Phi s^2 + \frac{b_2}{2} s^2 + \frac{b_3}{3} s^3 + \frac{b_4}{4} s^4, \quad (11.3)$$

where the standard notation from Refs. [155, 194, 197] for the couplings is followed: the a_i describe couplings for Higgs-singlet mixing terms, the b_i all remaining singlet self-couplings. The model will be assumed to possess two field degrees of freedom: the dynamic Higgs field that attains the VEV in the symmetry broken phase, *i.e.* $\langle h \rangle = v$, and the new scalar, which acquires a VEV as $\langle s \rangle = v_s$. In terms of h and s , the tree-level potential is given by

$$V_{\text{tree}}(h, s) = -\frac{1}{2} \mu^2 h^2 + \frac{1}{4} \lambda h^4 + \frac{a_1}{4} h^2 s + \frac{a_2}{4} h^2 s^2 + \frac{b_2}{2} s^2 + \frac{b_3}{3} s^3 + \frac{b_4}{4} s^4. \quad (11.4)$$

The potential in (11.3) is the most general, renormalizable potential up to an additional tadpole term $b_1 s$. The model can be shown to be equivalent under both formulations, as the tadpole term can be sourced by a constant shift of the singlet field [197]. Ultimately, such a change of field coordinates has no effect on the physics and is merely a convenience which will not be followed in the coming analysis. Finally, it is pointed out that a subclass of \mathbb{Z}_2 -symmetric models occurs for vanishing a_1 and b_3 .

11.2 Construction of the effective potential

11.2.1 Zero-temperature, field-dependent masses

Scalar singlet extensions of the EW sector generically inherit the SM fermion and gauge boson masses. Consequently, the fermion mass squares are

$$m_f^2(h, s) = \frac{y_f^2}{2} h^2. \quad (11.5)$$

For the sake of consistency with Chapter 10, only the top quark t will be accounted for. The squared masses of the gauge bosons W^\pm and Z in turn are

$$m_W^2(h, s) = \frac{g_2^2}{4} h^2 \quad m_Z^2(h, s) = \frac{g_1^2 + g_2^2}{4} h^2. \quad (11.6)$$

The scalar singlet field becomes present in the Higgs-singlet mass matrix

$$\begin{aligned} \mathcal{M}_s^2(h, s) &= \begin{pmatrix} m_{hh}^2 & m_{hs}^2 \\ m_{sh}^2 & m_{ss}^2 \end{pmatrix} \\ &= \begin{pmatrix} 3\lambda h^2 - \mu^2 + \frac{1}{2}a_1 s + \frac{1}{2}a_2 s^2 & \frac{1}{2}a_1 h + a_2 h s \\ \frac{1}{2}a_1 h + a_2 h s & \frac{1}{2}a_2 h^2 + 3b_4 s^2 + 2b_3 s + b_2 \end{pmatrix}. \end{aligned} \quad (11.7)$$

The matrix (11.7) can be recast as a diagonal matrix with the two mass square eigenvalues $m_{h_1}^2$, $m_{h_2}^2$, indicated explicitly in Appendix B. These eigenvalues correspond to states in a mass basis defined by

$$h_1 = \cos(\alpha) h + \sin(\alpha) s \quad h_2 = -\sin(\alpha) h + \cos(\alpha) s. \quad (11.8)$$

The Higgs-singlet mixing angle α is defined by (194)

$$\tan(\alpha) = \frac{\rho}{1 + \sqrt{1 + \rho^2}} \quad \text{with} \quad \rho \stackrel{\text{def}}{=} \frac{m_{hs}^2}{m_{hh}^2 - m_{ss}^2}. \quad (11.9)$$

Throughout this analysis, h_1 is assumed to be the predominantly Higgs-like eigenstate while h_2 is treated as singlet-like. Finally, the field-dependent mass squares of the Goldstone bosons are

$$m_\phi^2(h, s) = \lambda h^2 - \mu^2 + \frac{a_1}{2} s + \frac{a_2}{2} s^2. \quad (11.10)$$

11.2.2 Counterterm potential

The counterterm potential

$$V_{\text{CT}}(h, s) = -\frac{1}{2}\delta\mu^2 h^2 + \frac{1}{4}\delta\lambda h^4 + \frac{\delta a_1}{4} h^2 s + \frac{\delta a_2}{4} h^2 s^2 + \frac{\delta b_2}{2} s^2 + \frac{\delta b_3}{3} s^3 + \frac{\delta b_4}{4} s^4 \quad (11.11)$$

is introduced in order to complete the renormalization of all seven couplings appearing in Eq. (11.4). The relations

$$\left. \frac{\partial V_{\text{CT}}(h, s)}{\partial h} \right|_{\text{vev}} \stackrel{!}{=} - \left. \frac{\partial \tilde{V}_{\text{CW}}(h, s)}{\partial h} \right|_{\text{vev}} \quad \left. \frac{\partial V_{\text{CT}}(h, s)}{\partial s} \right|_{\text{vev}} \stackrel{!}{=} - \left. \frac{\partial \tilde{V}_{\text{CW}}(h, s)}{\partial s} \right|_{\text{vev}} \quad (11.12)$$

$$\left. \frac{\partial^2 V_{\text{CT}}(h, s)}{\partial h^2} \right|_{\text{vev}} \stackrel{!}{=} - \left. \frac{\partial^2 \tilde{V}_{\text{CW}}(h, s)}{\partial h^2} \right|_{\text{vev}} \quad \left. \frac{\partial^2 V_{\text{CT}}(h, s)}{\partial s^2} \right|_{\text{vev}} \stackrel{!}{=} - \left. \frac{\partial^2 \tilde{V}_{\text{CW}}(h, s)}{\partial s^2} \right|_{\text{vev}} \quad (11.13)$$

$$\left. \frac{\partial^2 V_{\text{CT}}(h, s)}{\partial h \partial s} \right|_{\text{vev}} \stackrel{!}{=} - \left. \frac{\partial^2 \tilde{V}_{\text{CW}}(h, s)}{\partial h \partial s} \right|_{\text{vev}} \quad (11.14)$$

make sure the tree-level minima and masses remain intact at zero temperature after applying the CW corrections. The remaining free coefficients can be exhausted by further requiring

$$\left. \frac{\partial^3 V_{\text{CT}}(h, s)}{\partial s^3} \right|_{\text{vev}} \stackrel{!}{=} - \left. \frac{\partial^3 \tilde{V}_{\text{CW}}(h, s)}{\partial s^3} \right|_{\text{vev}} \quad \left. \frac{\partial^4 V_{\text{CT}}(h, s)}{\partial s^4} \right|_{\text{vev}} \stackrel{!}{=} - \left. \frac{\partial^4 \tilde{V}_{\text{CW}}(h, s)}{\partial s^4} \right|_{\text{vev}} . \quad (11.15)$$

Two clarifications are in order. Firstly, the subclass of \mathbb{Z}_2 -symmetric models requires the truncation of V_{CT} to those terms which satisfy the symmetry. With two fewer coefficients, two of the renormalization conditions need to be dropped in turn. Secondly, the third and fourth order derivatives in the conditions (11.15) prevent a consistent treatment of the Goldstone divergences at the VEV in line with Chapter 10. Following Ref. [144], the Goldstone modes were instead omitted altogether in the renormalization conditions. As the reference points out and was confirmed during setup, this procedure merely amounts to a new, self-consistent set of renormalization conditions with negligible effects on the potential altogether.

11.2.3 Thermal mass corrections

The thermal Debye masses of the Higgs-singlet system emerge as eigenvalues of the thermal mass matrix

$$\tilde{\mathcal{M}}_s^2(h, s, T) = \mathcal{M}_s^2(h, s) + \Pi(T). \quad (11.16)$$

The matrix $\Pi(T)$ corrects each component of \mathcal{M}_s^2 as [144]

$$\Pi_{hh}(T) = \left(\frac{3}{2} g_1^2 + \frac{9}{2} g_2^2 + 6 y_t^2 + 12 \lambda + a_2 \right) \frac{T^2}{24} \quad (11.17)$$

$$\Pi_{ss}(T) = (4 a_2 + 6 b_4) \frac{T^2}{24} \quad (11.18)$$

$$\Pi_{hs}(T) = \Pi_{sh}(T) \approx 0. \quad (11.19)$$

The Goldstone bosons each obtain a correction

$$\Pi_\phi(T) = \Pi_{hh}(T) \quad (11.20)$$

which can be added to their zero-temperature mass term. Finally, the gauge boson modes are corrected by [100]

$$\Pi_{W^\pm}^{\mathcal{L}}(T) = \Pi_{W^3}^{\mathcal{L}}(T) = \frac{11}{6}g_2^2T^2 \quad \Pi_{W^\pm}^{\mathcal{T}}(T) = \Pi_{W^3}^{\mathcal{T}}(T) = 0 \quad (11.21)$$

$$\Pi_B^{\mathcal{L}}(T) = \frac{11}{6}g_1^2T^2 \quad \Pi_B^{\mathcal{T}}(T) = 0. \quad (11.22)$$

This gives [167]

$$\tilde{m}_{W_{\mathcal{L}}^\pm}^2(h, s, T) = \frac{g_2^2}{4}h^2 + \frac{11}{6}g_2^2T^2 \quad (11.23)$$

for the longitudinal W boson modes. The thermal mass squares of the longitudinal Z and γ boson modes are [160]

$$\tilde{m}_{Z_{\mathcal{L}}, \gamma_{\mathcal{L}}}^2(h, s, T) = \frac{1}{8}(g_1^2 + g_2^2)h^2 + (g_1^2 + g_2^2)T^2 \pm \Delta \quad (11.24)$$

with

$$\Delta^2 = \frac{1}{64}(g_1^2 + g_2^2)(h^2 + 8T^2)^2 - g_1^2g_2^2T^2(h^2 + 4T^2). \quad (11.25)$$

The standard truncated full dressing procedure of Eq. (8.11) will be followed again, better supported by the employed `CosmoTransitions` implementation. The full thermal effective potential is thus

$$V_{\text{eff}}(h, s; T) = V_{\text{tree}}(h, s) + V_{\text{CW}}(h, s) + V_{\text{CT}}(h, s) + V_1^{\text{th}}(h, s; T). \quad (11.26)$$

11.3 Constraints on the model parameters

The parameter constraints used in this work rely on two previous studies of the EWPhT and its phenomenology in the rSM carried out in Refs. [194, 197], as well as on a general scrutiny of rSM phenomenology at the LHC provided by Ref. [201]. To the knowledge of the author, these references best capture the state-of-the-art parameter constraints on real singlet scalar extensions and were therefore used as guidelines. An overview of the theoretical and experimental bounds that have been employed is provided hereinafter.

11.3.1 Theoretical constraints

Vacuum stability and reparametrization of the potential

The present day EW vacuum with a Higgs VEV of $v \approx 246$ GeV needs to be recovered at tree-level (and, more generally, at zero temperature). In effect, this means

imposing

$$\left. \frac{\partial V_{\text{tree}}(h, s)}{\partial h} \right|_{\text{vev}} = \left. \frac{\partial V_{\text{tree}}(h, s)}{\partial s} \right|_{\text{vev}} = 0. \quad (11.27)$$

These conditions permit to eliminate μ^2 and b_2 altogether from the potential, as they require that [197]

$$\mu^2 = \lambda v^2 + \frac{1}{2} v_s (a_1 + a_2 v_s) \quad (11.28)$$

$$b_2 = -\frac{1}{4v_s} (v^2(a_1 + 2a_2 v_s) + 4v_s^2(b_3 + b_4 v_s)). \quad (11.29)$$

Minimization further calls for a positive definite Hessian matrix [11.7] evaluated at $(h, s) = (v, v_s)$. This allows to recast three further couplings in terms of more convenient physical parameters as [197]

$$\lambda = \frac{m_{h_1}^2 \cos^2(\alpha) + m_{h_2}^2 \sin^2(\alpha)}{2v^2} \quad (11.30)$$

$$a_1 = \frac{2v_s}{v^2} \left[2v_s^2 \left(2b_4 + \frac{b_3}{v_s} \right) - m_{h_1}^2 - m_{h_2}^2 + \cos(2\alpha)(m_{h_1}^2 - m_{h_2}^2) \right] \quad (11.31)$$

$$a_2 = -\frac{1}{2v^2 v_s} \left[(m_{h_1}^2 - m_{h_2}^2)(2v_s \cos(2\alpha) - v \sin(2\alpha)) + 4b_3 v_s^2 - 2v_s(m_{h_1}^2 + m_{h_2}^2 - 4b_4 v_s^2) \right]. \quad (11.32)$$

Effectively, the set of free parameters $\{\mu^2, \lambda, a_1, a_2, b_2, b_3, b_4\}$ can be replaced by $\{m_{h_1}, v, m_{h_2}, v_s, \alpha, b_3, b_4\}$ with fixed values for $v \approx 246$ GeV and $m_{h_1} \approx 125$ GeV (see *e.g.* Ref. [197]). Finally, the theory is assumed to be stable at the EW vacuum. Therefore, one needs to make sure the EW minimum is indeed the lowest one should the potential possess a plurality of minima at zero temperature.

Boundedness

The potential will be required to be bounded from below. In practice, the quartic terms dominate the potential towards large field values along the axes h and s ; therefore, the couplings λ and b_4 need to be positive. Moreover, in order to extend boundedness to all directions, a_2 also needs to be constrained. In summary, the requirements for boundedness read [194]

$$\lambda, b_4 > 0; \quad a_2 \geq -2\sqrt{\lambda b_4}. \quad (11.33)$$

Perturbativity of the couplings

The quartic couplings λ , a_2 and b_4 are required to satisfy [196, 201]

$$|\lambda|, |a_2|, |b_4| \leq 4\pi. \quad (11.34)$$

Perturbative unitarity

Perturbative unitarity is imposed on the S matrix for all $2 \rightarrow 2$ processes involving scalars and longitudinal gauge bosons. All of its eigenvalues will be required to satisfy [197, 202]

$$|w_i| \leq 8\pi. \quad (11.35)$$

Details on the S matrix can be recovered in Appendix I.

11.3.2 Experimental constraints

Higgs signal strength, W boson mass and EW precision tests

SM couplings to the $SU(2)$ -like state h_1 will be suppressed by the mixing (11.8) by a factor of $\cos(\alpha)$, while they will scale with $(-\sin(\alpha))$ for the singlet-like state h_2 [197]. It follows that a number of EW observables are sensitive to the value of α , and therefore, a series of experimental results constrain the available parameter space (Fig. 11.1). Most notably, Higgs signal rates place a mass-independent upper limit $|\sin \alpha| < 0.33 - 0.36$ at 95% confidence level [147, 197, 201].

In principle, deviations from EW observables parametrized by the Peskin-Takeuchi parameters need to be kept at bay. However, as can be seen in Fig. 11.1 and was pointed out in more general terms in Ref. [197], the effects of these constraints are largely sub-leading and can be safely ignored. Lastly, in the high m_{h_2} scenario^I, measurements of the W boson mass are significantly more restrictive than the Higgs signal rates [203]. As the calculated W boson mass needs to agree with experimental results, model-dependent one-loop corrections need to be suppressed, which sets even tighter bounds on α (Fig. 11.1). The figure allows to tentatively implement these constraints for a fixed v/v_s ; however, a strict and general treatment requires

^IRoughly defined by $m_{h_2} \gtrsim 2m_{h_1}$.

to follow the prescriptions of Ref. [203]. This was deemed beyond the scope of this work and left for future studies.

Altogether, taking advantage of the reparametrization of the model, parameter selection took place in terms of the more convenient set of quantities $\{m_{h_2}, v_s, \alpha, b_3, b_4\}$. The ranges in question, showcased in Table 11.1, correspond to a combination of bounds set by Refs. [194, 197]. All parameter sets underwent the checks described in this section. For the verification of the theoretical constraints, as well as for later uses throughout the analysis, the sets were reexpressed in terms of the original couplings.

Table 11.1: Parameter space used throughout this chapter, on the basis of Refs. [194, 197]. The upper limits on the dimensionful constants very roughly keep the analysis within EW scale, while the bound on b_4 lies well within the bounds of perturbativity.

Parameter space				
v_s [GeV]	m_{h_2} [GeV]	α	b_3 [GeV]	b_4
[0.01, 1000]	[260, 1000]	[-0.35, 0.35]	[-1000, 1000]	[0.001, 5]

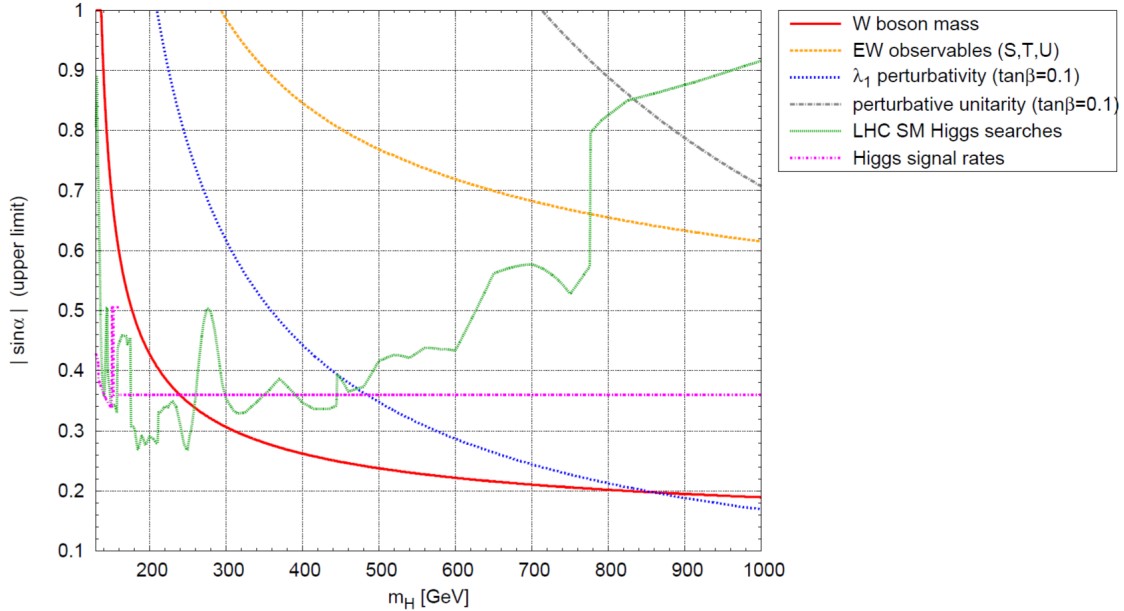


Figure 11.1: Upper limits on $|\sin(\alpha)|$ as a function of the mass parameter m_{h_2} (here, m_H) for a fixed value of $\beta = v/v_s$. As noted in the main text, present constraints on account of Higgs signal rate searches are slightly more stringent than in this figure, *i.e.* $|\sin(\alpha)| < 0.33$ [147, 197]. Figure taken from Ref. [201], which summarizes the results of Refs. [204–207].

11.4 Construction of the electroweak sphaleron

The derivation of the EW sphaleron follows the principles of Chapters [5](#) and [10](#).

The underlying energy functional is [145](#), [156](#)

$$\mathcal{E}[W_\mu^a, \Phi, s] = \int d^3x \left[\frac{1}{4} W_{ij}^a W^{aij} + (\mathcal{D}_i \Phi)^\dagger (\mathcal{D}^i \Phi) + \frac{1}{2} \partial_\mu s \partial^\mu s + \Delta V_{\text{eff}}^T(\Phi, s) \right], \quad (11.36)$$

with [155](#), [156](#)

$$\Delta V_{\text{eff}}^T(\Phi, s) \stackrel{\text{def}}{=} V_{\text{eff}}(\Phi, s, T) - V_{\text{eff}}(\Phi, s, T)|_{\text{vev}} \quad (11.37)$$

ensuring its evaluation with respect to the absolute vacuum at temperature T . The

ansatz of spherically symmetric fields is given by [145](#), [155](#)

$$\Phi(\xi, \theta, \phi; \mu) = h(\xi) \Phi^\infty(\theta, \phi; \mu) + (1 - h(\xi)) \frac{v}{\sqrt{2}} \begin{pmatrix} 0 \\ e^{-i\mu} \cos \mu \end{pmatrix} \quad (11.38)$$

$$s(\xi, \theta, \phi; \mu) = v_s l(\xi) \quad (11.39)$$

$$W_\xi(\xi, \theta, \phi; \mu) = 0 \quad (11.40)$$

$$W_\theta(\xi, \theta, \phi; \mu) = f(\xi) W_\theta^\infty(\theta, \phi; \mu) \quad (11.41)$$

$$W_\phi(\xi, \theta, \phi; \mu) = f(\xi) W_\phi^\infty(\theta, \phi; \mu), \quad (11.42)$$

with the loop parameter $\mu \in [0, \pi]$, the temperature-dependent VEVs $v = v(T)$, $v_s = v_s(T)$ and a dimensionless radial coordinate

$$\xi \stackrel{\text{def}}{=} g_2 r \Omega. \quad (11.43)$$

As pointed out by Refs. [153](#), [156](#), Ω merely rescales the radial coordinate and can be any parameter of mass dimension one, *e.g.* v , v_s or $\sqrt{v^2 + v_s^2}$. Furthermore, the missing loop parameter in Eq. [11.39](#) is noted, which ties in with the singlet scalar partaking trivially in the gauge structure of the theory. Evaluation of the ansatz at $\mu = \pi/2$ maximizes the energy along the loop, delivering the functional

$$\begin{aligned} \mathcal{E}[f, h, l] = & \frac{4\pi\Omega}{g_2} \int_0^\infty d\xi \left\{ 4 \left(\frac{df}{d\xi} \right)^2 + \frac{8}{\xi^2} f^2 (1-f)^2 + \frac{1}{2} \frac{v^2}{\Omega^2} \xi^2 \left(\frac{dh}{d\xi} \right)^2 \right. \\ & \left. + \frac{v^2}{\Omega^2} h^2 (1-f)^2 + \frac{1}{2} \frac{v_s^2}{\Omega^2} \xi^2 \left(\frac{dl}{d\xi} \right)^2 + \frac{\xi^2}{g_2^2 \Omega^4} \Delta V_{\text{eff}}^T(h, l) \right\}. \quad (11.44) \end{aligned}$$

As follows from Eq. [11.37](#), the quantity

$$\Delta V_{\text{eff}}^T(h, l) = V_{\text{eff}}(v h, v_s l, T) - V_{\text{eff}}(v, v_s, T) \quad (11.45)$$

takes care of evaluating the sphaleron energy (11.44) with respect to the absolute vacuum energy of the state (v, v_s) . Resting on the requirements for the existence of the sphaleron presented in Chapter 5, the radial functions need to satisfy

$$\lim_{\xi \rightarrow 0} f(\xi) = 0 \quad \lim_{\xi \rightarrow 0} h(\xi) = 0 \quad \lim_{\xi \rightarrow 0} l'(\xi) = 0 \quad (11.46)$$

$$\lim_{\xi \rightarrow \infty} f(\xi) = 1 \quad \lim_{\xi \rightarrow \infty} h(\xi) = 1 \quad \lim_{\xi \rightarrow \infty} l(\xi) = 1. \quad (11.47)$$

As shown in Ref. [156], the Neumann boundary condition on l at the origin is non-trivial but ultimately the only reasonable one ensuring the finiteness of \mathcal{E} . The Euler-Lagrange equations which result from Eq. (11.44) are

$$\xi^2 \frac{\partial^2 f}{\partial \xi^2} = 2f(1-f)(1-2f) - \frac{1}{4} \frac{v^2}{\Omega^2} \xi^2 h^2 (1-f) \quad (11.48)$$

$$\frac{\partial}{\partial \xi} \left(\xi^2 \frac{\partial h}{\partial \xi} \right) = 2h(1-f)^2 + \frac{\xi^2}{g_2^2 v^2 \Omega^2} \frac{\partial}{\partial h} \Delta V_{\text{eff}}^T(h, l) \quad (11.49)$$

$$\frac{\partial}{\partial \xi} \left(\xi^2 \frac{\partial l}{\partial \xi} \right) = \frac{\xi^2}{g_2^2 v_s^2 \Omega^2} \frac{\partial}{\partial l} \Delta V_{\text{eff}}^T(h, l). \quad (11.50)$$

The sphaleron energy is calculated via Eq. (11.44) with the solutions obtained for Eqs. (11.48) – (11.50). Unlike previous analyses of the model and in line with Chapter 10, this work also considers the $U(1)$ corrections to the energy. Given the gauge structure of the theory, these can be accounted for by applying the SM expression in Eq. (5.22).

11.5 Investigation of the decoupling criteria

11.5.1 Selection of benchmark points

A few tentative scans within the ranges of Table 11.1 allowed to identify the predominant phase transition trends in the general rSM scenario. In line with the findings of Ref. [197], it was found that one-step phase transitions dominate parameter space. While second-order phase transitions make up sizeable portions thereof, they do not provide the appropriate conditions for EWBG and were not pursued here.

A point of general importance concerns the non-restoration behaviour of the singlet, *i.e.* its acquisition of a non-zero VEV, at high temperatures in the FOPhTs recovered. This phenomenology was studied by Refs. [156, 208] and *a priori* generalizes the high temperature restoration patterns presented in Ref. [145]. Ultimately,

in absence of additional symmetry requirements (such as a \mathbb{Z}_2 -symmetry), one of the singlet VEVs is necessarily rendered unphysical by the shift symmetry addressed in Section [11.1](#). What remains physical, however, are any jumps in the field value at phase transitions. To this aim, it will be useful to define the quantity

$$\Delta v_s \stackrel{\text{def}}{=} \sqrt{(v_s - v_{s,\text{sym}})^2}, \quad (11.51)$$

with $v_{s,\text{sym}}$ the singlet VEV in the EW symmetric phase at the moment of the phase transition. Altogether, two parameter points satisfying the characteristics outlined above were singled out in Table [11.2](#) for further analysis.

Finally, it is pointed out that, whereas no two-step phase transitions were found in the coarse scans carried out for the general scenario, they constitute a dominant pattern in \mathbb{Z}_2 -symmetric models (cf. Ref. [\[148\]](#)). As their analysis requires a targeted approach, two-step phase transitions are left for future work. Nonetheless, one parameter point is kept for future reference in Table [11.2](#).

Table 11.2: BMPs used for a first characterization of the sphaleron.

	BMP1	BMP2	BMP3
PT pattern	1-step	1-step	2-step
Restoration	No	No	Yes
v_s [GeV]	222.37	98.71	150.00
m_{h_2} [GeV]	476.05	275.67	540.00
α	0.07	-0.29	0.10
b_3 [GeV]	-413.81	-376.95	0
b_4	1.64	2.78	4.66
\mathcal{E}_0 [GeV]	8901.18	8994.32	9331.26
T_{n_1} [GeV]	124.19	105.75	126.29
v_{n_1} [GeV]	197.60	205.75	76.09
v_{s,n_1} [GeV]	219.95	108.23	0
$v_{s,\text{sym}}$ [GeV]	187.35	159.18	0
$\mathcal{E}_{n,1}$ [GeV]	6451.09	7078.58	2673.43
T_{n_2} [GeV]	-	-	95.02
v_{n_2} [GeV]	-	-	225.14
v_{s,n_2} [GeV]	-	-	139.21
$\mathcal{E}_{n,2}$ [GeV]	-	-	8379.76

11.5.2 Characterization of the sphaleron

Following the procedures of Chapter 10, the solutions to (11.48) – (11.50) for the BMPs of Table 11.2 provided first insights into the sphaleron. As the plots in Fig. 11.2 show, the profiles of the Higgs and gauge fields at zero- and nucleation-temperature bear a strong resemblance to their SM and IDM counterparts (cf. Figs. 5.3 and 10.1). This stands in contrast to the diverse physiognomy exhibited by the singlet field profiles, which has no distinctive effect on the remaining fields other than a slight impact on their convergence rates. The origin of this contrasting phenomenology in the profiles was ultimately not pursued in this work; nonetheless, it could be worth studying any links to the overall modest contribution of the singlet field on the sphaleron energy suggested in Ref. 156.

The evolution of the sphaleron energy \mathcal{E} and its relation to the various VEVs after symmetry breaking is provided in Fig. 11.3 for BMPs 1 and 2. Firstly, as the left-hand side plots showcase, the temperature-dependent evolution of \mathcal{E} (in red)

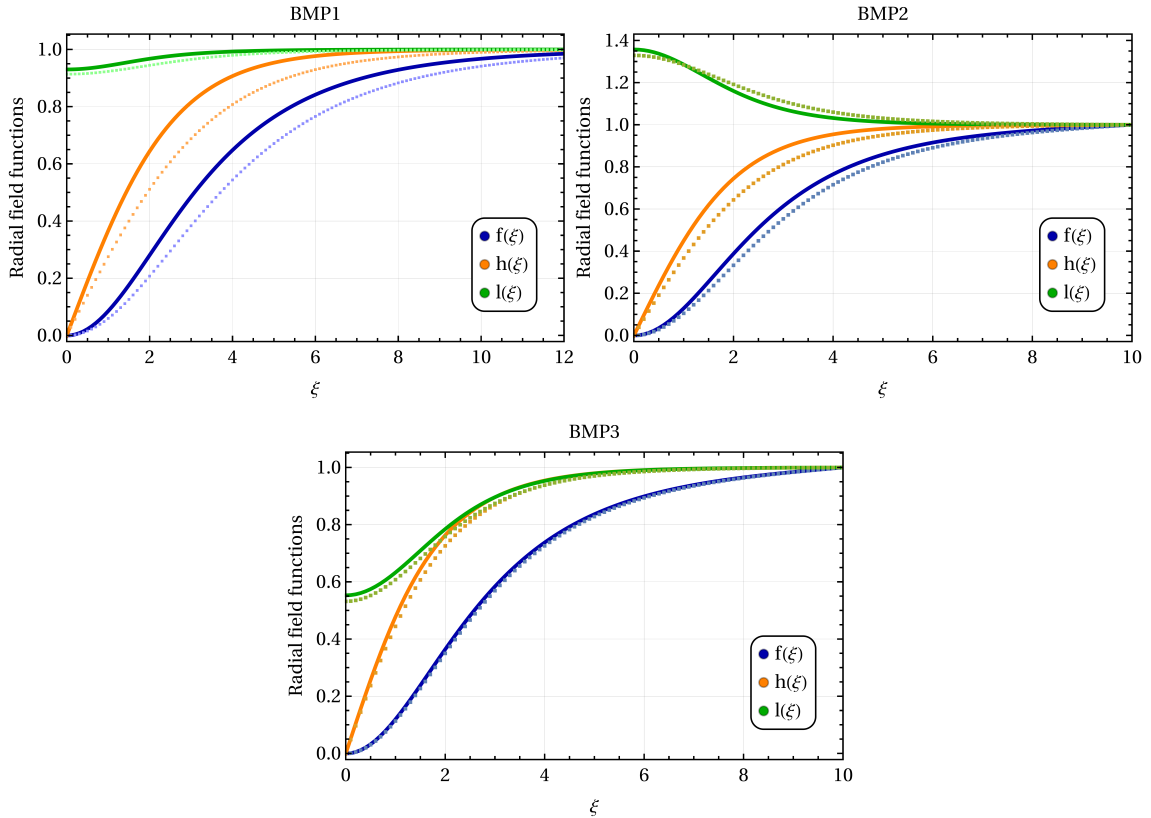


Figure 11.2: Exemplary sphaleron curves for the BMPs in Table 11.2. The continuous lines correspond to the zero-temperature solutions of (11.48)–(11.50), whereas the dotted lines were obtained at the respective nucleation temperatures (in the case of BMP3, at $T_{n,2}$).

largely tallies with the behaviour of the Higgs VEV $v(T)$ (in orange). The right-hand side plots of the figure cement this observation: whereas the proportionality between both quantities is not exact, the approximate scaling law (7.11) between $v(T)$ and \mathcal{E} is tangible for these BMPs.

Secondly, the figure further addresses an aspect of singlet models which has garnered attention in the past, namely the nature of the scaling – if extant at all – between the energy and the remaining singlet and full VEVs of the model [156]. Relying on the figure, the existence of a simple, universal scaling law for the singlet VEV (in green) appears dubious, as opposite scaling with \mathcal{E} between both rows is displayed. Yet, this picture changes drastically when considering the quantity Δv_s and the corresponding full VEV $\sqrt{v^2 + \Delta v_s^2}$, *i.e.* the quantities accounting for the jump of the VEV at the phase transition. The scaling behaviour of the full VEV in particular begs the question of whether it could be a more suitable candidate for a criterion on SFOPhTs than the Higgs VEV. Ultimately, Ref. [156] settled this

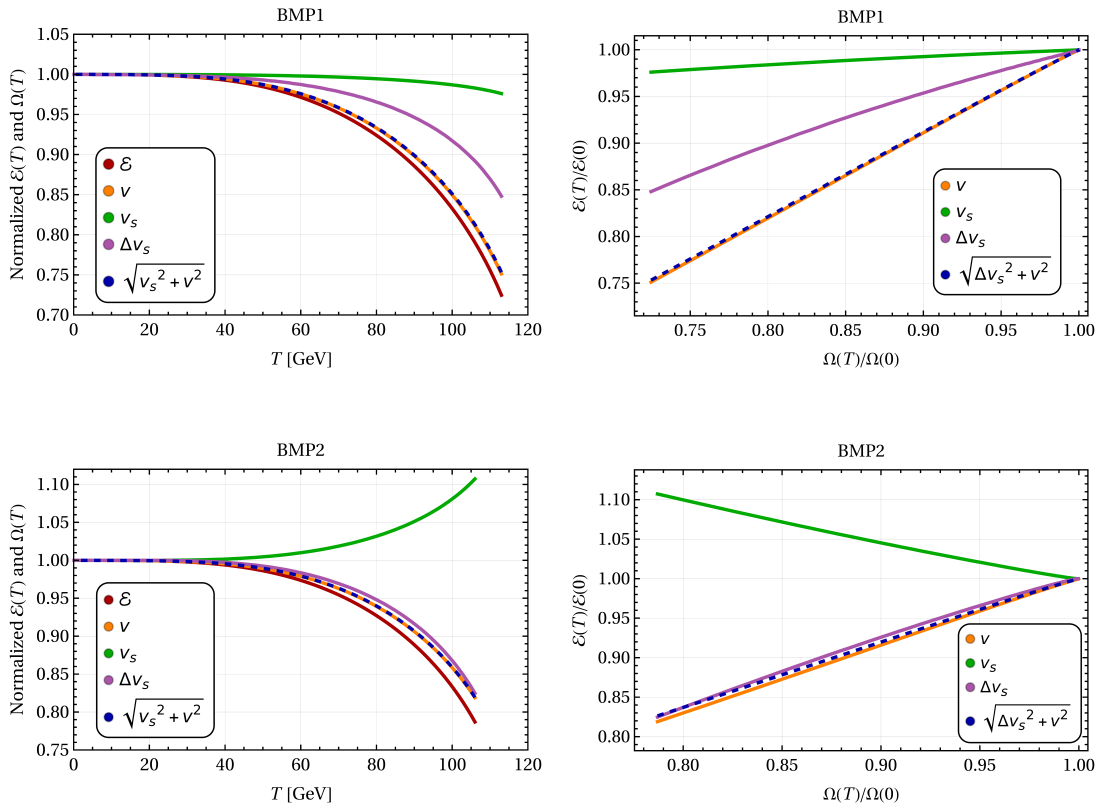


Figure 11.3: LEFT: Temperature-dependent evolution of the normalized VEVs $\Omega(T)$ and sphaleron energies for BMP1 and BMP2 from Table 11.2. The plots cover the range between zero temperature and the nucleation temperature T_n . RIGHT: Scaling of $\mathcal{E}(T)$ with the different VEVs.

question in a targeted numerical study. Such a criterion inadequately captures the decoupling of sphalerons. Instead, the standard condition (7.14) on the Higgs VEV alone remains appropriate. This sets the stage for its reassessment.

11.5.3 SFOPhTs and sphaleron decoupling in the rSM

The reliability of the standard ξ_n -criterion was counter-checked at nucleation in line with the final procedure of Chapter 10. To this aim, the parameter space showcased by Table 11.1 was sampled randomly. For the 500 sample parameter sets surviving all constraints and featuring a first-order nucleation into the correct EW minimum, the quantities ξ_n , $\mathcal{E}(T_n)$ and the corresponding σ_n were calculated. It is found that for low enough v_n and ξ_n , the finiteness of the mesh domain compromises the numerical integrity of the sphaleron solutions in the setup employed (see Appendix H.1.3). These effects set in slightly below $\xi_n \lesssim 0.8$ and thus motivate the cutoffs in the following figures. Fig. 11.4 conveys the linear nature of the scaling between $\mathcal{E}(T_n)/T_n$ and ξ_n . It determines the dominant behaviour of σ_n in relation to ξ_n , in turn displayed in Fig. 11.5. The color gradient in Fig. 11.4 further showcases $\mathcal{E}(T_n)$ for the remaining 338 points, which were found in the range 3.5 – 10 TeV, whereas the color gradient in Fig. 11.5 does the same for the normalized v_n .

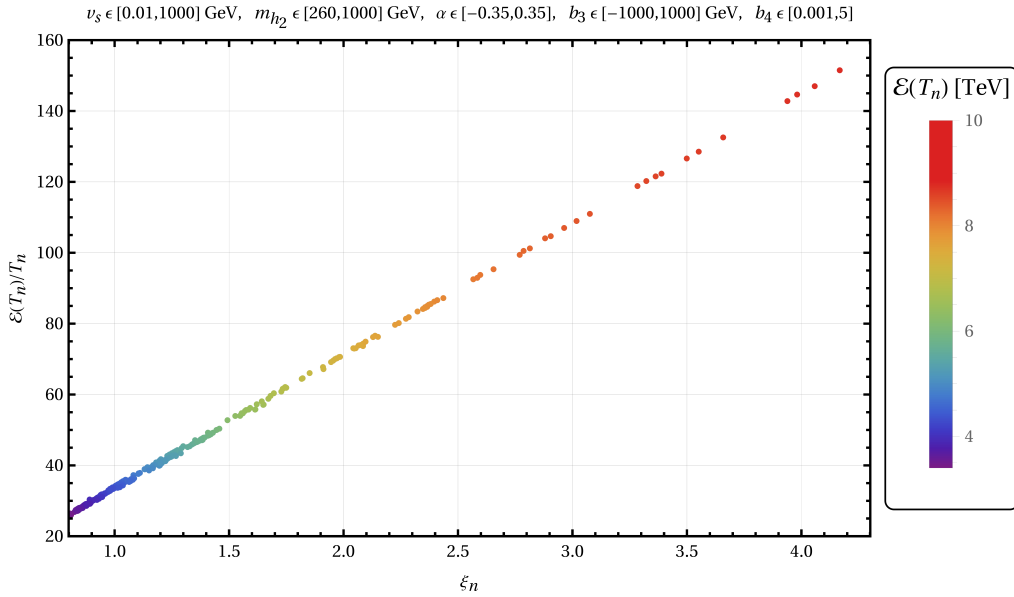


Figure 11.4: Scaling of $\mathcal{E}(T_n)/T_n$ with ξ_n in the rSM for a sample of 338 random points within the ranges of Table 11.1.

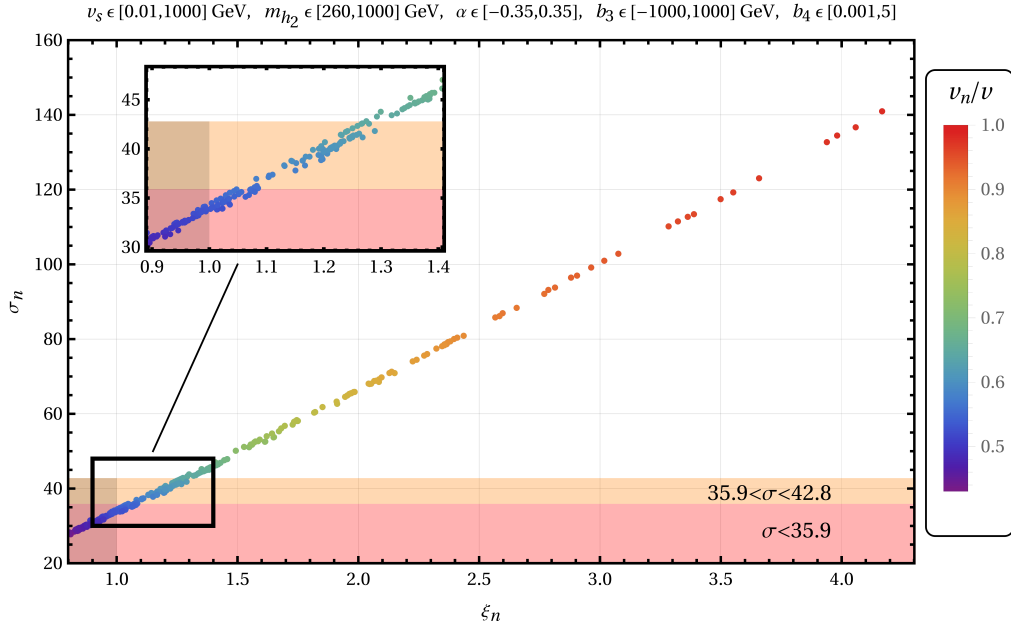


Figure 11.5: Comparison of the criteria on σ_n and ξ_n in the rSM for a sample of 338 random points within the space of parameters of Table [11.1](#). The shaded region in the lower left corner is excluded by the σ -criterion and the canonical ξ -criterion.

Yet again, the modesty of the canonical ξ_n -criterion is hinted at by Fig. [11.5](#), as the curve outlined by the sample data crosses the bounds on σ beyond the shaded region marking $\xi_n \lesssim 1$. The magnification suggests a shift of the ξ -criterion to

$$\xi_n \gtrsim (1.05 - 1.30), \quad (11.52)$$

which tallies with the results obtained for the IDM and can largely be traced back to the similar – yet not identical – scaling of Figs. [10.7](#) and [11.4](#). Furthermore, and as encountered in the IDM, one notes the potential for phase transitions with large $\mathcal{E}(T_n)$ and v_n , which are linked to $\xi_n \gg 1$. Whereas the figures suggest a relative scarcity of such phase transitions as compared to transitions with $\xi_n \sim 1$, this could ultimately be an unwanted artifact of the sample selection or the small sample size and thus requires caution. Finally, in contrast to the minimal dispersion in the results of the previous chapter, it is worth noting the width of the data sample in Fig. [11.4](#). This width is of approximately $0.05\xi_n$ for the slices of constant σ_n most densely populated and thus marks a stark contrast to the $\sigma - \xi$ plot obtained for the IDM. The higher dispersion in the data sample of the rSM can be tentatively traced back to, at least, two sources which ultimately stress the differences between the models and approaches followed throughout this work. First of all, the transitions considered

in the rSM are much richer on a structural level, as they feature a full range of active fields, as opposed to the inertness of Φ_2 in the IDM. The active interplay of *all* fields entails an enhanced impact of *all* model parameters. In particular, none of the tree-level terms in $\Delta V_{\text{eff}}^T(h, l)$, featured in Eqs. (11.48) – (11.50), vanishes on account of field inertness. Whether this opens the door to non-trivial effects of individual sampling parameters and combinations thereof on $\mathcal{E}(T)$, which could then affect the relation between ξ and σ at a subdominant level, could be an interesting direction to follow. Ultimately, this chapter has not delved into the dependence of the phase transition strength on individual parameters, which would be a good place to start.

Secondly, sampling parameters in the rSM were reaped from a parameter space for the most part much less constrained than in the former analysis, and then screened in a much more lenient manner (see Section 11.3.2). Although recent bounds were employed for both models, parameter selection and screening in the rSM took into account fewer experimental constraints and ultimately did not specifically aim for DM candidates. The relative freedom in the choice of model parameters may in turn have induced larger regions of parameter space seemingly available for SFOPhTs. Within these, an increased heterogeneity in the relation of ξ and $\mathcal{E}(T)$ may be possible, which would feed the dispersion in plots of $\sigma - \xi$ as Fig. 11.4. These arguments are not entirely speculative and tie in with the results of Ref. [156], which display a suggestive dispersion behaviour in similar plots of $\mathcal{E}(T_c)/T_c$ against ξ_c .

On the whole, the results obtained in this chapter largely agree with similar results available in the literature. Refs. [145, 156] both suggest the bounds $\xi_c \gtrsim (1.1 - 1.2)$, obtained under an assumption that roughly translates into the upper bound on σ [91]. They are well covered by the central region of the bounds (11.52) for ξ_n . However, the present results raise the more stringent bound by 0.05–0.10 units of ξ_n , the latter uncertainty on account of the sample dispersion. Whereas these results constitute at best a small improvement on the state of the art, they independently confirm the increased severity of the decoupling criterion in the rSM with respect to the order-of-magnitude estimate $\xi \gtrsim 1$. Nonetheless, when considered in the context of the most generous estimates (7.15) of the ξ -criterion available in the SM, the results (11.52) cannot be unequivocally attributed to the effects of new physics.

Ultimately, it is yet again the uncertainty in the sphaleron fluctuation determinant κ which marks the limits of this work. At any rate, these results and their comparison to equivalent literature values serve to gauge the performance of the framework, *i.e.* of the approach and the computational implementations, on which the novel results of Chapter [10](#) rest.

Chapter 12

Conclusion and outlook

At a crossroads between cosmology, elementary particle physics and QFT, the BAU is one of the great mysteries of modern physics. EWBG constitutes one of the most promising candidate solutions to the puzzle, yet explicitly invokes physics beyond the SM for a successful realization. In the present work, the mechanism has been approached in two models with extended scalar sectors in order to shed light on one of its premises: a strong first-order EW phase transition.

Part [I](#) of this work provided a comprehensive review of EWBG which laid down the formal groundwork and dissected two of its fundamental ingredients: the EW sphaleron and a SFOPhT at EWSB. An outline of the mechanism of EWBG was presented, on the basis of which the standard order-of-estimate criterion $\xi \stackrel{\text{def}}{=} v(T)/T \gtrsim 1$ for a SFOPhT was justified. Part [II](#) addressed the methods employed throughout the later analyses. First, it introduced the general elements of the one-loop thermal effective potential used to track the phase transition in the candidate models. Then, two computational methods were presented on which the entirety of the later analyses came to rest. Special emphasis was placed on a general-purpose relaxation algorithm which was successfully embedded into the framework of this project. Finally, Part [III](#) reassessed the criterion $\xi \gtrsim 1$ for two extensions of the SM, the IDM and the rSM, which were set up taking into account state-of-the-art theoretical and experimental constraints. Special attention was paid to the temperature scheme used in the evaluation of the criterion. After a comprehensive comparison, the scheme showing an improved consistency with the phenomenology of phase transitions was chosen. This ensured that the largely independent criterion of bubble nucleation, crucial and yet widely neglected in similar studies, was appropriately taken into account.

The central results obtained in Part [III](#) call for a conservative assessment. On

the one hand side, both models suggest an updated criterion of $\xi_n \gtrsim (1.05 - 1.30)$ within the uncertainties of the framework. This renders the condition up to 30% more severe than the plain order-of-magnitude estimate $\xi \gtrsim 1$ that pervades the literature. On the other hand side, these results largely come to agree with the more nuanced SM estimates of the criterion presented in Chapter 7, as well as with the outcomes of comparable analyses available for the rSM and general 2HDM scenarios. All things considered, this work strengthens current state-of-the-art results via an independent comprehensive assessment. The impact of the new physics and the improved temperature scheme on the criterion for a SFOPhT can be deemed modest, yet not entirely negligible. Moreover, the novel results obtained for the IDM constitute a first benchmark of the ξ -criterion in the model to the best knowledge of the author.

In addition to the central results, this work sheds light on the separate issue of bubble nucleation. Its importance reaches far beyond the scope of this work, successful nucleation being a phenomenological imperative of BSM scenarios. In the context of EWBG, the nucleation criterion acts on top of the Sakharov conditions and should be viewed as both a vital requirement and a valuable asset. As the comparative case study in the IDM featured in this work shows, significant portions of parameter space can be excluded altogether on this criterion alone, thus helping to better delineate the regions available for a SFOPhT.

Finally, it should be interesting to acquire a sound grasp of the complex multi-step transitions largely eluded in this work. Such studies might, for instance, constitute a first step towards ambitious reevaluations of multi-Higgs doublet models seasoned with additional singlet scalars with regards to their potential for EWBG.

In the grand scheme of things, EWBG relies on far more than a strong first-order EW phase transition. Within the realm of the phase transition alone, additional conditions on the bubble and particle dynamics constitute further defining factors. Moreover, the independent matter of CP violation needs to be accounted for. None of the models considered in this work inherently feature additional CP violation, meaning that new sources have to be added *ad-hoc*. Ultimately, an elegant solution to the puzzle of the BAU could lie in a comprehensive model which addresses the entirety of the Sakharov criteria. Within EWBG, the ever-present requirement for

thermal off-equilibrium will necessarily call for a SFOPhT. The results presented in this thesis, based on state-of-the-art methods, constitute a stepping stone towards more comprehensive models which could hold the key to the BAU.

Bibliography

- [1] J. Ellis. “Beyond the Standard Model for hillwalkers”. In: *arXiv preprint hep-ph/9812235* (1998).
- [2] J. Ellis. “Limits of the Standard Model”. In: *arXiv preprint hep-ph/0211168* (2002).
- [3] F. Zwicky. “Die Rotverschiebung von extragalaktischen Nebeln”. In: *Helvetica Physica Acta* 6 (1933), pp. 110–127.
- [4] G. Bertone *et al.* “Particle dark matter: evidence, candidates and constraints”. In: *Physics Reports* 405.5-6 (Jan. 2005), pp. 279–390. ISSN: 0370-1573. DOI: [10.1016/j.physrep.2004.08.031](https://doi.org/10.1016/j.physrep.2004.08.031). URL: <http://dx.doi.org/10.1016/j.physrep.2004.08.031>.
- [5] D. Wu. “A brief introduction to the strong CP problem”. In: *Zeitschrift für Naturforschung A* 52.1-2 (1997), pp. 179–182.
- [6] H. Georgi. “The flavor problem”. In: *Physics Letters B* 169.2-3 (1986), pp. 231–233.
- [7] M. C. González-García and Y. Nir. “Neutrino masses and mixing: evidence and implications”. In: *Reviews of Modern Physics* 75.2 (Mar. 2003), pp. 345–402. ISSN: 1539-0756. DOI: [10.1103/revmodphys.75.345](https://doi.org/10.1103/revmodphys.75.345). URL: <http://dx.doi.org/10.1103/RevModPhys.75.345>.
- [8] K. M. Heeger. “Evidence for neutrino mass: a decade of discovery”. In: *SEE-SAW* 25 (Apr. 2005). DOI: [10.1142/9789812702210_0005](https://doi.org/10.1142/9789812702210_0005). URL: http://dx.doi.org/10.1142/9789812702210_0005.
- [9] B. Schulz. *Review on the quantization of gravity*. 2014. arXiv: [1409.7977](https://arxiv.org/abs/1409.7977) [[gr-qc](https://arxiv.org/abs/1409.7977)].

- [10] A. Ashtekar and E. Bianchi. “A short review of loop quantum gravity”. In: *Reports on Progress in Physics* 84.4 (Mar. 2021), p. 042001. ISSN: 1361-6633. DOI: [10.1088/1361-6633/abed91](https://doi.org/10.1088/1361-6633/abed91). URL: <http://dx.doi.org/10.1088/1361-6633/abed91>.
- [11] C. Csáki and P. Tanedo. “Beyond the Standard Model”. In: *arXiv preprint arXiv:1602.04228* (2016).
- [12] F. Jegerlehner. “The hierarchy problem of the electroweak Standard Model revisited”. In: *arXiv preprint arXiv:1305.6652* (2013).
- [13] G. Bhattacharyya. “Hierarchy problem and BSM physics”. In: *Pramana* 89.4 (2017), pp. 1–3.
- [14] P. A. M. Dirac. “A theory of electrons and protons”. In: *Proceedings of the Royal Society of London. Series A, Containing papers of a mathematical and physical character* 126.801 (1930), pp. 360–365.
- [15] P. A. M. Dirac. “Quantised singularities in the electromagnetic field”. In: *Proceedings of the Royal Society of London. Series A, Containing Papers of a Mathematical and Physical Character* 133.821 (1931), pp. 60–72.
- [16] H. Primakoff and S. P. Rosen. “Baryon number and lepton number conservation laws”. In: *Annual Review of Nuclear and Particle Science* 31.1 (1981), pp. 145–192.
- [17] G. Steigman. “Observational tests of antimatter cosmologies”. In: *Annual review of astronomy and astrophysics* 14.1 (1976), pp. 339–372.
- [18] W. Hu *et al.* “Cosmic Microwave Background Anisotropies”. In: *Annual Review of Astronomy and Astrophysics* 40.1 (Sept. 2002), pp. 171–216. ISSN: 1545-4282. DOI: [10.1146/annurev.astro.40.060401.093926](https://doi.org/10.1146/annurev.astro.40.060401.093926). URL: <http://dx.doi.org/10.1146/annurev.astro.40.060401.093926>.
- [19] D. N. Spergel *et al.* “First-year Wilkinson Microwave Anisotropy Probe (WMAP)* observations: determination of cosmological parameters”. In: *The Astrophysical Journal Supplement Series* 148.1 (2003), p. 175.
- [20] S. Eidelman *et al.* “Review of particle physics”. In: *Physics letters B* 592.1-4 (2004), pp. 1–5.

- [21] R. H. Cyburt. “Primordial nucleosynthesis for the new cosmology: Determining uncertainties and examining concordance”. In: *Physical Review D* 70.2 (July 2004). ISSN: 1550-2368. DOI: [10.1103/PhysRevD.70.023505](https://doi.org/10.1103/PhysRevD.70.023505). URL: <http://dx.doi.org/10.1103/PhysRevD.70.023505>.
- [22] P. A. R. Ade *et al.* “Planck 2013 results. XVI. Cosmological parameters”. In: *Astronomy & Astrophysics* 571 (2014), A16.
- [23] R. Battiston. “Astro-particle physics with the Alpha Magnetic Spectrometer (AMS)”. In: *Ital. Phys. Soc. Conf. Ser. 57: Frontier Objects in Astrophysics and Particle Physics*. 1997, p. 543.
- [24] R. Battiston. “The Alpha Magnetic Spectrometer (AMS): search for antimatter and dark matter on the International Space Station”. In: *Nuclear Physics B - Proceedings Supplements* 65.1-3 (June 1998), pp. 19–26. ISSN: 0920-5632. DOI: [10.1016/S0920-5632\(97\)00970-5](https://doi.org/10.1016/S0920-5632(97)00970-5). URL: [http://dx.doi.org/10.1016/S0920-5632\(97\)00970-5](http://dx.doi.org/10.1016/S0920-5632(97)00970-5).
- [25] M. Aguilar *et al.* “The Alpha Magnetic Spectrometer (AMS) on the International Space Station: Part I—Results from the test flight on the space shuttle”. In: *Physics Reports* 366.6 (2002), pp. 331–405.
- [26] M. Aguilar *et al.* “The Alpha Magnetic Spectrometer (AMS) on the international space station: Part II—Results from the first seven years”. In: *Physics reports* (2020).
- [27] G. A. White. *A pedagogical introduction to electroweak baryogenesis*. Morgan & Claypool Publishers, 2016.
- [28] E. W. Kolb and M. S. Turner. “The early universe”. In: *Nature* 294.5841 (1981), pp. 521–526.
- [29] S. Davidson *et al.* “Leptogenesis”. In: *Physics Reports* 466.4-5 (2008), pp. 105–177.
- [30] K. Fuyuto. “Electroweak Baryogenesis”. In: *Electroweak Baryogenesis and Its Phenomenology*. Springer, 2018, pp. 9–33.
- [31] A. D. Sakharov. “Pis'ma Zh. Eksp. Teor. Fiz. 5 (1967) 32”. In: *JETP Lett* 5 (1967), p. 24.

- [32] V. A. Kuzmin. “CP violation and baryon asymmetry of the universe”. In: *Pisma Zh. Eksp. Teor. Fiz.* 12 (1970), pp. 335–337.
- [33] A. Y. Ignatiev *et al.* “Universal CP-noninvariant superweak interaction and bayron asymmetry of the universe”. In: *Physics Letters B* 76.4 (1978), pp. 436–438.
- [34] M. Yoshimura. “Unified gauge theories and the baryon number of the universe”. In: *Physical Review Letters* 41.5 (1978), p. 281.
- [35] M. Yoshimura. “Physics Review Letters 41, 281”. In: *Phys. Rev. Lett* 42 (1978), p. 746.
- [36] E. P. Wigner. “Symmetry and conservation laws”. In: *Proceedings of the National Academy of Sciences of the United States of America* 51.5 (1964), p. 956.
- [37] E. C. G. Stueckelberg. “Forces of interaction in electrodynamics and in the field theory of nuclear forces.(Parts II and III)”. In: *Helv. Phys. Acta* 11 (1938), pp. 299–328.
- [38] L. Bergamasco *et al.* “An experimental lower limit on the proton lifetime”. In: *Lettere al Nuovo Cimento (1971-1985)* 11.14 (1974), pp. 636–638.
- [39] E. N. Alekseev *et al.* “Lower limit on the proton lifetime according to data from the Baksan underground scintillation”. In: *JETP Lett* 33.12 (1981).
- [40] P. Langacker. “The Present Status of Proton Decay and Baryon Number Non-conservation”. In: *Weak and Electromagnetic Interactions in Nuclei*. Springer, 1986, pp. 879–890.
- [41] A. Takenaka *et al.* “Search for proton decay via $p \rightarrow e^+ + \pi^0$ and $p \rightarrow \mu^+ + \pi^0$ with an enlarged fiducial volume in Super-Kamiokande I-IV”. In: *Physical Review D* 102.11 (2020), p. 112011.
- [42] K. S. Babu *et al.* “Baryon number violation”. In: *arXiv preprint arXiv:1311.5285* (2013).
- [43] S. Chatrchyan *et al.* “Search for baryon number violation in top-quark decays”. In: *Physics Letters B* 731 (2014), pp. 173–196.

- [44] S. Dimopoulos and L. J. Hall. “Baryogenesis at the MeV era”. In: *Physics Letters B* 196.2 (1987), pp. 135–141.
- [45] A. Dannenberg and L. J. Hall. “Baryogenesis at the weak phase transition”. In: *Physics Letters B* 198.3 (1987), pp. 411–415.
- [46] V. A. Kuzmin *et al.* “On anomalous electroweak baryon-number non-conservation in the early universe”. In: *Physics Letters B* 155.1-2 (1985), pp. 36–42.
- [47] M. E. Shaposhnikov. “Possible appearance of the baryon asymmetry of the universe in an electroweak theory”. In: *Soviet Journal of Experimental and Theoretical Physics Letters* 44 (1986), p. 465.
- [48] L. McLerran. “Can the observed baryon asymmetry be produced at the electroweak phase transition?” In: *Physical review letters* 62.10 (1989), p. 1075.
- [49] N. Turok and J. Zadrozny. “Dynamical generation of baryons at the electroweak transition”. In: *Physical Review Letters* 65.19 (1990), p. 2331.
- [50] A. G. Cohen *et al.* “Weak scale baryogenesis”. In: *Physics Letters B* 245.3-4 (1990), pp. 561–564.
- [51] A. G. Cohen *et al.* “Spontaneous baryogenesis at the weak phase transition”. In: *Physics Letters B* 263.1 (1991), pp. 86–92.
- [52] M. Dine *et al.* “Comments on the electroweak phase transition”. In: *Physics Letters B* 283.3-4 (1992), pp. 319–325.
- [53] P. Huet and A. E. Nelson. “CP violation and electroweak baryogenesis in extensions of the standard model”. In: *Physics Letters B* 355.1-2 (1995), pp. 229–235.
- [54] N. S. Manton. “Topology in the Weinberg-Salam theory”. In: *Physical Review D* 28.8 (1983), p. 2019.
- [55] F. R. Klinkhamer and N. S. Manton. “A saddle-point solution in the Weinberg-Salam theory”. In: *Physical Review D* 30.10 (1984), p. 2212.
- [56] P. Arnold and L. McLerran. “Sphalerons, small fluctuations, and baryon-number violation in electroweak theory”. In: *Physical Review D* 36.2 (1987), p. 581.

- [57] M. B. Gavela *et al.* “Standard Model CP-violation and baryon asymmetry”. In: *Modern Physics Letters A* 09.09 (Mar. 1994), pp. 795–809. ISSN: 1793-6632. DOI: [10.1142/S0217732394000629](https://doi.org/10.1142/S0217732394000629). URL: <http://dx.doi.org/10.1142/S0217732394000629>.
- [58] M. B. Gavela *et al.* “Standard Model CP-violation and baryon asymmetry (II). Finite temperature”. In: *Nuclear Physics B* 430.2 (Nov. 1994), pp. 382–426. ISSN: 0550-3213. DOI: [10.1016/0550-3213\(94\)00410-2](https://doi.org/10.1016/0550-3213(94)00410-2). URL: [http://dx.doi.org/10.1016/0550-3213\(94\)00410-2](http://dx.doi.org/10.1016/0550-3213(94)00410-2).
- [59] P. Huet and E. Sather. “Electroweak baryogenesis and Standard Model CP violation”. In: *Physical Review D* 51.2 (Jan. 1995), pp. 379–394. ISSN: 0556-2821. DOI: [10.1103/physrevd.51.379](https://doi.org/10.1103/physrevd.51.379). URL: <http://dx.doi.org/10.1103/PhysRevD.51.379>.
- [60] T. Konstandin *et al.* “Axial currents from CKM matrix CP violation and electroweak baryogenesis”. In: *Nuclear Physics B* 679.1-2 (Feb. 2004), pp. 246–260. ISSN: 0550-3213. DOI: [10.1016/j.nuclphysb.2003.11.037](https://doi.org/10.1016/j.nuclphysb.2003.11.037). URL: <http://dx.doi.org/10.1016/j.nuclphysb.2003.11.037>.
- [61] K. Kajantie *et al.* “Is there a hot electroweak phase transition at $m_H \gtrsim m_W$?” In: *Physical Review Letters* 77.14 (1996), p. 2887.
- [62] K. Kajantie *et al.* “The Electroweak phase transition in a magnetic field”. In: *Nuclear Physics B* 544.1-2 (1999), pp. 357–373.
- [63] F. Csikor *et al.* “End point of the hot electroweak phase transition”. In: *Physical Review Letters* 82.1 (1999), p. 21.
- [64] Y. Aoki *et al.* “The end point of the first-order phase transition of the SU(2) gauge-Higgs model on a 4-dimensional isotropic lattice”. In: *Physical Review D* 60.1 (1999), p. 013001.
- [65] ALEPH collaboration *et al.* “Search for the Standard Model Higgs Boson at LEP”. In: *Physics Letters B* 565 (2003), pp. 61–75.
- [66] N. S. Manton. “The inevitability of sphalerons in field theory”. In: *Philosophical Transactions of the Royal Society A* 377.2161 (2019), p. 20180327.

- [67] M. Kamionkowski *et al.* “Gravitational radiation from first-order phase transitions”. In: *Physical Review D* 49.6 (1994), p. 2837.
- [68] C. Caprini *et al.* “Science with the space-based interferometer eLISA. II: Gravitational waves from cosmological phase transitions”. In: *Journal of cosmology and astroparticle physics* 2016.04 (2016), p. 001.
- [69] H. Kudoh *et al.* “Detecting a gravitational-wave background with next-generation space interferometers”. In: *Physical Review D* 73.6 (2006), p. 064006.
- [70] B. P. Abbott *et al.* “Observation of gravitational waves from a binary black hole merger”. In: *Physical review letters* 116.6 (2016), p. 061102.
- [71] Y. Cui *et al.* “Cosmic archaeology with gravitational waves from cosmic strings”. In: *Physical Review D* 97.12 (2018), p. 123505.
- [72] L. Graziani *et al.* “Cosmic archaeology with massive stellar black hole binaries”. In: *Monthly Notices of the Royal Astronomical Society: Letters* 495.1 (2020), pp. L81–L85.
- [73] ME Shaposhnikov. “Baryon asymmetry of the universe in standard electroweak theory”. In: *Nuclear Physics B* 287 (1987), pp. 757–775.
- [74] J. M. Cline. “Baryogenesis”. In: *arXiv preprint hep-ph/0609145* (2006).
- [75] A. Riotto. “Theories of baryogenesis”. In: *Proceedings, Summer School in High-energy physics and cosmology: Trieste, Italy* (1998), pp. 326–436.
- [76] S. L. Glashow. “Partial-symmetries of weak interactions”. In: *Nuclear physics* 22.4 (1961), pp. 579–588.
- [77] S. Weinberg. “A model of leptons”. In: *Physical review letters* 19.21 (1967), p. 1264.
- [78] A. Salam. “Weak and electromagnetic interactions”. In: *Selected Papers Of Abdus Salam: (With Commentary)*. World Scientific, 1994, pp. 244–254.
- [79] M. E. Peskin and D. V. Schroeder. *An Introduction to Quantum Field Theory*. 1995.
- [80] M. D. Schwartz. *Quantum field theory and the Standard Model*. Cambridge University Press, 2014.

- [81] G. Kane. *Modern Elementary Particle Physics: The Fundamental Particles and Forces, Updated Edition*. 1993.
- [82] F. Englert and R. Brout. “Broken symmetry and the mass of gauge vector mesons”. In: *Physical Review Letters* 13.9 (1964), p. 321.
- [83] P. W. Higgs. “Broken symmetries and the masses of gauge bosons”. In: *Physical Review Letters* 13.16 (1964), p. 508.
- [84] G. S. Guralnik *et al.* “Global conservation laws and massless particles”. In: *Physical Review Letters* 13.20 (1964), p. 585.
- [85] M. Thomson. *Modern particle physics*. Cambridge University Press, 2013.
- [86] N. Cabibbo. “Unitary symmetry and leptonic decays”. In: *Physical Review Letters* 10.12 (1963), p. 531.
- [87] M. Kobayashi and T. Maskawa. “CP-violation in the renormalizable theory of weak interaction”. In: *Progress of theoretical physics* 49.2 (1973), pp. 652–657.
- [88] J. H. Christenson *et al.* “Evidence for the 2π Decay of the K^0 Meson”. In: *Physical Review Letters* 13.4 (1964), p. 138.
- [89] A. Alavi-Harati *et al.* “Observation of Direct CP Violation in $K_{S,L} \rightarrow \pi\pi$ Decays”. In: *Physical Review Letters* 83.1 (July 1999), pp. 22–27. ISSN: 1079-7114. DOI: [10.1103/physrevlett.83.22](https://doi.org/10.1103/PhysRevLett.83.22). URL: <http://dx.doi.org/10.1103/PhysRevLett.83.22>.
- [90] V. Fanti *et al.* “A new measurement of direct CP violation in two pion decays of the neutral kaon”. In: *Physics Letters B* 465.1-4 (Oct. 1999), pp. 335–348. ISSN: 0370-2693. DOI: [10.1016/S0370-2693\(99\)01030-8](https://doi.org/10.1016/S0370-2693(99)01030-8). URL: [http://dx.doi.org/10.1016/S0370-2693\(99\)01030-8](http://dx.doi.org/10.1016/S0370-2693(99)01030-8).
- [91] M. Quirós. “Finite temperature field theory and phase transitions”. In: *Proceedings, Summer school in high-energy physics and cosmology: Trieste, Italy 1999* (1998), pp. 187–259.
- [92] S. Coleman and E. Weinberg. “Radiative corrections as the origin of spontaneous symmetry breaking”. In: *Physical Review D* 7.6 (1973), p. 1888.

- [93] S. Flörchinger and C. Wetterich. *Lectures on quantum field theory 2*. 2019.
URL: https://www.thphys.uni-heidelberg.de/~floerchinger/assets/pdfs/Quantum_field_theory_2_2019.pdf.
- [94] S. Flörchinger and C. Wetterich. *Lectures on quantum field theory 1*. 2018.
URL: https://www.thphys.uni-heidelberg.de/~floerchinger/assets/pdfs/Quantum_field_theory_1_20182019.pdf.
- [95] M. Laine and A. Vuorinen. “Basics of thermal field theory”. In: *Lect. Notes Phys* 925.1 (2016).
- [96] J. I. Kapusta and C. Gale. *Finite-Temperature Field Theory Principles and Applications*. 2006.
- [97] L. Dolan and R. Jackiw. “Symmetry behavior at finite temperature”. In: *Physical Review D* 9.12 (1974), p. 3320.
- [98] R. Jackiw. “Symmetry restoration at finite temperature”. In: *International Symposium on Mathematical Problems in Theoretical Physics*. Springer. 1975, pp. 319–325.
- [99] C. King and L. G. Yaffe. “Global symmetry restoration in high temperature Higgs theories”. In: *Communications in mathematical physics* 108.3 (1987), pp. 423–436.
- [100] M. E. Carrington. “Effective potential at finite temperature in the standard model”. In: *Physical Review D* 45.8 (1992), p. 2933.
- [101] S. L. Adler. “Axial-vector vertex in spinor electrodynamics”. In: *Physical Review* 177.5 (1969), p. 2426.
- [102] J. S. Bell and R. Jackiw. “A PCAC puzzle: $\pi_0 \rightarrow \gamma\gamma$ in the σ -model”. In: *Il Nuovo Cimento A (1965-1970)* 60.1 (1969), pp. 47–61.
- [103] G. ’t Hooft. “Symmetry breaking through Bell-Jackiw anomalies”. In: *Physical Review Letters* 37 (1976), pp. 8–11.
- [104] K. Fujikawa. “Path-integral measure for gauge-invariant fermion theories”. In: *Physical Review Letters* 42.18 (1979), p. 1195.
- [105] K. Fujikawa. “Evaluation of the chiral anomaly in gauge theories with γ_5 couplings”. In: *Physical Review D* 29.2 (1984), p. 285.

-
- [106] L. McLerran. “Anomalies, Sphalerons and Baryon Number Violation in Electroweak Theory”. In: *Acta Phys. Polon. B* 20 (1989), pp. 249–286.
- [107] H.-J. Borchers. “Über die Mannigfaltigkeit der interpolierenden Felder zu einer kausalen S-Matrix”. In: *Il Nuovo Cimento (1955-1965)* 15.5 (1960), pp. 784–794.
- [108] S. Kamefuchi *et al.* “Change of variables and equivalence theorems in quantum field theories”. In: *Selected Papers Of Abdus Salam: (With Commentary)*. World Scientific, 1994, pp. 103–123.
- [109] I. V. Tyutin. “Once again on the equivalence theorem”. In: *Physics of Atomic Nuclei* 65.1 (2002), pp. 194–202.
- [110] S. Weinberg. “The Quantum Theory of Fields vol 1 (Cambridge: Cambridge)”. In: (1995).
- [111] R. Jackiw and C. Rebbi. “Vacuum periodicity in a Yang-Mills quantum theory”. In: *Physical Review Letters* 37.3 (1976), p. 172.
- [112] C. G. Callan Jr. *et al.* “The structure of the gauge theory vacuum”. In: *Physics Letters B* 63.3 (1976), pp. 334–340.
- [113] A. M. Polyakov. “Quark confinement and topology of gauge theories”. In: *Nuclear Physics B* 120.3 (1977), pp. 429–458.
- [114] M. Shifman. *Advanced topics in quantum field theory: A lecture course*. Cambridge University Press, 2012.
- [115] N. S. Manton and P. Sutcliffe. *Topological solitons*. Cambridge University Press, 2004.
- [116] S. Skadhauge. “Sphalerons and Electroweak Baryogenesis”. PhD thesis. Copenhagen U., 1996.
- [117] K. Funakubo. *Lecture slides (intensive course at Nagoya University)*. June 2013.
- [118] T. Heldeweg. “Sphaleron solutions and their phenomenology in the electroweak theory”. MA thesis. 2018.
- [119] L. Carson *et al.* “Exact computation of the small-fluctuation determinant around a sphaleron”. In: *Physical Review D* 42.6 (1990), p. 2127.

- [120] G. D. Moore *et al.* “Chern-Simons number diffusion with hard thermal loops”. In: *Physical Review D* 58.4 (1998), p. 045001.
- [121] M. D’Onofrio *et al.* “Sphaleron rate in the minimal standard model”. In: *Physical review letters* 113.14 (2014), p. 141602.
- [122] X. Gan *et al.* “Electroweak sphaleron with dimension-six operators”. In: *Physical Review D* 96.11 (2017), p. 115018.
- [123] J. Baacke and S. Junker. “Quantum corrections to the electroweak sphaleron transition”. In: *Modern Physics Letters A* 8.30 (1993), pp. 2869–2874.
- [124] J. Baacke and S. Junker. “Quantum fluctuations around the electroweak sphaleron”. In: *Physical Review D* 49.4 (1994), p. 2055.
- [125] J. Baacke and S. Junker. “Quantum fluctuations of the electroweak sphaleron: Erratum and addendum”. In: *Physical Review D* 50.6 (1994), p. 4227.
- [126] A. I. Bochkarev and M. E. Shaposhnikov. “Electroweak production of baryon asymmetry and upper bounds on the Higgs and top masses”. In: *Modern Physics Letters A* 2.06 (1987), pp. 417–427.
- [127] S. Fabian. “Study of the Inert Doublet Model in the light of Dark Matter physics and Electroweak Phase Transition”. MA thesis. Ruprecht-Karls-Universität Heidelberg, 2020.
- [128] J. S. Langer. “Theory of the condensation point”. In: *Annals of Physics* 41.1 (1967), pp. 108–157. ISSN: 0003-4916. DOI: [https://doi.org/10.1016/0003-4916\(67\)90200-X](https://doi.org/10.1016/0003-4916(67)90200-X). URL: <https://www.sciencedirect.com/science/article/pii/000349166790200X>.
- [129] J. S. Langer. “Statistical theory of the decay of metastable states”. In: *Annals of Physics* 54.2 (1969), pp. 258–275.
- [130] D. V. Perepelitsa. *Path integrals in quantum mechanics*. 2018.
- [131] W. Ai. “Aspects of False Vacuum Decay”. PhD thesis. Technische Universität München, 2019.
- [132] S. Coleman. “Fate of the false vacuum: Semiclassical theory”. In: *Physical Review D* 15.10 (1977), p. 2929.

- [133] C. G. Callan Jr. and S. Coleman. “Fate of the false vacuum. II. First quantum corrections”. In: *Physical Review D* 16.6 (1977), p. 1762.
- [134] A. Andreassen *et al.* “Direct Approach to Quantum Tunneling”. In: *Physical Review Letters* 117.23 (Nov. 2016). ISSN: 1079-7114. DOI: [10.1103/PhysRevLett.117.231601](https://doi.org/10.1103/PhysRevLett.117.231601) URL: <http://dx.doi.org/10.1103/PhysRevLett.117.231601>.
- [135] A. Andreassen *et al.* “Precision decay rate calculations in quantum field theory”. In: *Physical Review D* 95.8 (2017), p. 085011.
- [136] A. D. Linde. “On the vacuum instability and the Higgs meson mass”. In: *Physics Letters B* 70.3 (1977), pp. 306–308.
- [137] A. D. Linde. “Fate of the false vacuum at finite temperature: theory and applications”. In: *Phys. Lett., B* 100.1 (1981), pp. 37–40.
- [138] A. D. Linde. “Decay of the false vacuum at finite temperature”. In: *Nuclear Physics B* 216.2 (1983), pp. 421–445.
- [139] S. M. Carroll. *Spacetime and geometry*. Cambridge University Press, 2019.
- [140] M. Dine *et al.* “Towards the theory of the electroweak phase transition”. In: *Physical Review D* 46.2 (1992), p. 550.
- [141] M. Breitbach. “Gravitational Waves from Cosmological Phase Transitions”. MA thesis. Johannes Gutenberg University Mainz, 2018.
- [142] K. Funakubo *et al.* “Phase transitions in the NMSSM”. In: *Progress of theoretical physics* 114.2 (2005), pp. 369–389.
- [143] C.-W. Chiang and E. Senaha. “Electroweak phase transitions in the secluded U (1) -extended MSSM”. In: *Journal of High Energy Physics* 2010.6 (2010), p. 30.
- [144] J. R. Espinosa *et al.* “Strong electroweak phase transitions in the Standard Model with a singlet”. In: *Nuclear Physics B* 854.3 (2012), pp. 592–630.
- [145] K. Fuyuto and E. Senaha. “Improved sphaleron decoupling condition and the Higgs coupling constants in the real singlet-extended Standard Model”. In: *Physical Review D* 90.1 (2014), p. 015015.

- [146] G. Kurup and M. Perelstein. “Dynamics of electroweak phase transition in singlet-scalar extension of the Standard Model”. In: *Physical Review D* 96.1 (2017), p. 015036.
- [147] M. Carena *et al.* “Probing the electroweak phase transition via enhanced di-Higgs boson production”. In: *Physical Review D* 97.9 (2018), p. 095032.
- [148] M. Carena *et al.* “Electroweak phase transition with spontaneous Z_2 -breaking”. In: *Journal of High Energy Physics* 2020.8 (2020), pp. 1–38.
- [149] S. Fabian *et al.* “Dark Matter and Nature of Electroweak Phase Transition with an Inert Doublet”. In: *arXiv preprint arXiv:2012.12847* (2020).
- [150] W. Su *et al.* “Strong first order electroweak phase transition in 2HDM confronting future Z & Higgs factories”. In: *Journal of High Energy Physics* 2021.4 (2021), pp. 1–37.
- [151] M. Joyce *et al.* “Non-local Electroweak Baryogenesis. Part I: Thin Wall Regime”. In: *Physical Review D* 53.6 (Mar. 1996), pp. 2930–2957. ISSN: 1089-4918. DOI: [10.1103/PhysRevD.53.2930](https://doi.org/10.1103/PhysRevD.53.2930). URL: <http://dx.doi.org/10.1103/PhysRevD.53.2930>.
- [152] M. Joyce *et al.* “Non-local Electroweak Baryogenesis. Part II: The Classical Regime”. In: *Physical Review D* 53.6 (Mar. 1996), pp. 2958–2980. ISSN: 1089-4918. DOI: [10.1103/PhysRevD.53.2958](https://doi.org/10.1103/PhysRevD.53.2958). URL: <http://dx.doi.org/10.1103/PhysRevD.53.2958>.
- [153] R. Zhou and L. Bian. “Baryon asymmetry and detectable gravitational waves from electroweak phase transition”. In: *arXiv preprint arXiv:2001.01237* (2020).
- [154] S. Braibant *et al.* “Sphalerons at finite temperature”. In: *International Journal of Modern Physics A* 8.31 (1993), pp. 5563–5574.
- [155] R. Zhou *et al.* “Connecting the electroweak sphaleron with gravitational waves”. In: *Physical Review D* 101.9 (2020), p. 091903.
- [156] A. Ahriche. “What is the criterion for a strong first order electroweak phase transition in singlet models?” In: *Physical Review D* 75.8 (2007), p. 083522.

- [157] H. H. Patel and M. J. Ramsey-Musolf. “Baryon washout, electroweak phase transition, and perturbation theory”. In: *Journal of High Energy Physics* 2011.7 (2011), p. 29.
- [158] S. Chatrchyan *et al.* “Observation of a new boson at a mass of 125 GeV with the CMS experiment at the LHC”. In: *Physics Letters B* 716.1 (2012), pp. 30–61.
- [159] F. Goertz. “Composite Higgs theory”. In: *Proceedings of An Alpine LHC Physics Summit — PoS(ALPS2018)* (Sept. 2018). DOI: [10.22323/1.330.0012](https://doi.org/10.22323/1.330.0012). URL: <http://dx.doi.org/10.22323/1.330.0012>.
- [160] J. Bernon *et al.* “A new insight into the phase transition in the early Universe with two Higgs doublets”. In: *Journal of High Energy Physics* 2018.5 (2018), pp. 1–43.
- [161] D. Curtin *et al.* “Thermal resummation and phase transitions”. In: *The European Physical Journal C* 78.9 (2018), pp. 1–29.
- [162] G. W. Anderson and L. J. Hall. “Electroweak phase transition and baryogenesis”. In: *Physical Review D* 45.8 (1992), p. 2685.
- [163] D. J. Gross *et al.* “QCD and instantons at finite temperature”. In: *Reviews of Modern Physics* 53.1 (1981), p. 43.
- [164] R. R. Parwani. “Resummation in a hot scalar field theory”. In: *Physical Review D* 45.12 (1992), p. 4695.
- [165] R. R. Parwani. “Erratum: Resummation in a hot scalar field theory”. In: *Physical Review D* 48.12 (1993), p. 5965.
- [166] C. Delaunay *et al.* “Dynamics of non-renormalizable electroweak symmetry breaking”. In: *Journal of High Energy Physics* 2008.04 (2008), p. 029.
- [167] P. Arnold and O. Espinosa. “Effective potential and first-order phase transitions: Beyond leading order”. In: *Physical Review D* 47.8 (1993), p. 3546.
- [168] C. Manuel. “Thermal gauge boson masses of the electroweak theory in the broken phase”. In: *Physical Review D* 58.1 (1998), p. 016001.
- [169] W. H. Press *et al.* *Numerical Recipes: Example Book: Fortran*. Cambridge Univ. P., 1985.

- [170] U. M. Ascher *et al.* *Numerical solution of boundary value problems for ordinary differential equations*. SIAM, 1995.
- [171] C. L. Wainwright. “CosmoTransitions: computing cosmological phase transition temperatures and bubble profiles with multiple fields”. In: *Computer Physics Communications* 183.9 (2012), pp. 2006–2013.
- [172] Y. Wang. *CosmoTransition_Z2SB*. https://gitlab.com/yikwang/cosmotransition_z2sb. Accessed: 26-03-2021.
- [173] N. Blinov. *CosmoTransition_Z2SB*. https://github.com/nblinov/ct_sm. Accessed: 26-03-2021.
- [174] N. Blinov *et al.* “The electroweak phase transition in the Inert Doublet Model”. In: *Journal of Cosmology and Astroparticle Physics* 2015.07 (July 2015), pp. 028–028. ISSN: 1475-7516. DOI: [10.1088/1475-7516/2015/07/028](https://doi.org/10.1088/1475-7516/2015/07/028). URL: <http://dx.doi.org/10.1088/1475-7516/2015/07/028>.
- [175] M. Bichsel. *Mathematica implementation of the Relaxation algorithm*. https://www.wiwi.uni-siegen.de/vwli/forschung/relaxation/relaxation_mat/mathematica_applications/relaxationdescription.txt?lang=de. Accessed: 20-03-2021.
- [176] T. Trimborn *et al.* “Multidimensional transitional dynamics: a simple numerical procedure”. In: *Macroeconomic Dynamics* 12.3 (2008), pp. 301–319.
- [177] S. Banerjee *et al.* “Relic density of dark matter in the inert doublet model beyond leading order for the low mass region: 1. Renormalisation and constraints”. In: *arXiv preprint arXiv:2101.02165* (2021).
- [178] S. Banerjee *et al.* *arXiv: Relic density of dark matter in the inert doublet model beyond leading order for the low mass region: 2. Co-annihilation*. Tech. rep. 2021.
- [179] S. Banerjee *et al.* “Relic density of dark matter in the inert doublet model beyond leading order for the low mass region: 3. Annihilation in 3-body final state”. In: *arXiv preprint arXiv:2101.02167* (2021).

- [180] S. Banerjee. “Relic density of dark matter in the inert doublet model beyond leading order for the low mass region: 4. The Higgs resonance region”. In: *arXiv preprint arXiv:2101.02170* (2021).
- [181] A. Belyaev *et al.* “Anatomy of the inert two-Higgs-doublet model in the light of the LHC and non-LHC dark matter searches”. In: *Physical Review D* 97.3 (2018), p. 035011.
- [182] J. M. Cline and P.-A. Lemieux. “Electroweak phase transition in two Higgs doublet models”. In: *Physical Review D* 55.6 (Mar. 1997), pp. 3873–3881. ISSN: 1089-4918. DOI: [10.1103/physrevd.55.3873](https://doi.org/10.1103/physrevd.55.3873). URL: <http://dx.doi.org/10.1103/PhysRevD.55.3873>.
- [183] J. M. Cline *et al.* “Electroweak baryogenesis in two Higgs doublet models and B meson anomalies”. In: *Journal of High Energy Physics* 2011.11 (Nov. 2011). ISSN: 1029-8479. DOI: [10.1007/jhep11\(2011\)089](https://doi.org/10.1007/jhep11(2011)089). URL: [http://dx.doi.org/10.1007/JHEP11\(2011\)089](http://dx.doi.org/10.1007/JHEP11(2011)089).
- [184] A. Ilnicka *et al.* “Inert doublet model in light of LHC Run I and astrophysical data”. In: *Physical Review D* 93.5 (Mar. 2016). ISSN: 2470-0029. DOI: [10.1103/physrevd.93.055026](https://doi.org/10.1103/physrevd.93.055026). URL: <http://dx.doi.org/10.1103/PhysRevD.93.055026>.
- [185] E. Lundström. “Inert doublet model and LEP II limits”. In: *Physical Review D* 79.3 (Feb. 2009). ISSN: 1550-2368. DOI: [10.1103/physrevd.79.035013](https://doi.org/10.1103/physrevd.79.035013). URL: <http://dx.doi.org/10.1103/PhysRevD.79.035013>.
- [186] A. Pierce and J. Thaler. “Natural Dark Matter from an unnatural Higgs boson and new colored particles at the TeV scale”. In: *Journal of High Energy Physics* 2007.08 (Aug. 2007), pp. 026–026. ISSN: 1029-8479. DOI: [10.1088/1126-6708/2007/08/026](https://doi.org/10.1088/1126-6708/2007/08/026). URL: <http://dx.doi.org/10.1088/1126-6708/2007/08/026>.
- [187] K. Fuyuto and E. Senaha. “Sphaleron and critical bubble in the scale invariant two Higgs doublet model”. In: *Physics Letters B* 747 (2015), pp. 152–157.
- [188] M. Tanabashi *et al.* “Status of Higgs Boson Physics”. In: *Physical Review D* 98 (2018), p. 030001.

- [189] M. Aaboud *et al.* “Combination of searches for invisible Higgs boson decays with the ATLAS experiment”. In: *Physical review letters* 122.23 (2019), p. 231801.
- [190] A. M. Sirunyan *et al.* “Search for invisible decays of a Higgs boson produced through vector boson fusion in proton-proton collisions at $s = 13$ TeV”. In: *Physics Letters B* 793 (2019), pp. 520–551.
- [191] M. Baak *et al.* “The global electroweak fit at NNLO and prospects for the LHC and ILC”. In: *The European Physical Journal C* 74.9 (2014), pp. 1–14.
- [192] M. E. Peskin and T. Takeuchi. “New constraint on a strongly interacting Higgs sector”. In: *Physical Review Letters* 65.8 (1990), p. 964.
- [193] B. Kastening. “Sphalerons in the two-doublet Higgs model”. In: *Physics Letters B* 266.3-4 (1991), pp. 413–418.
- [194] S. Profumo *et al.* “Singlet Higgs Phenomenology and the Electroweak Phase Transition”. In: *Journal of High Energy Physics* 2007.08 (2007), p. 010.
- [195] R. N. Lerner and J. McDonald. “Gauge singlet scalar as inflaton and thermal relic dark matter”. In: *Physical Review D* 80.12 (Dec. 2009). ISSN: 1550-2368. DOI: [10.1103/PhysRevD.80.123507](https://doi.org/10.1103/PhysRevD.80.123507). URL: <http://dx.doi.org/10.1103/PhysRevD.80.123507>.
- [196] M. Gonderinger *et al.* “Vacuum stability, perturbativity, and scalar singlet dark matter”. In: *Journal of High Energy Physics* 2010.1 (Jan. 2010). ISSN: 1029-8479. DOI: [10.1007/jhep01\(2010\)053](https://doi.org/10.1007/jhep01(2010)053). URL: [http://dx.doi.org/10.1007/JHEP01\(2010\)053](http://dx.doi.org/10.1007/JHEP01(2010)053).
- [197] A. Alves *et al.* “Collider and gravitational wave complementarity in exploring the singlet extension of the Standard Model”. In: *Journal of High Energy Physics* 2019.4 (2019), p. 52.
- [198] C.-Y. Chen *et al.* “Non-resonant collider signatures of a singlet-driven electroweak phase transition”. In: *Journal of High Energy Physics* 2017.8 (2017), pp. 1–49.
- [199] B. Kastening and X. Zhang. “Sphalerons in an SU(2) model with one Higgs doublet and one scalar singlet”. In: *Physical Review D* 45.10 (1992), p. 3884.

-
- [200] J. Choi. “Sphalerons in the Standard Model with a real Higgs singlet”. In: *Physics Letters B* 345.3 (1995), pp. 253–258.
- [201] T. Robens and T. Stefaniak. “LHC benchmark scenarios for the real Higgs singlet extension of the Standard Model”. In: *The European Physical Journal C* 76.5 (2016), pp. 1–12.
- [202] S. Kanemura and K. Yagyu. “Unitarity bound in the most general two Higgs doublet model”. In: *Physics Letters B* 751 (2015), pp. 289–296.
- [203] D. López-Val and T. Robens. “ Δr and the W-boson mass in the Singlet Extension of the Standard Model”. In: *Physical Review D* 90.11 (2014), p. 114018.
- [204] G. Chalons *et al.* “The Higgs Singlet Extension at LHC Run 2”. In: *arXiv preprint arXiv:1606.07793* (2016).
- [205] G. M. Pruna and T. Robens. “The Higgs Singlet Extension parameter space in the light of the LHC discovery”. In: *arXiv preprint arXiv:1303.1150* (2013).
- [206] T. Robens and T. Stefaniak. “Status of the Higgs Singlet Extension of the Standard Model after LHC run 1”. In: *The European Physical Journal C* 75.3 (2015), pp. 1–25.
- [207] T. Robens. “Investigating extended scalar sectors at current and future colliders”. In: *arXiv preprint arXiv:1908.10809* (2019).
- [208] J. Choi and R. R. Volkas. “Real Higgs singlet and the electroweak phase transition in the Standard Model”. In: *Physics Letters B* 317.3 (1993), pp. 385–391.
- [209] P. A. Zyla *et al.* (Particle Data Group). “Review of particle physics”. In: *Progress of Theoretical and Experimental Physics* 2020.8 (2020), p. 083C01.
- [210] I. Oda. “Conformal Higgs Gravity”. In: *arXiv preprint arXiv:1505.06760* (2015).
- [211] M. Dine *et al.* “Baryogenesis at the electroweak scale”. In: *Nuclear Physics B* 375.3 (1992), pp. 625–648.

- [212] A. Arhrib *et al.* “ $H \rightarrow \gamma\gamma$ in the Inert Higgs Doublet Model”. In: *Physical Review D* 85.9 (May 2012). ISSN: 1550-2368. DOI: [10.1103/physrevd.85.095021](https://doi.org/10.1103/physrevd.85.095021). URL: <http://dx.doi.org/10.1103/PhysRevD.85.095021>.
- [213] R. Barbieri *et al.* “Improved naturalness with a heavy Higgs boson: An alternative road to CERN LHC physics”. In: *Physical Review D* 74.1 (July 2006). ISSN: 1550-2368. DOI: [10.1103/physrevd.74.015007](https://doi.org/10.1103/physrevd.74.015007). URL: <http://dx.doi.org/10.1103/PhysRevD.74.015007>.

Appendix A

Units and conventions

The following conventions, values and constants are assumed throughout the entirety of the work.

Units and constants

Natural units are employed unless explicitly stated otherwise, *i.e.*

$$\hbar = c = 1 \tag{A.1}$$

for the reduced Planck constant \hbar , the speed of light c and the gravitational constant G .

Tensors, matrices and vectors

This work essentially assumes the conventions of Ref. [79] for the tensors and matrices typical of QFT. For example, the standard metric tensor in particle physics and QFT will be

$$\eta_{\mu\nu} = \eta^{\mu\nu} = \begin{pmatrix} 1 & 0 & 0 & 0 \\ 0 & -1 & 0 & 0 \\ 0 & 0 & -1 & 0 \\ 0 & 0 & 0 & -1 \end{pmatrix}. \tag{A.2}$$

Greek indices cover $\{0, 1, 2, 3\}$ or alternatively $\{t, x, y, z\}$. In certain instances, t will be replaced by the Euclidean $\tau = -it$; Greek indices will still be used. Roman indices instead refer to $\{1, 2, 3\}$ or $\{x, y, z\}$. Occasionally, they may cover spherical polar coordinates, *i.e.* $\{r, \theta, \phi\}$.

The Pauli matrices are

$$\sigma^1 = \begin{pmatrix} 0 & 1 \\ 1 & 0 \end{pmatrix}, \quad \sigma^2 = \begin{pmatrix} 0 & -i \\ i & 0 \end{pmatrix}, \quad \sigma^3 = \begin{pmatrix} 1 & 0 \\ 0 & -1 \end{pmatrix}. \tag{A.3}$$

The generators of $SU(2)$ rotations are normalized Pauli matrices, *i.e.* $\tau^a = \sigma^a/2$.

The Dirac matrices are

$$\gamma^i = \begin{pmatrix} 0 & \sigma^i \\ -\sigma^i & 0 \end{pmatrix}, \tag{A.4}$$

with

$$\gamma_{\text{W}}^0 = \begin{pmatrix} 0 & I_2 \\ I_2 & 0 \end{pmatrix}, \quad \gamma_{\text{D}}^0 = \begin{pmatrix} I_2 & 0 \\ 0 & -I_2 \end{pmatrix} \quad (\text{A.5})$$

in the Weyl (W) and Dirac (D) bases, respectively. They may be part of a vector

$$\gamma = (\gamma^0, \gamma^1, \gamma^2, \gamma^3)^{\text{T}}. \quad (\text{A.6})$$

Finally, an additional γ -matrix is introduced as

$$\gamma^5 = i\gamma^0\gamma^1\gamma^2\gamma^3. \quad (\text{A.7})$$

On an entirely different note: standard three-dimensional vectors may occasionally appear in boldface depending on the context, as in Chapter 9 and Appendix E.

$U(1)$ and $SU(2)$ gauge transformations

The action of $U(1)$ rotations on the pertinent fields in Chapter 2 can be expressed as [79, 94]

$$\Phi(x) \rightarrow e^{i\alpha(x)}\Phi(x) \quad (\text{A.8})$$

$$\psi(x) \rightarrow e^{i\alpha(x)}\psi(x) \quad (\text{A.9})$$

$$B_\mu(x) \rightarrow B_\mu(x) + \frac{i}{g_1}\partial_\mu\alpha(x) \quad (\text{A.10})$$

for a local rotation parameter $\alpha(x)$. The relevant $SU(2)$ transformations instead deliver

$$\Phi(x) \rightarrow U(x)\Phi(x) \quad (\text{A.11})$$

$$\psi(x) \rightarrow U(x)\psi(x) \quad (\text{A.12})$$

$$W_\mu(x) \rightarrow U(x)W_\mu U^\dagger(x) + \frac{i}{g_2}U(x)\partial_\mu U^\dagger(x), \quad (\text{A.13})$$

with $U(x)$ a $SU(2)$ matrix

$$U(x) = e^{i\beta^a(x)\tau^a} \quad (\text{A.14})$$

featuring three rotation parameters $\beta^a(x)$.

Tree-level masses of the relevant SM particles

The zero-temperature masses of the SM particles contemplated in the analyses are [209]

$$m_h = 125.10(14) \text{ GeV} \qquad m_\gamma = 0 \text{ GeV} \qquad (\text{A.15})$$

$$m_{W^\pm} = 80.379(12) \text{ GeV} \qquad m_Z = 91.1876(21) \text{ GeV} \qquad (\text{A.16})$$

$$m_t = 172.76(30) \text{ GeV} . \qquad (\text{A.17})$$

Further parameters and constants

The reduced Planck mass [122, 210]

$$M_{\text{Pl}} \stackrel{\text{def}}{=} \sqrt{\frac{\hbar c}{8\pi G}} = 2.43 \cdot 10^{18} \text{ GeV} \qquad (\text{A.18})$$

is used throughout this work. The number of relativistic degrees of freedom in the SM at $T \sim \mathcal{O}(10^2 \text{ GeV})$ is [91, 122]

$$g_*(T) \approx 106.75 . \qquad (\text{A.19})$$

Appendix B

Finite-temperature Feynman rules

These are the finite-temperature, momentum-space Feynman rules as presented in Ref. [91] and assumed in this work. Throughout these, β is the inverse temperature, $\beta \stackrel{\text{def}}{=} T^{-1}$.

Matsubara frequencies ω_n

$$\text{Bosons : } \omega_n^b = 2n\pi\beta^{-1} \quad (\text{B.1})$$

$$\text{Fermions : } \omega_n^f = (2n + 1)\pi\beta^{-1} \quad (\text{B.2})$$

Boson propagator

$$G_B(p) = \frac{i}{p_\mu p^\mu - m^2} \quad \text{with } p^\mu = (i\omega_n^b, \vec{p}) \quad (\text{B.3})$$

Fermion propagator

$$G_F(p) = \frac{i}{\gamma_\mu p^\mu - m} \quad \text{with } p^\mu = (i\omega_n^f, \vec{p}) \quad (\text{B.4})$$

Loop integrals

$$i\beta^{-1} \sum_{n=-\infty}^{\infty} \int \frac{d^3p}{(2\pi)^3} \quad (\text{B.5})$$

Vertices

$$- i\beta(2\pi)^3 \delta\left(\sum_i \omega_{n_i}\right) \delta^{(3)}\left(\sum_i \vec{p}_i\right) \quad (\text{B.6})$$

where the sums in the δ -functions account for energy and momentum conservation at each vertex.

Appendix C

Saddle-point method

The saddle point method as presented in Ref. [95] is reviewed. Let $\hat{\phi}$ denote a critical point of an action \mathcal{S}_E defined by the requirement

$$\left. \frac{\delta \mathcal{S}_E[\phi]}{\delta \phi} \right|_{\phi=\hat{\phi}} = 0. \quad (\text{C.1})$$

Then, up to quadratic order, the action around $\hat{\phi}$ can be approximated as [95]

$$\mathcal{S}_E[\phi] \approx \mathcal{S}_E[\hat{\phi}] + \int_X \frac{1}{2} \delta\phi \frac{\delta^2 \mathcal{S}_E[\hat{\phi}]}{\delta\phi^2} \delta\phi, \quad (\text{C.2})$$

with the definitions for the deviation $\delta\phi = \phi - \hat{\phi}$ from the critical field $\hat{\phi}$ and the fluctuation operator

$$\frac{\delta^2 \mathcal{S}_E[\hat{\phi}]}{\delta\phi^2}. \quad (\text{C.3})$$

Eq. (C.2) is ideally expressed in a basis of eigenfunctions k_n of the fluctuation operator. Typically, if its spectrum is discrete, the integral goes into a discrete sum over eigenvalues, thus simplifying the later functional integration. In such an eigenbasis, the deviations $\delta\phi$ can be expressed with coefficients b_n as

$$\delta\phi = \sum_n b_n k_n. \quad (\text{C.4})$$

The saddle-point method is fundamental in calculating decay and transition rates, which this work features plenty of. A decisive requirement to this aim is that the fluctuation operator be neither positive nor negative definite when evaluated at the saddle point $\hat{\phi}$, which calls for a mixed spectrum of positive and negative eigenvalues. Furthermore, in order to source a decay rate, the fluctuation operator will need to possess an uneven number of negative eigenvalues. In a standard treatment (cf. Refs. [95, 132, 133]), the fluctuation operator will have exactly one negative eigenvalue

$-\xi_-$ for a mode denoted as k_- in a spectrum of otherwise positive eigenvalues ξ_n for the corresponding modes k_n . Thus, one has that

$$\mathcal{S}_E[\phi] \approx \mathcal{S}_E[\hat{\phi}] + \int_X \frac{1}{2} \delta\phi \frac{\delta^2 \mathcal{S}_E[\hat{\phi}]}{\delta\phi^2} \delta\phi = \mathcal{S}_E[\hat{\phi}] - \frac{1}{2} \xi_-^2 b_-^2 + \sum_{n \geq 0} \frac{1}{2} \xi_n^2 b_n^2. \quad (\text{C.5})$$

One may apply this, for example, to the vacuum-to-vacuum amplitude [\(6.7\)](#) in Chapter [6](#). Redefining the functional measure as

$$\int \mathcal{D}\phi \stackrel{\text{def}}{=} \prod_m \int \frac{db_m}{\sqrt{2\pi}}, \quad (\text{C.6})$$

where m covers the indices of all possible modes, the partition function is factorized and calculated as

$$\begin{aligned} \mathcal{Z}[0] &= \int \mathcal{D}\phi e^{-\mathcal{S}_E[\phi]} \\ &\approx e^{-\mathcal{S}_E[\hat{\phi}]} \int \frac{db_-}{\sqrt{2\pi}} e^{\frac{1}{2} \xi_-^2 b_-^2} \prod_{n \geq 0} \int \frac{db_n}{\sqrt{2\pi}} e^{-\frac{1}{2} \xi_n^2 b_n^2} \\ &\approx i \sqrt{\frac{1}{\xi_-^2}} \left(\prod_{n \geq 0} \sqrt{\frac{1}{\xi_n^2}} \right) e^{-\mathcal{S}_E[\hat{\phi}]}. \end{aligned} \quad (\text{C.7})$$

Appendix D

Mathematical background

The structure of $SU(2)$ theory introduced in chapters 4 and 5 heavily relies on fundamental topological results. The present appendix aims to provide a minimal background. Interested readers are referred to Chapter 3 onward in Ref. [115], as well as the more recent Ref. [66], both of which this appendix closely follows and from which the definitions were seized.

D.1 Maps and homotopy theory

Let X, Y be two boundaryless manifolds and $x_0 \in X, y_0 \in Y$ a point on each. Mappings $f : X \mapsto Y$ will be called *based* if they are defined such that $f(x_0) = y_0$. As between manifolds, it is also possible to define mappings between two mappings f_0 and f_1 as

$$\tilde{f} : X \times [0, 1] \mapsto Y. \quad (\text{D.1})$$

The second parameter of the mapping \tilde{f} , henceforth τ , runs along the closed unit interval. Two mappings f_0 and f_1 will be *homotopically related* if

- \tilde{f} is continuous;
- τ can be chosen such that $\tilde{f}|_{\tau=0} = f_0$ and $\tilde{f}|_{\tau=1} = f_1$;
- $\tilde{f}(x_0; \tau) = y_0$ for all τ .

In other words, if two based mappings f_0 and f_1 can be continuously deformed into each other as a function of an external parameter, they are homotopic to each other. Homotopy meets the requirements for an equivalence relation. One can therefore define homotopy classes into which to sort the different f .

Homotopy classes for based mappings that have n -spheres S^n as their domain,

$f : S^n \mapsto Y$, are of particular interest. The reason for this is that important results can be derived for mappings defined on n -spheres. Via stereographic projection it is then possible to establish a correspondence between points on an n -sphere and points on \mathbb{R}^n , so that results calculated on the former are more generally applicable. The first important result to note is the structure formed by homotopy classes for based mappings $f : S^n \mapsto Y$. Very generally, they can be organized into sets $\pi_n(Y)$. These sets also fulfill the groups axioms for $n \geq 1$. An important result for these groups is that

$$\pi_n(S^n) = \mathbb{Z}. \tag{D.2}$$

The class of the constant mapping constitutes the identity element of $\pi_1(Y)$ and defines the notion of *contractibility*. Every element in this class is homotopic to the trivial loop, *i.e.* each and every one of these loops can be deformed in a continuous fashion such that the trajectories in Y are contracted into the single point y_0 . Contractibility has certain implications on the topology of a manifold. If every possible loop on Y can be contracted to a point, Y is said to be simply connected, *i.e.* it has no holes. Two prime and opposing examples for these properties are the 2-sphere (simply connected) and the 2-torus (not simply connected).

D.2 Saddle points of functions on manifolds

On a finite-dimensional, compact and connected manifold, multivariable calculus can go a long way to providing the location and nature of critical points. Take a well-behaved function f on a two-dimensional manifold M : depending on the number of negative eigenvalues of the Hessian, one can discriminate between a maximum, a saddle point and a minimum of f on M .

However, in field theory one typically deals with infinite-dimensional spaces where the tools of calculus can fall short. Nonetheless, when it comes to assessing the existence and location of saddle points, there exist other methods like the so-called *minmax* search procedure [66]. Its premise is intuitive: if two minima of f on M are known, one can set up trial paths between them along which f will necessarily have to attain a maximum. The lowest of these maxima corresponds to a saddle point of

the function on the manifold.

The minmax search procedure can be generalized to functions with only one minimum on M : one may search for the minmax of paths starting and ending at the minimum. An essential requisite for this is the existence of non-contractible loops – in other words, the existence of a hole – on the manifold such as to avoid the minimum being itself the minmax point. If met, it is possible to systematically proceed with the minmax search in each homotopy class.

Appendix E

The Standard Model sphaleron

E.1 Existence

The existence of the EW sphaleron was shown in Ref. [54] yet treated more didactically in Refs. [115, 118]. Their main ideas and basic outlines for the construction of the sphaleron were seized on for the following brief review and its distillation in Chapter 5.

Mathematically, the proof rests on two requirements. First of all, the gauge needs to be fixed; otherwise, potential saddle points would always sit on gauge orbits along which the energy would remain constant. Thus, the procedure would become ill-defined and no true saddle points would arise. In spherical coordinates, a radial gauge can be easily fixed by setting $W_r = 0$. It conveniently leaves one last, global degree of freedom untouched, which will be taken advantage of shortly.

The second requirement is that, at spatial infinity, the Higgs field drop towards its vacuum expectation value. On the one hand side, this defines a domain S^2 manifold at spatial infinity,

$$\Phi^\infty(\theta, \phi) = \lim_{r \rightarrow \infty} \Phi(r, \theta, \phi). \quad (\text{E.1})$$

Φ^∞ projects the tuples (θ, ϕ) onto the Higgs vacuum manifold. On the other hand side, it is necessary that any such mapping satisfy

$$|\Phi^\infty(\theta, \phi)| = \frac{v}{\sqrt{2}} \quad (\text{E.2})$$

for any choice of θ and ϕ . This makes sure that any vacuum field configuration has finite energy and remains physical. Condition (E.2) crucially compactifies the Higgs vacuum manifold to S_{vac}^3 . Expressions (E.1) and (E.2) thus induce a space of Higgs field Φ^∞ mappings that behave

$$\Phi^\infty: S^2 \mapsto S_{\text{vac}}^3. \quad (\text{E.3})$$

This will be a space of *based mappings* (see Appendix [D](#)): by exhausting the residual gauge freedom still available and imposing a polar gauge condition, one can construct the base point

$$\Phi^\infty(\theta = 0) = \frac{v}{\sqrt{2}} \begin{pmatrix} 0 \\ 1 \end{pmatrix}. \quad (\text{E.4})$$

Thus, configuration space \mathcal{C} and the space of based mappings $\text{Maps}(S^2 \mapsto S^3)$ are topologically one and the same.

The above result has profound implications – most notably, the existence of non-contractible loops. This is a consequence of the central topological identity

$$\pi_1(\text{Maps}(S^2 \mapsto S^3)) = \pi_3(S^3) = \mathbb{Z}, \quad (\text{E.5})$$

which states the existence of loop classes other than the trivial, contractible class. The strategy in finding a sphaleron consists in building a loop of fields topologically equivalent to a single mapping of non-zero topological degree. Since the topological degree is a homotopy invariant, if the mapping constructed has a non-zero degree, its homotopy class is different from the trivial, contractible class of degree zero. The original loop of mappings thus is non-contractible. On such a non-contractible loop, it is possible to perform a minmax search of the energy (Appendix [D](#)). In the last step, the loop will be reinterpreted as a path between adjacent vacuum configurations separated by a potential barrier. The sphaleron will correspond to the configuration atop the barrier, on the lowest-energy mountain pass.

The non-contractible loop of fields can be constructed by invoking an external loop parameter $\mu \in [0, \pi]$. Thus, one can define a mapping $\Phi^\infty(\mu) : S^2 \mapsto S^3_{\text{vac}}$ as

$$\Phi^\infty(\theta, \phi; \mu) = \begin{pmatrix} \Phi_1^\infty \\ \Phi_2^\infty \end{pmatrix} = \frac{v}{\sqrt{2}} \begin{pmatrix} \sin \mu \sin \theta e^{i\phi} \\ e^{-i\mu} (\cos \mu + i \sin \mu \cos \theta) \end{pmatrix}, \quad (\text{E.6})$$

or equivalently, in terms of the real components,

$$\Phi_{\text{Re}}^\infty(\theta, \phi; \mu) = \frac{v}{\sqrt{2}} \begin{pmatrix} \sin \mu \sin \theta \cos \phi \\ \sin \mu \sin \theta \sin \phi \\ \sin^2 \mu \cos \theta + \cos^2 \mu \\ \sin \mu \cos \mu (\cos \theta - 1) \end{pmatrix}. \quad (\text{E.7})$$

This loop of fields can be reinterpreted as a single identity mapping $\Psi : S^3_{\text{dom}} \mapsto S^3_{\text{vac}}$ if a one-to-one correspondence between points $p(\theta, \phi, \mu)$ on S^3_{dom} and every triple (θ, ϕ, μ) is established. The reader can easily check that with $\phi \in [0, 2\pi]$ and $\theta \in$

$[0, \pi]$,

$$p(\theta, \phi, \mu) = \frac{v}{\sqrt{2}} \begin{pmatrix} \sin \mu \sin \theta \cos \phi \\ \sin \mu \sin \theta \sin \phi \\ \sin^2 \mu \cos \theta + \cos^2 \mu \\ \sin \mu \cos \mu (\cos \theta - 1) \end{pmatrix} \quad (\text{E.8})$$

provides a sensible bijection. Making use of the one-to-one correspondence, it is now easy to see that

$$\Psi(p) = \Phi_{\text{Re}}^\infty(\theta(p), \phi(p), \mu(p)) \quad (\text{E.9})$$

with Eq. (E.7) yields an identity mapping $S_{\text{dom}}^3 \mapsto S_{\text{vac}}^3$. The identity mapping has a topological degree of one, as a loop over the domain covers the target manifold exactly once; it is therefore non-contractible. It follows that the loop of fields $\Phi^\infty(\theta, \phi; \mu)$ is non-contractible as well. Therefore, unless the energy were to be constant for all field configurations, a saddle point – and thus, a sphaleron field configuration – must exist.

E.2 $U(1)$ corrections to the SM sphaleron energy

As the physical mixing angle θ_W is parametrically small, its effects can be added perturbatively to the to the pure $SU(2)$ sphaleron derived the previous section. To this aim, a simplified approach was suggested in Ref. [55] which will be followed here closely. The full Lagrangian (5.1) prompts an energy shift

$$\Delta\mathcal{E} = \int d^3x \left(\frac{1}{4} B_{ij} B^{ij} - B^i J_i \right), \quad (\text{E.10})$$

corresponding to the gauge kinetic term for the field B_i . The Euler-Lagrange equations for this shift define a current

$$J_i(x) = \partial_j B_{ij} = -\frac{1}{2} i g_1 \left[\Phi^\dagger(x) \mathcal{D}_i \Phi(x) - (\mathcal{D}_i \Phi(x))^\dagger \Phi(x) \right]. \quad (\text{E.11})$$

In the presence of Φ and W_i , the current J_i will in general not vanish and instead source a non-zero field B_i . The latter will couple to and in general shift the pure $SU(2)$ solutions to Φ and W_i . Neglecting such feedback effects of order θ_W^2 , the energy shift can be shown to be

$$\Delta\mathcal{E} = - \int d^3x \frac{1}{2} B_i J^i. \quad (\text{E.12})$$

The current J_i is axially symmetric and thus lends itself to a parametrization

$$\mathbf{J} = \frac{1}{2}g_1v^2\frac{h^2(g_2vr)(1-f(g_2vr))}{r^2}(-y, x, 0)^T. \quad (\text{E.13})$$

Via

$$-\nabla^2\mathbf{B} = \mathbf{J} \quad (\text{E.14})$$

it will give rise to the $U(1)$ field, which itself admits an axially symmetric ansatz

$$\mathbf{B} = \frac{1}{2}g_1v^2q(\xi)(-y, x, 0)^T \quad (\text{E.15})$$

with $q(\xi)$ a function of the dimensionless radial coordinate $\xi = g_2vr$. As all other fields, \mathbf{B} needs to attain its – in this case vanishing – vacuum value at spatial infinity while the theory remains well-defined at the origin. This establishes the boundary conditions

$$\lim_{\xi \rightarrow 0} \xi^3 q(\xi) = 0, \quad \lim_{\xi \rightarrow \infty} q(\xi) = 0 \quad (\text{E.16})$$

on $p(\xi)$. Its trajectory is determined by

$$\xi^2 \frac{d^2q}{d\xi^2} + 4\xi \frac{dq}{d\xi} = -h^2(1-f), \quad (\text{E.17})$$

which is formally solved by

$$q(\xi) = \frac{1}{3\xi^3} \int_0^\xi d\eta \eta^2 h^2(\eta) [1-f(\eta)] + \int_\xi^\infty d\eta \frac{1}{3\eta} h^2(\eta) [1-f(\eta)] \quad (\text{E.18})$$

The energy shift can thus be expressed in terms of the radial functions f , h and p as

$$\Delta\mathcal{E} = -\frac{\pi}{3} \frac{g_1^2 v}{g_2^3} \int_0^\infty d\xi \xi^2 h^2(\xi) [1-f(\xi)] q(\xi). \quad (\text{E.19})$$

This derivation was carried out for the SM case. However, it is also valid for the two extended models investigated in this work. In the singlet extension, the singlet field not couple to the $U(1)$ gauge field and hence does not alter the derivation above. In the IDM scenarios of this work, one of the Higgs fields always vanishes ($v_2(T) = 0$); thus, (E.19) remains valid under the proper replacements of h by the non-vanishing Higgs field.

Appendix F

Sphaleron rate

Ref. [56] employed a semi-classical treatment of the sphaleron process which has become a commonplace approach in the literature (see *e.g.* Refs. [27, 75, 122]). The rate of sphaleron processes may be treated as of that of a particle on top of a potential barrier overcoming the latter in the correct direction. The rate of such processes can be calculated as [27, 56]

$$\begin{aligned}\Gamma &= \langle \delta(x) \theta(p) \rangle \\ &= \frac{\int dx dp \delta(x) p \theta(p) \exp\left[-\beta\left(\frac{1}{2}p^2 + V(x)\right)\right]}{\int dx dp \exp\left[-\beta\left(\frac{1}{2}p^2 + V(x)\right)\right]} \\ &\approx \frac{\omega_0}{2\pi} e^{-\beta V_0},\end{aligned}\tag{F.1}$$

where $\delta(x)$ prepares the particle at the origin and $\theta(p)$ defines the correct momentum direction. The picture hereby defined does not differ too much from standard vacuum decay as treated in Chapter 6, and thus it will be useful to work out the imaginary component of the free energy, which is expected to exist for a saddle point. Denoting the modes of the vacuum and the unstable direction on the barrier as ω_0 and $-\omega_-$, respectively, and with V_0 as the height of the potential barrier, for a sphaleron one has that

$$\begin{aligned}\text{Im } F &= T \text{Im} (\ln \mathcal{Z}) = T \frac{\text{Im} (\mathcal{Z})}{\mathcal{Z}} \\ &\approx T \frac{\text{Im} \int dx dp \exp\left[-\beta\left(\frac{1}{2}p^2 + V_0 - \frac{1}{2}\omega_-^2 x^2\right)\right]}{\int dx dp \exp\left[-\beta\left(\frac{1}{2}p^2 + \frac{1}{2}\omega_0^2 x^2\right)\right]} \\ &= \frac{\omega_0}{2\omega_- \beta} e^{-\beta V_0}.\end{aligned}\tag{F.2}$$

These results can be combined such as to deliver a sphaleron rate

$$\Gamma_{\text{sph}} \approx \frac{\omega_-}{\pi} \frac{\text{Im } \mathcal{Z}_{\text{sph}}}{\mathcal{Z}_0}\tag{F.3}$$

in terms of partition functions for fluctuations about the sphaleron and vacuum configurations, \mathcal{Z}_{sph} and \mathcal{Z}_0 . The calculation of \mathcal{Z}_{sph} requires some care with regards to symmetries and the associated flat directions in field space. With a proper treatment of the associated zero modes, the sphaleron rate can be shown to be [56]

$$\frac{\Gamma_{\text{sph}}}{V} \approx \frac{\omega_-}{2\pi} \mathcal{N}_{\text{tr}}(\mathcal{N}_{\text{rot}} \mathcal{V}_{\text{rot}}) \left(\frac{\alpha_W T}{4\pi} \right)^3 \alpha_{W,T}^{-6} \kappa e^{-\mathcal{E}(T)/T}. \quad (\text{F.4})$$

\mathcal{N}_{tr} and \mathcal{N}_{rot} are normalization factors related to the translational and rotational symmetries of the system. $\mathcal{V}_{\text{rot}} = 8\pi^2$ is a volume factor of the rotation group, and $\alpha_{W,T}$ for the weak gauge coupling parameter g_2 at high temperatures. κ is the fluctuation determinant. In the SM, assuming $\lambda/g_2^2 \approx 0.3$, one can evaluate these quantities to [122, 211]

$$\mathcal{N}_{\text{tr}} \approx 7.6, \quad \mathcal{N}_{\text{rot}} \approx 11.2 \quad (\text{F.5})$$

$$\omega_- \approx 0.65 g_2^2 v(T)^2 \quad (\text{F.6})$$

$$\alpha_{W,T} = \alpha_W T / g_2 v(T) \quad (\text{F.7})$$

$$10^{-4} < \kappa < 10^{-1}. \quad (\text{F.8})$$

Appendix G

Relaxation method

In order to apply Newton's method, and as pointed out in Chapter 9 and Ref. [169], the system is perturbed linearly, *i.e.*

$$\tilde{\mathbf{y}}_k \rightarrow \tilde{\mathbf{y}}_k + \Delta \tilde{\mathbf{y}}_k. \quad (\text{G.1})$$

For the sake of clarity throughout this appendix, the tilde will be systematically omitted. At k , the vector \mathbf{D}_k now reads

$$\mathbf{D}_k(\mathbf{y}_k + \Delta \mathbf{y}_k, \mathbf{y}_{k-1} + \Delta \mathbf{y}_{k-1}) \stackrel{\text{def}}{=} \widehat{\mathbf{D}}_k(\mathbf{y}_k, \mathbf{y}_{k-1}) \stackrel{!}{=} \mathbf{0}_N. \quad (\text{G.2})$$

To linear order in the perturbations $\Delta \mathbf{y}_k$, one has

$$\widehat{\mathbf{D}}_k(\mathbf{y}_k, \mathbf{y}_{k-1}) \approx \mathbf{D}_k(\mathbf{y}_k, \mathbf{y}_{k-1}) + \sum_{n=1}^N \frac{\partial \mathbf{D}_k}{\partial y_{n,k-1}} \Delta y_{n,k-1} + \sum_{n=1}^N \frac{\partial \mathbf{D}_k}{\partial y_{n,k}} \Delta y_{n,k} \stackrel{!}{=} \mathbf{0}_N. \quad (\text{G.3})$$

For simplicity, one may define the Jacobian \mathbf{S} such that

$$S_{j,n} = \frac{\partial D_{j,k}}{\partial y_{n,k-1}}, \quad S_{j,n+N} = \frac{\partial D_{j,k}}{\partial y_{n,k}}, \quad n = 1, \dots, N. \quad (\text{G.4})$$

The matrix \mathbf{S} is $(MN \times MN)$ -dimensional and its structure encodes the coupling between adjacent state vectors. Making use of the second equality in Eq. (G.3), one can write

$$\sum_{n=1}^N S_{j,n} \Delta y_{n,k-1} + \sum_{n=N+1}^{2N} S_{j,n} \Delta y_{n-N,k} = -D_{j,k}, \quad j = 1, \dots, N. \quad (\text{G.5})$$

Every deviation vector \mathbf{D}_k is to be cancelled by appropriate perturbations at k and its adjacent mesh indices. At the boundaries,

$$\sum_{n=1}^N S_{j,n} \Delta y_{n,1} = -D_{j,1}, \quad j = n_2 + 1, n_2 + 2, \dots, N \quad (\text{G.6})$$

Appendix H

Aspects of the IDM

H.1 Parameter constraints in the IDM

H.1.1 Perturbative unitarity

Following Refs. [181, 212], the S matrix for all processes containing scalars has the following eigenvalues:

$$w_{1,2} = \lambda_3 \pm \lambda_4 \quad (\text{H.1})$$

$$w_{3,4} = \lambda_3 \pm \lambda_5 \quad (\text{H.2})$$

$$w_{5,6} = \lambda_3 + 2\lambda_4 \pm 3\lambda_5 \quad (\text{H.3})$$

$$w_{7,8} = -\lambda_1 - \lambda_2 \pm \sqrt{(\lambda_1 - \lambda_2)^2 + \lambda_4^2} \quad (\text{H.4})$$

$$w_{9,10} = -\lambda_1 - \lambda_2 \pm \sqrt{(\lambda_1 - \lambda_2)^2 + \lambda_5^2} \quad (\text{H.5})$$

$$w_{11,12} = -3\lambda_1 - 3\lambda_2 \pm \sqrt{9(\lambda_1 - \lambda_2)^2 + (2\lambda_3 + \lambda_4)^2}. \quad (\text{H.6})$$

Perturbative unitarity is met when they all meet

$$|w_i| \leq 8\pi. \quad (\text{H.7})$$

H.1.2 Oblique parameters

Following Refs. [149, 181, 213], deviations of the EW precision observables can be parametrized as

$$S = \frac{1}{72\pi(x_2^2 - x_1^2)^2} [x_2^6 f_a(x_2) - x_1^6 f_a(x_1) + 9x_1^2 x_2^2 (x_2^2 f_b(x_2) - x_1^2 f_b(x_1))] \quad (\text{H.8})$$

$$T = \frac{1}{32\pi^2 \alpha v^2} [f_c(m_{H^\pm}^2, m_{H^2}^2) + f_c(m_{H^\pm}^2, m_{A^2}^2) - f_c(m_A^2, m_H^2)] \quad (\text{H.9})$$

assuming $\alpha \approx 1/127$ for the electromagnetic fine-structure constant at an energy scale $\sqrt{s} \sim m_Z$. The relevant functions featured above are

$$f_a(x) \stackrel{\text{def}}{=} -5 + 12 \ln(x), \quad (\text{H.10})$$

$$f_b(x) \stackrel{\text{def}}{=} 3 - 4 \ln(x) \quad (\text{H.11})$$

and

$$f_c(x, y) \stackrel{\text{def}}{=} \begin{cases} \frac{x+y}{2} - \frac{xy}{x-y} \ln \frac{x}{y}, & x \neq y \\ 0, & x = y \end{cases}. \quad (\text{H.12})$$

H.1.3 Plotting range in plots of σ and $\mathcal{E}(T)/T$

One unphysical aspect of the plots in Fig. [10.5](#) and those following which should be acknowledged is the choice of the plotting range, which does not tally with that of Figs. [10.3](#) and [10.4](#). It was found that for low enough Δm , the low VEV at the phase transition spoils the convergence behaviour of the relaxation code on account of purely numerical effects. In such fringe cases, the finiteness of the solution domain addressed in Chapter [9](#) becomes apparent¹, and the calculations of the energy \mathcal{E} and σ become unreliable. For this reason, all plots of σ (and later \mathcal{E}) are cut off at $\xi \gtrsim 0.4 - 0.6$ or at the corresponding Δm .

¹And so do the computational limitations, as an increase in the solution domain while keeping a reliable mesh density causes the computational cost to rocket.

Appendix I

Aspects of the rSM

I.1 Eigenvalues of the Higgs-singlet mass matrix

The matrix (11.7) can be recast as a diagonal matrix with the two mass square eigenvalues (156)

$$\begin{aligned} m_{h_1, h_2}^2(h, s) = & \frac{1}{2} \left[\left(3\lambda + \frac{a_2}{2} \right) h^2 + \left(3b_4 + \frac{a_2}{2} \right) s^2 + \left(\frac{a_1}{2} + 2b_3 \right) s - \mu^2 + b_2 \right. \\ & \mp \left\{ \left[\left(3\lambda - \frac{a_2}{2} \right) h^2 - \left(3b_4 - \frac{a_2}{2} \right) s^2 + \left(\frac{a_1}{2} - 2b_3 \right) s - \mu^2 - b_2 \right]^2 \right. \\ & \left. \left. + 4 \left(a_2 s + \frac{a_1}{2} \right)^2 h^2 \right\}^{\frac{1}{2}} \right]. \end{aligned} \quad (\text{I.1})$$

I.2 Perturbative unitarity constraints

The scattering cross sections in the model need to remain bounded up to high energies. In a partial wave analysis, this can be enforced by requiring the scattering amplitudes $a_l(s)$ to satisfy (202)

$$|\text{Re}\{a_l(s)\}| \leq \frac{1}{2} \quad (\text{I.2})$$

as the center-of-mass energy $\sqrt{s} \rightarrow \infty$. Ref. (197) proposes to consider the S matrix for all $2 \rightarrow 2$ processes involving scalars and longitudinal gauge bosons. The reference classifies them into the following charge channels:

- seven neutral channels: $\{h_1 h_1, h_2 h_2, h_1 h_2, h_1 Z, h_2 Z, ZZ, W^+ W^-\}$;
- three charge-1 channels: $\{h_1 W^+, h_2 W^+, ZW^+\}$;
- one charge-2 channel: $\{W^+ W^-\}$.

The partial wave analysis can be translated into a condition on the eigenvalues w_l of the S matrix, $|w_l| \leq 8\pi$. The S matrix presented here corresponds to the one outlined in the appendix of Ref. [197]. For a calculation of its matrix elements, one may consult Ref. [202].

Neutral channels

The first sub-matrix \mathcal{S}_0 accounts for interactions in the neutral channels. Its non-zero elements are listed below.

$$\mathcal{S}_{11} = -3(a_2 \cos^2\theta \sin^2\theta + b_4 \sin^4\theta + \lambda \cos^4\theta) \quad (\text{I.3})$$

$$\mathcal{S}_{12} = \frac{1}{8}(3 \cos 4\theta (-a_2 + b_4 + \lambda) - a_2 - 3b_4 - 3\lambda) \quad (\text{I.4})$$

$$\mathcal{S}_{13} = \frac{3 \sin 2\theta (\cos 2\theta (-a_2 + b_4 + \lambda) - b_4 + \lambda)}{2\sqrt{2}} \quad (\text{I.5})$$

$$\mathcal{S}_{16} = -\frac{1}{2}a_2 \sin^2\theta - \lambda \cos^2\theta \quad (\text{I.6})$$

$$\mathcal{S}_{17} = -\frac{a_2 \sin^2\theta + 2\lambda \cos^2\theta}{\sqrt{2}} \quad (\text{I.7})$$

$$\mathcal{S}_{22} = -3(a_2 \cos^2\theta \sin^2\theta + b_4 \cos^4\theta + \lambda \sin^4\theta) \quad (\text{I.8})$$

$$\mathcal{S}_{23} = -\frac{3 \sin 2\theta (\cos 2\theta (-a_2 + b_4 + \lambda) + b_4 - \lambda)}{2\sqrt{2}} \quad (\text{I.9})$$

$$\mathcal{S}_{26} = \frac{1}{2}a_2 \cos^2\theta - \lambda \sin^2\theta \quad (\text{I.10})$$

$$\mathcal{S}_{27} = -\frac{a_2 \cos^2\theta + 2\lambda \sin^2\theta}{\sqrt{2}} \quad (\text{I.11})$$

$$\mathcal{S}_{33} = \frac{1}{4}(3 \cos 4\theta (-a_2 + b_4 + \lambda) - a_2 - 3b_4 - 3\lambda) \quad (\text{I.12})$$

$$\mathcal{S}_{36} = \frac{(2\lambda - a_2) \cos \theta \sin \theta}{\sqrt{2}} \quad (\text{I.13})$$

$$\mathcal{S}_{37} = (2\lambda - a_2) \cos \theta \sin \theta \quad (\text{I.14})$$

$$\mathcal{S}_{44} = -a_2 \sin^2\theta - 2\lambda \cos^2\theta \quad (\text{I.15})$$

$$\mathcal{S}_{45} = (2\lambda - a_2) \cos \theta \sin \theta \quad (\text{I.16})$$

$$\mathcal{S}_{55} = -a_2 \cos^2\theta - 2\lambda \sin^2\theta \quad (\text{I.17})$$

$$\mathcal{S}_{66} = -3\lambda \quad (\text{I.18})$$

$$\mathcal{S}_{67} = -\sqrt{2}\lambda \quad (\text{I.19})$$

$$\mathcal{S}_{77} = -4\lambda \quad (\text{I.20})$$

Charge-1 channels

The next block, \mathcal{S}_I , accounts for scatterings in the charge-1 channels.

$$\mathcal{S}_I = \begin{pmatrix} -2\lambda \cos^2\theta - a_2 \sin\theta & (2\lambda - a_2) \cos\theta \sin\theta & 0 \\ (2\lambda - a_2) \cos\theta \sin\theta & -a_2 \cos^2\theta - 2\lambda \sin^2\theta & 0 \\ 0 & 0 & -2\lambda \end{pmatrix} \quad (\text{I.21})$$

Charge-2 channels

Finally, charge-2 channels have but one entry.

$$\mathcal{S}_{II} = -2\lambda \quad (\text{I.22})$$

The full S matrix is a direct sum of the partial matrices, $\mathcal{S} = \mathcal{S}_0 \oplus \mathcal{S}_I \oplus \mathcal{S}_{II}$. Perturbative unitarity of the scatterings considered requires its eigenvalues w_l to fulfill

$$|w_l| \leq 8\pi. \quad (\text{I.23})$$

Declaration of honesty

I, Álvaro Lozano Onrubia, hereby declare the sole authorship of this thesis. All sources and aids employed throughout have been clearly indicated.

Ich, Álvaro Lozano Onrubia, erkläre mich hiermit zum alleinigen Verfasser dieser Arbeit. Alle zu ihrer Erstellung benutzten Quellen und Hilfen wurden deutlich angegeben.

Heidelberg, June 17, 2021

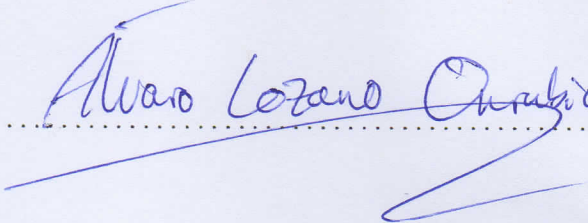
.....

Declaration of honesty

I, Álvaro Lozano Onrubia, hereby declare the sole authorship of this thesis. All sources and aids employed throughout have been clearly indicated.

Ich, Álvaro Lozano Onrubia, erkläre mich hiermit zum alleinigen Verfasser dieser Arbeit. Alle zu ihrer Erstellung benutzten Quellen und Hilfen wurden deutlich angegeben.

Heidelberg, June 17, 2021


Álvaro Lozano Onrubia